UNIVERSITY OF CALIFORNIA SAN DIEGO

Multiform Medical Device Platforms for Cellular Discovery and Diagnostics

A Dissertation submitted in partial satisfaction of the requirements
for the degree Doctor of Philosophy

in

Bioengineering

by

Lauren Beth Waller

Committee in charge:

Professor Andrew McCulloch, Chair
Professor Yu-Hwa Lo, Co-Chair
Professor Drew Hall
Professor Ratneshwar Lal
Professor Marc Andre Meyers

2023

The Dissertation of Lauren Beth Waller is approved, and it is acceptable in quality and form for publication on microfilm and electronically.

University of California San Diego

2023

DEDICATION

For Marilyn – who always believed in me.

In recognition of their unending support and encouragement, this dissertation is also dedicated to my parents Susan M Waller and James S Waller, my fiancé Garret D Wiesehan, my brother Andrew J Waller, and all the family and friends who have encouraged me along the way.

TABLE OF CONTENTS

LIST OF FIGURES

LIST OF TABLES

LIST OF ABBREVIATIONS

AML	Acute Myeloid Leukemia
AOD	Acoustic Optical Deflector
BSA	Bovine Serum Albumin
COC	Cyclo-Olefin Copolymer
CPLCL	Cold Plasma-based Live Cell Lithography
CW	Continuous Wave
DBD	Dielectric Barrier Discharge
FACS	Fluorescence Activated Cell Sorting
FBS	Fetal Bovine Serum
GUI	Graphical User Interface
IFC	Imaging Flow Cytometer
IR	Infrared
LAMP	Loop-Mediated Isothermal Amplification
LED	Light Emitting Diode
LFIA	Lateral Flow Immunoassay
MACS	Magnetic- Activated Cell Sorting
NA	Numerical Aperture
PMT	Photomultiplier tube
PSA	Pressure sensitive adhesive
PZT	Piezoelectric
ROI	Region of Interest
RONS	Reactive Oxygen/ Nitrogen Species

RT-LAMP	Reverse-Transcription Loop-Mediated Isothermal Amplification
SAW	Surface Acoustic Wave
UV	Ultraviolet
WBC	White blood cell

ACKNOWLEDGEMENTS

I would like to acknowledge my doctoral committee for their guidance and support. Special thanks to my advisor Professor Yu-Hwa Lo and co-advisor Professor Andrew D McCulloch. I would also like to acknowledge the Medical Devices Group, which has provided research support, scientific guidance, constructive feedback and many positive moments throughout the last several years. Special thanks to Xinyu Chen, Edward Wang, Zhilin Guo, Rui Tang, Zunming Zhang, and Brendan Schuster.

Chapter 1, in full, is a near-verbatim reprint of the material as it appears in APL Photonics 2021. Chen X*, Waller L*, Chen J, Tang R, Zhang Z, Gagne I, Gutierrez B, Cho SH, Tseng C-Y, Lian I, Lo Y-H., AIP Publishing, 2021. The dissertation author was the co-primary investigator and author of this paper.

Chapter 2, in full, is a near-verbatim reprint of the material as it appears in Frontiers in Bioengineering and Biotechnology, 2022. Waller L*, Guo Z*, Tang R, Zhang Z, Wang E, Yasuhara-Bell J, Laurent L and Lo Y-H, Frontiers, 2022. The dissertation author was the co-primary investigator and author of this paper.

Chapter 3 contains unpublished material coauthored with Guo, Zhilin and Schuster, Brendan. The dissertation author was the primary author of this chapter.

VITA

2017 Bachelor of Science in Bioengineering, University of California San Diego

2019 MiniMBA Certificate Program, Rady School of Management, University of California San Diego

2021 Professional Leadership and Integrity Certificate Program, Rady School of Management, University of California San Diego

2023 Doctor of Philosophy in Bioengineering, University of California San Diego

PUBLICATIONS

Waller L[*], Guo Z[*], Tang R, Zhang Z, Wang E, Yasuhara-Bell J, Laurent L and Lo Y-H (2022) High Sensitivity, Rapid Detection of Virus in High Traffic Environments. Front. Bioeng. Biotechnol. 10:877603. doi: 10.3389/fbioe.2022.877603 ([*]co- first author)

Chen X[*], Waller L[*], Chen J, Tang R, Zhang Z, Gagne I, Gutierrez B, Cho SH, Tseng C-Y, Lian I, Lo Y-H. (2021). Label-free image-encoded microfluidic cell sorter with a scanning Bessel beam. APL Photonics 6, 076101. https://doi.org/10.1063/5.0051354. ([*]co- first author)

Zhang Z, Tang R, Chen X, Waller L, Kau A, Fung A, Gutierrez B, An C, Cho SH, Shi L, and Lo Y-H. (2022). A high-throughput technique to map cell images to cell positions using a 3D imaging flow cytometer. PNAS. https://doi.org/10.1073/pnas.2118068119.

Tang R, Zhang Z, Chen X, Waller L, Zhang AC, Chen J, Han Y, An C, Cho SH, Lo Y-H. 3D side-scattering imaging flow cytometer and convolutional neural network for label-free cell analysis. APL Photonics 5, 126105 (2020); https://doi.org/10.1063/5.0024151.

Chen X, Gu Y, Chen J, Lee C-H, Gagne I, Tang R, Waller L, Zhang Z, Zhang AC, Han Y, Wang W, Lian I, Cho SH, Lo Y-H. Image-guided cell sorting using fast scanning lasers. APL Photonics 5, 040801 (2020); https://doi.org/10.1063/1.5144117

Tang R, Chen X, Zhang Z, Waller L, Chen J, Gu Y, Han Y, Lee C-H, Gagne I, Zhang AC, Cho SH, Lo Y-H. (2020). 2D image-guided cell sorter and 3D imaging flow cytometer. SPIE BiOS. Vol 11250, High-Speed Biomedical Imaging and Spectroscopy V; 112500H (2020) https://doi.org/10.1117/12.2547689.

Tang R, Xia L, Gutierrez B, Gagne I, Munoz A, Eribez K, Jagnandan N, Chen X, Zhang Z, Waller L, Alaynick W, Cho SH, An C, Lo Y-H. Low-Latency Label-Free Image-Activated Cell Sorting Using Fast Deep Learning and Ai Inferencing. http://dx.doi.org/10.2139/ssrn.4177986

Patents:

Sur R, Haleblian G, Schmid-Schoenbein, Waller L, Canacari N, Zamat A. Renal stone entrapment cage and flushing catheter. (2017). WO2018094050A2. https://patents.google.com/patent/WO2018094050A2/en?oq=WO2018094050A2WO2018

Thermal Endoscope for Clinical Diagnostics. US Provisional Application 62/833,509 · Filed Apr 12, 2019. 094050A2

Label-Free Image-Encoded Microfluidic Cell Sorter with a Scanning High Focal Depth Beam, Filed 2022.

FIELD OF STUDY

Major Field: Bioengineering

ABSTRACT OF THE DISSERTATION

Multiform Medical Device Platforms for Cellular Discovery and Diagnostics

by

Lauren Beth Waller

Doctor of Philosophy in Bioengineering

University of California San Diego, 2023

Professor Yu-Hwa Lo, Chair
Professor Andrew McCulloch, Co-Chair

Medical devices enable crucial insight into fundamental biological processes, development and disease. In this dissertation we present three medical devices for cellular discovery and diagnostics. In chapter I, we demonstrate a label- free image-encoded microfluidic cell sorter with a scanning Bessel beam. Microfluidics- based cell sorters offer a convenient, high information content, disposable solution that overcomes many of the disadvantages of conventional cell sorters. However, flow confinement in the microfluidic channel is generally

one-dimensional via sheath flow. Consequently, the equilibrium cell distribution spreads outside the focal plane of commonly used Gaussian laser excitation beams, giving rise to a high number of blurred images that hinder subsequent cell sorting based on cell image features. To address this issue, we present a Bessel–Gaussian beam image-guided cell sorter with an ultra-long depth of focus, enabling focused images of >85% of passing cells. This system features label-free sorting capabilities based on features extracted from the output temporal waveform of a photomultiplier tube (PMT) detector.

In chapter II, we demonstrate an automated, high throughput diagnostic device suited for high-traffic settings. Here we demonstrate a multiplex reverse-transcription loop-mediated isothermal amplification (RT-LAMP) coupled with a gold nanoparticle-based lateral flow immunoassay (LFIA) capable of detecting up to three unique viral gene targets in 15 min. RT-LAMP primers associated with three separate gene targets from the SARS-CoV-2 virus (Orf1ab, Envelope, and Nucleocapsid) were added to a one-pot mix. A colorimetric change from red to yellow occurs in the presence of a positive sample. Positive samples are run through a LFIA to achieve specificity on a multiplex three-test line paper assay. Positive results are indicated by a characteristic crimson line. The device is almost fully automated and is deployable in any community setting with a power source.

In chapter III, we demonstrate a novel prototype and concept for cold plasma – based live cell lithography. A plasma jet is formed using a custom dual – lead nozzle, high voltage alternating current transformer, nitrogen feed gas, and frame. The concept aims to leverage the batch processing and spatial resolution advantages of lithography to identify, preserve, and isolate cells of interest while preserving their spatial information.

CHAPTER 1: LABEL-FREE IMAGE-ENCODED MICROFLUIDIC CELL SORTER WITH A SCANNING BESSEL BEAM

1.1 ABSTRACT

Microfluidics-based, label-free image-guided cell sorters offer a low-cost, high information content, and disposable solution that overcomes many limitations in conventional cell sorters. However, flow confinement for most microfluidic devices is generally only one-dimensional using sheath flow. Consequently, the equilibrium distribution of cells spreads beyond the focal plane of commonly used Gaussian laser excitation beams, resulting in a large number of blurred images that hinder subsequent cell sorting based on cell image features. To address this issue, we present a Bessel Gaussian beam image-guided cell sorter with an ultra-long depth of focus, enabling focused images of >85% of passing cells. This system features label-free sorting capabilities based on features extracted from the output temporal waveform of a photomultiplier tube (PMT) detector. For the sorting of polystyrene beads, SKNO1 leukemia cells, and *Scenedesmus* green algae, results indicate a sorting purity of 97%, 97%, and 98%, respectively, demonstrating that temporal waveforms from PMT output have strong correlation to cell image features. These correlations are confirmed by off-line reconstructed cell images from a temporal-spatial transformation algorithm tailored to the scanning Bessel Gaussian beam.

1.2 INTRODUCTION

Characterization, classification, and isolation of cell types among a heterogenous population based on their stain-free morphological characteristics can yield significant biological insight, especially when coupled with phenotype-genotype correlations. Cell classification processes often require both the multiparametric spatial information of intracellular structures and

high data volume analysis. In recent years, genome sequencing and population genomic analysis have had a profound impact in biological research by enabling high-volume comparative analysis, enabling new cell type discovery and uncovering previously unknown cellular heterogeneities [1]. This has significantly increased the need for methods capable of isolating cells of interest in a label-free environment to simplify the process flow, reduce cost, minimize cell disruptions by labeling, and overcome limitations of biomarker availability and specificity. Conventional methods of cell sorting include optical microscopy [2], deterministic lateral displacement [3], density gradient methods [4], and fluorescence and magnetic-activated cell sorting (FACS/MACS) [5-8]. However, these techniques suffer from some of the following aspects, including lack of specificity, low throughput, high cell loss, population-based sorting without single cell resolution, and the need for biochemical labeling.

A significant development in the field of label-free cell sorting is in the invention of an imaging flow cytometer/cell sorter. This microfluidic-based technology enables the highly informative morphological and spatial characterization of intracellular structures and subsequent sorting of cells of interest at a throughput of over two hundred cells per second [9]. Various possible configurations exist, each with unique characteristics and applications ranging from inexpensive, custom laboratory tools to precise clinical instruments. Examples of compatible on-chip cell sorting techniques include surface acoustic waves (SAWs) [10], magnetic forces [11], and dielectrophoretic forces [12]. Machine learning [9], artificial intelligence [13], and coupling with downstream microarray based systems [14] are a natural progression of the field and have been applied.

Previously our group developed an image-guided cell sorter using a fast scanning laser as the excitation source [15]. In a simple microfluidic device suitable for low-cost, disposable

applications that minimizes cross contamination [16], one-dimensional flow focusing confines the procession of cells into the center of the microfluidic channel only in one axis perpendicular to the flow direction. In the other perpendicular axis, however, the cell positions are not confined. As a result, particles in the flow channel tend to have a wide distribution in their positions affected by their size, stiffness, shape, and morphology. To extract image related features of high fidelity, keeping the cells at the focal spot of the interrogating beam is essential. Cells positioned outside the focal depth of the interrogating beam will give rise to blurred images. Furthermore, given the typical 10-15 μm cell size, even for the cells located in the focal plane, a significant portion of the cell features can be out of focus. As a result, today's image-guided flow cytometer cell sorters using a tightly focused Gaussian beam from a high numerical aperture (NA) objective face two major challenges: (a) to keep cells of different properties in the flow channel all in focus and (b) to keep all parts of the cells across their thickness along the optical axis in focus. Inability to meet the former requirement gives rise to a large number of out-of-focus cells, resulting in low throughput and biased analysis since some cell subpopulations tend to be in focus more than others. Failure to meet the latter requirement increases the risk of misleading the gating criteria for sorting since the apparent crisp cell image represents only the feature of one cross section of the cell, leaving features outside the focal plane blurry or not detectable. In this paper, we demonstrate a scanning Bessel beam system with extended focal depth to overcome the above limits and develop innovative approaches to perform image-guided cell sorting in a disposable microfluidic cartridge. The sorting criteria were directly determined from the image-encoded temporal waveform without image restoration. The system is simple to set up and can operate in a label-free manner.

Although not used in a flow cytometer system before, Bessel beam-based illumination microscopy methods have previously been leveraged to increase the depth of focus in biological

specimens with near-isotropic spatial resolution, achieving significant merit in light-sheet microscopy, illumination microscopy, and electron microscopy [17-19]. A Bessel beam is a diffraction-free mode solution of the Helmholtz equation and possesses a number of unique properties which make it useful for imaging applications, including non-diffractive behavior and the ability to self- heal when partially obstructed [20]. A mathematically ideal Bessel beam cannot exist as it is unbounded and carries an infinite amount of energy. An experimentally achievable approximation is to modulate the Bessel beam by a broad width Gaussian function, which is called a Bessel-Gaussian beam. The most used method of generating the Bessel-Gaussian beam is by illuminating a conically shaped element called an axicon with a Gaussian beam [21].

Here we demonstrate an imaging flow cytometer and cell sorter with an ultra-long depth of focus, accomplished by a scanning Bessel-Gaussian laser beam. The two-dimensional cell images can be reconstructed from one dimensional waveform information collected from a photomultiplier tube (PMT). From this waveform, a number of cellular morphological features are quantified, and these values can be used to create appropriate gates for cell sorting. Sorting is accomplished via an integrated piezoelectric (PZT) actuator as previously described [15][16][22]. The PZT-integrated microfluidic device is made of cyclo-olefin copolymer (COC) material integrated with a cartridge that contains microfluidic channels and interfaces with the fluidic pumps. Both the microfluidic chip and the cartridge are injection molded and can be disposed to eliminate concerns of cross contamination.

Experiments were conducted to evaluate the sorting performance of the system for multiple sizes of polystyrene beads, label-free identification and sorting of acute myeloid leukemia (AML) cells from white blood cells, and the label-free sorting of *Scenedesmus sp*., a green algae, from field-collected microorganisms. Our results indicate a sorting accuracy of 97%, 97%, and 98%,

respectively. We also demonstrate an increased percentage of in-focus cell images from 30-40% for a Gaussian beam system to >85% by using a Bessel Gaussian beam, effectively increasing the throughput by about three folds to around 300 cells/second, limited by the response of the on-chip piezoelectric actuator and the presence of cell doublets.

1.3 PRINCIPLE AND METHODS

1.3.1 Design of the imaging system

The optical system design is shown in Figure 1.1(a). The Gaussian beam output from a 488nm diode laser illuminates on an axicon (AX1025-A, Thorlabs) with an angle of 0.5º. A Bessel-Gaussian beam is formed by the superposition of two sets of plane waves propagating with a cone angle. The Bessel-Gaussian beam is then modulated by an acousto-optic deflector (OAD948, Isomet). The acoustic transducer deflects the beam to different angles along the y- (scanning) direction (Figure 1.1(a)) at a frequency of 200KHz. Lens1 performs a Fourier transform of the zero order Bessel-Gaussian beam to create an annulus-shaped beam at its focal plane. This annulus-shaped beam is then magnified by lens2 before reaching the exit pupil of a 10X illumination objective lens (378-803-3, Mitutoyo). The illumination objective lens transforms the annulus-shaped beam back to a Bessel-Gaussian beam onto the cells in the microfluidic channel. The position of the AOD is conjugate with the back focal plane of the objective lens. This schematic creates a fan scan of the laser beam at the front focal plane. The microfluidic chip, which is made of cyclic olefin copolymer (COC) as shown in Figure 1.1(b), is put at the front focal plane.

Our design uses a single PMT detector and an AOD-scanned CW laser to encode the 2D cell transmission profile into a temporal signal, which can be used as the gating criteria for cell sorting and classification. A spatial mask (mask2, Figure 1.1(a)) with one 500μm x 15μm slit is put at the image plane of the 488nm laser channel, which creates a 50μm x 1.5μm transparent area

at the focal plane. The slit is aligned to the center of the Bessel-Gaussian beam. As a result, the sidelobes of the Bessel-Gaussian beam along the flow direction are blocked while the sidelobes along the scanning direction can pass the slit.

Since cell speed in the microfluidic channel is position dependent and the speed information is required to correctly relate the temporal waveform to the cell image, we use a 455 nm LED, a PMT, and a spatial mask (mask1, Figure 1.1(a)) to detect the speed of each individual cell.[12] The spatial mask contains two 1mm x 10μm slits separated in the cell flow (z-) direction, placed at the image plane of 455nm LED channel. The speed of each cell is obtained by dividing the slit distance with the magnification factor (10x in our case) and the time difference between the minima in the LED transmission signal. In our experiment, cell speeds are typically between 10 cm/s and 25 cm/s with an average speed of around 20 cm/s.

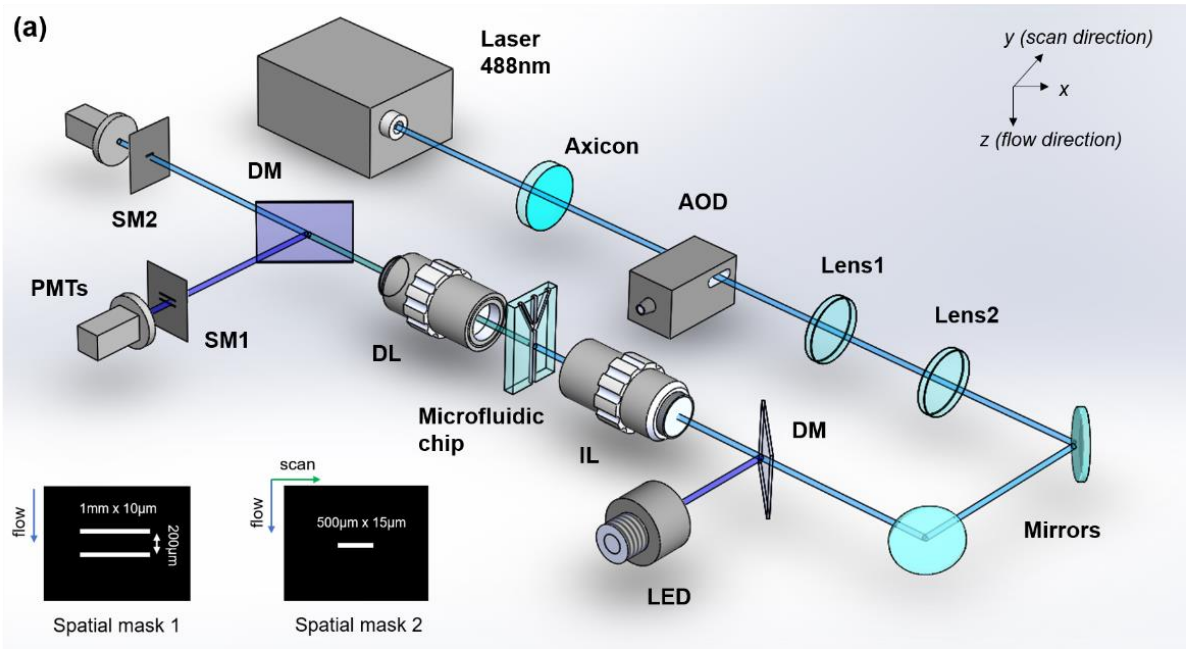

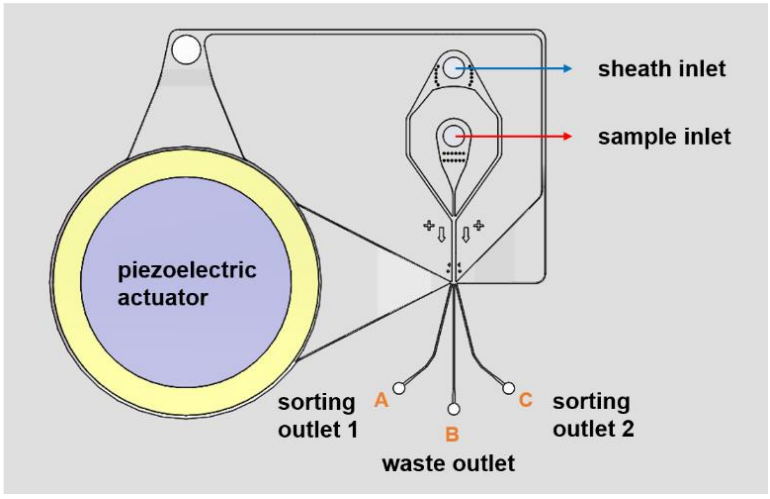

(b)

Figure 1.1: (a) Optical imaging system design. AOD, acousto-optic deflector; DM, dichroic mirror; IL, 10×/0.28 illumination objective lens; DL, 10×/0.28 detection objective lens; PMTs, photomultiplier tubes; and SM: spatial filter. The spatial masks for cell speed detection and transmission imaging are shown on the bottom left. (b) Microfluidic chip design. The chip is made of cyclic olefin copolymer (COC) by injection molding.

The microfluidic sorting chip was made of COC (Cyclic Olefin Copolymer) by injection molding. COC was chosen due to its high transparency in the visible wavelength, low autofluorescence, and low fabrication cost. The piezoelectric actuator was attached to the top of

the COC microchip via a thin layer of double-sided PSA (pressure sensitive adhesive). The sample stream is focused by the sheath flow hydrodynamically. When a target cell is detected, the piezo-actuator is triggered to push or pull the target cell to sorting outlet 1 or 2 and eventually into either the collection tubes or specific wells in a 384-well plate. Cells that are not of interest travel through the center channel to the waste outlet.

1.3.2 Simulation of the Bessel Gaussian beam transmission signal

To gain insight into the transmission of a Bessel Gaussian beam through an object, we use COMSOL Multiphysics simulation software to show how a 7μm bead (n=1.6) changes the optical intensity distribution of a Bessel-Gaussian beam (Figure 1.2). Since our system measures the far field of the transmitted light, we simulate the electric field distribution 400μm away from the bead to satisfy the Fraunhofer far-field condition. When there is no object in the interrogation zone, the laser light transmits through the slit and generates a constant DC background. When the laser beam intersects the bead, the light will be partially reflected and partially diffracted. If the diffraction angle θ is greater than the collection angle of the detection objective lens, the light intensity on the PMT decreases, resulting in a dark region in the transmission image of the 7μm bead due to the combined effects of reflection and diffraction assuming the effect of light absorption is negligible. According to the simulation, when the Bessel-Gaussian beam hits the center of the 7μm bead, the calculated diffraction angle θ is around 2 degrees, much smaller than the collection angle of the detection objective (10X, NA = 0.28). Thus the small angle diffraction beam can pass the slit and reach the PMT, producing a “bright spot” at the center of the image of the bead. This explains why we observe a bright spot at the center of the restored bead image from the transmitted signal (Figure 1.2(b)). As a general rule, areas of large optical density and large angle scattering give rise to dark

regions; and areas of low optical density and small angle scattering give rise to bright regions in the restored transmission images.

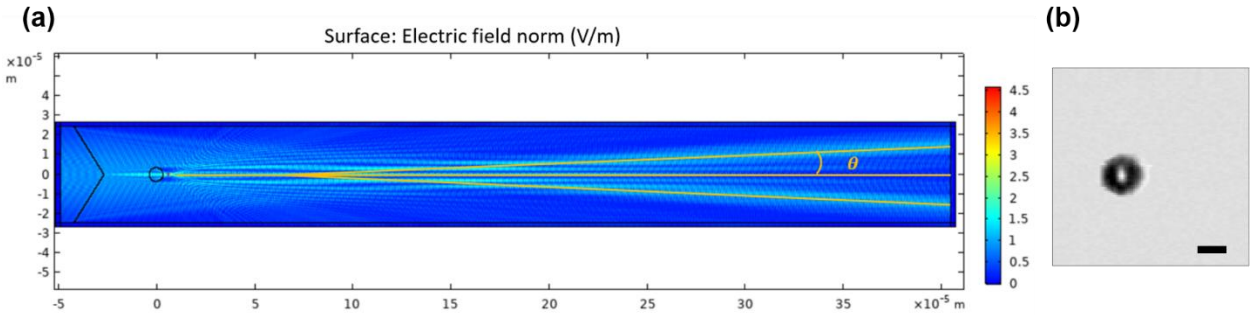

Figure 1.2: (a) COMSOL simulation of the electric field when a Bessel-Gaussian beam illuminates on the center of a 7μm bead. (b) Example transmission image of a 7μm bead generated by the image-guided cell sorter using a scanning Bessel-Gaussian beam. The image was reconstructed using the mathematical algorithm discussed in Section D. Scale bar: 5μm

1.3.3 Depth of focus comparison

The main motive of using a Bessel Gaussian beam to replace a Gaussian beam is to extend the focal depth such that objects in different positions in a microfluidic channel and different cross sections of the cell can all be focused to generate high fidelity 2D cell image information. Figure 1.3 shows the intensity profile and focal depth of the Bessel Gaussian beam measured by a camera. Figures 1.3(a) and (b) show the intensity profile of the Bessel Gaussian beam at the image plane. The full width half maximum (FWHM) of the center lobe is between 1 μm and 1.5 μm. As expected, a significant amount of energy is in the side lobes, which excite areas outside the central spot and complicate the waveform analysis when we use a single PMT for detection to keep the system simple and at low cost. A mathematical algorithm to be discussed in the next section is required to deconvolve the signal when we reconstruct the transmission image. To measure the focal depth, beam profiles at different depths are recorded by moving the detection objective lens along the beam propagation (x-) direction. Both the maximum intensity and FWHM of the center

lobe have relatively small changes within a distance of 160μm, as shown in Figure 1.3(c)). In contrast, a Gaussian beam produced by the same objective lens has a much shorter focal depth of about 7.37 μm.

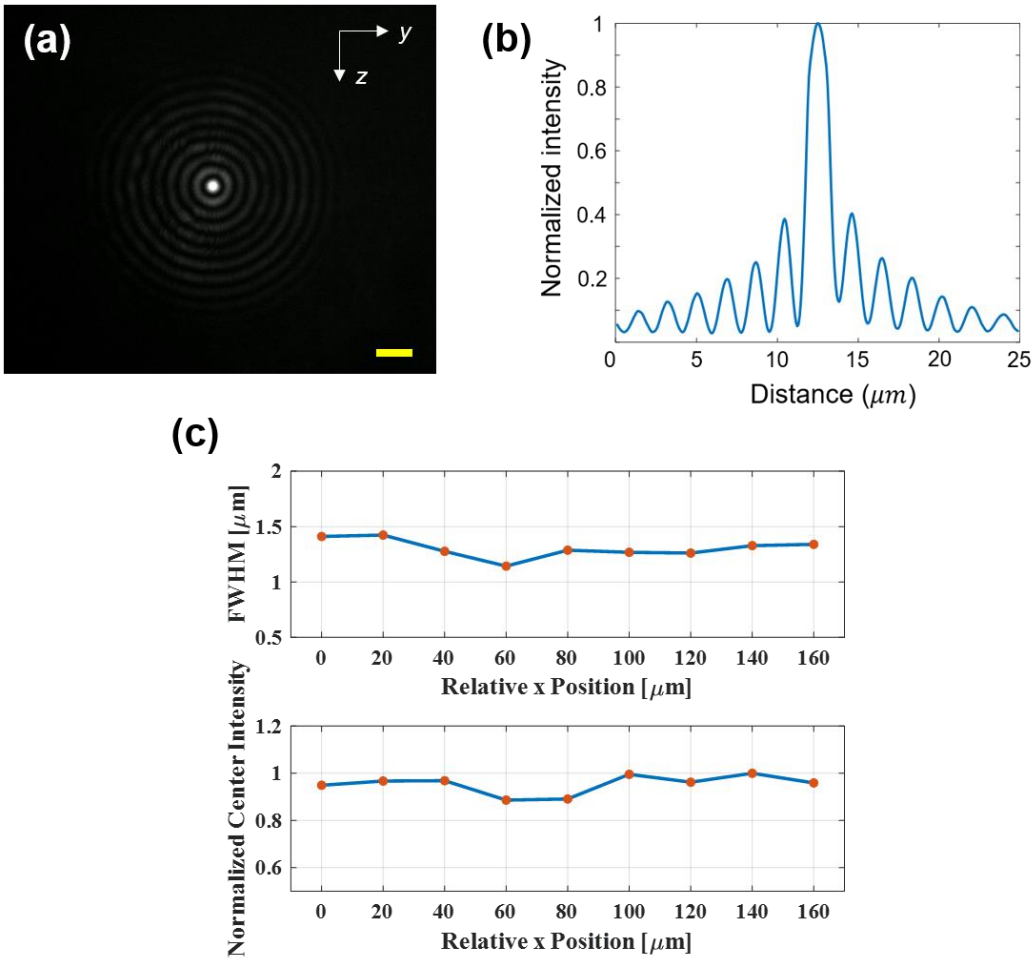

Figure 1.3: Bessel-Gaussian beam profile. (a) Camera measured beam profile at the image plane. (b) Normalized intensity from the center of the Bessel-Gaussian beam. (c) Full-width-half-maximum and normalized light intensity of the main lobe of Bessel-Gaussian beam.

To assess how the extended focal depth of a Bessel-Gaussian beam can improve the detection yield compared to a Gaussian beam, we ran a mixture of cells and beads, including 15μm beads, 7μm beads, HEK 293T cells, MCF7 cells and Hela cells, in both Gaussian beam and Bessel-Gaussian beam image-guided cell sorters. The results are summarized in Table 1.1. In the Gaussian beam system, the short focal depth cannot keep the majority of objects in focus due to the wide

distribution of the objects along the microfluidic channel. Except for 15μm beads that tend to take a stable position in the channel, only 30-40% 7μm beads, and only 40-60% cells are in focus. In sharp contrast, > 90% of 7μm beads, 98% of 15μm beads, and 85% of cells of all kinds are in focus in the Bessel-Gaussian beam system.

Figure 1.4 shows example in-focus and out-of-focus 15μm bead and 7μm bead images generated by the Gaussian beam system. In sharp contrast, the vast majority of both 15μm and 7μm diameter beads are well focused for the Bessel-Gaussian beam system.

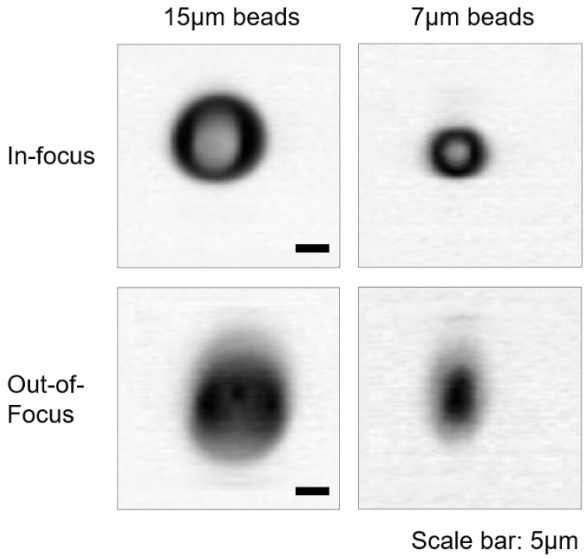

Figure 1.4: Examples of in-focus (first row) and out-of-focus (second row) images for 15μm and 7μm beads, generated by a scanning Gaussian beam image-guided cell sorter. In comparison, nearly all images from the scanning Bessel Gaussian beam system are well in focus (see Fig. 5). Scale bar: 5μm

Table 1.1: Comparison of the ratio of in-focus objects between the scanning Gaussian beam system and the scanning Bessel-Gaussian beam system.

	Gaussian System	Bessel- Gaussian System
7μm Beads	30%-40%	90%-95%
15μm Beads	~98%	~98%
Cell Mixture	40%-60%	85%-90%

1.3.4 Image reconstruction algorithm

In this section we describe the mathematical algorithm to reconstruct images from the label-free, transmission signal by a Bessel Gaussian beam. It is noted that because of the correlation between the PMT temporal signal and the image features, we do not need to use the restored cell images as gates to sort cells. Instead, we sort cells directly from the features in the waveform, thus saving time and resources for real time signal processing. Therefore, image reconstruction can be performed off-line for validation of the results and improved human-machine interface when users would like to observe image differences between sorted and unsorted cells and visualize image related features such as size, shape, granularity, contrast, etc.

The electric field of a Bessel-Gaussian beam can be written as

$$\boldsymbol{E_{BG}(r,x) = E_0 J_0(k_r r)\frac{w_0}{w(x)} e^{-\frac{r^2}{w_0^2}} \cdot e^{-ik_x x} e^{-i\emptyset}} \qquad (1)$$

where $\boldsymbol{r = \sqrt{y^2 + z^2}}$ is the distance from the center of the Bessel Gaussian beam. $\boldsymbol{E_0}$ is a field amplitude constant. $\boldsymbol{k_r}$ is the wavevector in the transverse plane and $\boldsymbol{{k_r}^2 + {k_x}^2 = k^2}$. $\boldsymbol{w_0}$ is the waist width of Gaussian amplitude. $\emptyset = \boldsymbol{tan^{-1}\frac{x}{x_0}}$. $\boldsymbol{x_0}$ is Rayleigh length of the Gaussian beam.

We use $\boldsymbol{n(x,y,z)}$ to denote the cell or bead index profile $\boldsymbol{n(x,y,z) = n_o + \Delta n(x,y,z)}$. We assume $\boldsymbol{n_o}$ is the index of water and $\boldsymbol{\Delta n > 0}$ since the index of cells and beads is greater than the index of water. Assume cell or bead thickness is within $\boldsymbol{x_c}$. For the 2D imaging system, we cannot resolve index change along the beam propagation direction, so we make the following approximation:

$$\int_0^{x_c} \Delta \boldsymbol{n(x,y,z)dx} = \Delta \bar{\boldsymbol{n}}(\boldsymbol{y,z})\boldsymbol{x_c} \qquad (2)$$

Adding a slit in parallel with the laser scanning (y-) direction on the image plane and assuming the slit is narrow enough to be approximated by a 1-D delta function in its transmission characteristic, the transmitted field focused by a lens and after the slit can be approximated by (3).

$$\boldsymbol{E_t(y',z') = E_0' e^{-ik_o x} e^{-i\emptyset} \frac{w_0}{w(x)} \int_y \int_z \delta(z-z') \times \left(\frac{2\sqrt{n_o(n_o+\Delta\bar{n}(y,z))}}{2n_o+\Delta\bar{n}(y,z)}\right) \times}$$
$$\boldsymbol{J_0\left[k_r\sqrt{(y'-y)^2+(z'-z)^2}\right] \times e^{-\frac{(y'-y)^2+(z'-z)^2}{w_0^2}} e^{-ik_o\Delta\bar{n}(y,z)x_c} dydz} \qquad (3)$$

The term $\left(\frac{2\sqrt{n_o(n_o+\Delta\bar{n}(y,z))}}{2n_o+\Delta\bar{n}(y,z)}\right)$ in Eq. (3) is the approximate transmission coefficient assuming there is no absorption. Here $(\boldsymbol{y,z})$ refers to the transverse coordinate in the object plane, and $(\boldsymbol{y',z'})$ refers to the transverse coordinate in the image (detection) plane. For simplicity, we have transformed the actual position $(\boldsymbol{Y',Z'})$ in the image plane into $(\boldsymbol{y',z'})$ by defining $\boldsymbol{y' = \frac{Y'}{M}}$ and $\boldsymbol{z' = \frac{Z'}{M}}$ with M being the magnification of the detection optics.

Also note that $(\boldsymbol{y',z'})$ is related to the time by the following relations:

$$\boldsymbol{y' = \frac{FOV_y}{T}\, t} \qquad (4\text{-a})$$
$$\boldsymbol{z' = v_{flow} t} \qquad (4\text{-b})$$

where $\boldsymbol{FOV_y}$ is the field-of-view in the y- (scanning) direction, T is the time for each AOD scan (5 $\boldsymbol{\mu}$s in our system), and $\boldsymbol{v_{flow}}$ is the flow speed of the object (around 20 cm/s in our system). For a 40$\boldsymbol{\mu}$m field-of-view in the scanning direction and an AOD scanning period of 5$\boldsymbol{\mu}$s, the scanning speed is 8m/s, which is 40 times faster than the average cell travel speed. This allows us to treat the scanning along the y-axis as if the cell is nearly still in the z-axis.

From the relations in (4), we can relate a signal in time domain to the space domain, thus reconstructing the image from a temporal waveform.

To analyze the detected cell transmission signal behind the slit when the center of the scanning Bessel Gaussian beam is at a given position in the flow ($\boldsymbol{z'}$-) direction, we can represent the transmitted field in (5) under a given position $\boldsymbol{z'}$.

$$\boldsymbol{E_t(y')|_{z'} \propto \int_y \left(\frac{2\sqrt{n_o(n_o+\Delta\bar{n}(y)|_{z'}}}{2n_o+\Delta\bar{n}(y)|_{z'}}\right) J_0\left[k_r\sqrt{(y'-y)^2}\right] e^{-\frac{(y'-y)^2}{w_0^2}} e^{-ik_o\Delta\bar{n}(y)|_{z'}x_c} dy} \qquad (5)$$

Equation (5) shows that $\boldsymbol{E_t(y')|_{z'}}$ is the convolution of the index function $\left(\frac{2\sqrt{n_o(n_o+\Delta\bar{n}(y)|_{z'}}}{2n_o+\Delta\bar{n}(y)|_{z'}}\right) e^{-ik_o\Delta\bar{n}(y)|_{z'}x_c}$ and the Bessel Gaussian function $\boldsymbol{J_0[k_r y]e^{-\frac{y^2}{w_0^2}}}$ along the scanning (y-) direction. To save computational power for image reconstruction, we approximate the Bessel function $\boldsymbol{J_0[k_r y]}$ by a series of delta functions at its maxima and minima:

$$\boldsymbol{J_o(u) \sim \sum_m c_{max,m}\delta(u-u_{max,m}) + \sum_n c_{min,n}\delta(u-u_{min,n})} \qquad (6)$$

$\boldsymbol{u_{max,m}}$: positions of *mth* maximum of $\boldsymbol{J_o(u)}$. $\boldsymbol{J_o(u_{max,m}) > 0;\ m = 0, \pm1, \pm2, \pm3, \cdots}$

$\boldsymbol{u_{min,n}}$: positions of *nth* minimum of $\boldsymbol{J_o(u)}$. $\boldsymbol{J_o(u_{min,n}) < 0;\ n = \pm1, \pm2, \pm3, \cdots}$

The coefficients for each delta function are defined as

$$c_{max,m} = J_0(u_{max,m}) \quad m = 0, \pm 1, \pm 2, \pm 3, \cdots$$

$$c_{min,n} = J_0(u_{min,n}) \quad n = \pm 1, \pm 2, \pm 3, \cdots$$

Substituting (6) into (5) and dropping the parameter z' for simplicity, we obtain the following approximate expression of the transmitted E-field behind the slit,

$$E_t(y')|_{z'} \sim \left[\sum_m C_{max,m} exp\left[-\frac{u_{max,m}^2}{(k_r w_o)^2} \right] \left(\frac{2\sqrt{n_o(n_o + \Delta\bar{n}\left(y' - \frac{u_{max,m}}{k_r}\right)|_{z'}}}{2n_o + \Delta\bar{n}\left(y' - \frac{u_{max,m}}{k_r}\right)|_{z'}} \right) e^{-ik_o \Delta\bar{n}\left(y' - \frac{u_{max,m}}{k_r}\right)|_{z'} x_c} \right] -$$

$$\left[\sum_n C_{min,n} exp\left[-\frac{u_{min,n}^2}{(k_r w_o)^2} \right] \left(\frac{2\sqrt{n_o(n_o + \Delta\bar{n}\left(y' - \frac{u_{min,n}}{k_r}\right)|_{z'}}}{2n_o + \Delta\bar{n}\left(y' - \frac{u_{min,n}}{k_r}\right)|_{z'}} \right) e^{-ik_o \Delta\bar{n}\left(y' - \frac{u_{min,n}}{k_r}\right)|_{z'} x_c} \right] \quad (7)$$

Representing $E_t(y') \sim A - B$ in brief form, we can write the transmitted power through the slit as

$$J_t(y')|_{z'} \propto {E_t}^*(y')|_{z'} E_t(y')|_{z'} \propto AA^* + BB^* - AB^* - BA^* \quad (8)$$

It can be shown that (8) can be approximated as

$$J_t(y', x) \sim \frac{4n_o(n_o + \Delta\bar{n}(y')|_{z'}}{(2n_o + \Delta\bar{n}(y')|_{z'})^2} + \left[\sum_{m \neq 0} {C_{max,m}}^2 exp\left[-\frac{2u_{max,m}^2}{(k_r w_o)^2} \right] \frac{4n_o(n_o + \Delta\bar{n}\left(y' - \frac{u_{max,m}}{k_r}\right)|_{z'}}{\left(2n_o + \Delta\bar{n}\left(y' - \frac{u_{max,m}}{k_r}\right)|_{z'}\right)^2} \right] +$$

$$\left[\sum_n {C_{min,n}}^2 exp\left[-\frac{2u_{min,n}^2}{(k_r w_o)^2} \right] \frac{4n_o(n_o + \Delta\bar{n}\left(y' - \frac{u_{min,n}}{k_r}\right)|_{z'}}{\left(2n_o + \Delta\bar{n}\left(y' - \frac{u_{min,n}}{k_r}\right)|_{z'}\right)^2} \right] \quad (9)$$

To obtain (9), we have ignored summations of terms with a random phase φ_{mn} such as $\sum_{m,n} e^{-i\varphi_{mn}}$ where $\varphi_{m,n} = k_o x_c [\Delta\bar{n}\left(y' - \frac{u_{max,m}}{k_r}\right)|_{z'} - \Delta\bar{n}\left(y' - \frac{u_{min,n}}{k_r}\right)|_{z'}]$. In other words, we have only kept the phase-matched terms with $\varphi_{mn} = 0$.

According to (9), when the beam center hits a high index spot, $\frac{4n_o(n_o + \Delta\bar{n}(y')}{(2n_o + \Delta\bar{n}(y'))^2}|_{z'} < 1$, the light intensity through the slit yields a lower than 100% transmission. When the beam center hits

a low index position (e.g. water only), the first term in (9) is maximum, but the values in the second and third term depend on the index values $\Delta\bar{\boldsymbol{n}}\left(\boldsymbol{y}' - \frac{\boldsymbol{u}_{max,m}}{\boldsymbol{k}_r}\right)|_{z'}$ and $\Delta\bar{\boldsymbol{n}}\left(\boldsymbol{y}' - \frac{\boldsymbol{u}_{min,n}}{\boldsymbol{k}_r}\right)|_{z'}$ relative to the maxima and minima of the side lobes. In order to reconstruct the image from the measured PMT signal, we need to solve $\Delta\bar{\boldsymbol{n}}(\boldsymbol{y})|_{\boldsymbol{z}}$ or simply $\Delta\bar{\boldsymbol{n}}(\boldsymbol{y},\boldsymbol{z})$. Next, we describe the algorithm to obtain $\Delta\bar{\boldsymbol{n}}(\boldsymbol{y},\boldsymbol{z})$ from eq. (9).

Define $\boldsymbol{f}(\boldsymbol{y},\boldsymbol{z}) = \frac{4\boldsymbol{n}_o(\boldsymbol{n}_o+\Delta\bar{\boldsymbol{n}}(\boldsymbol{y}))}{(2\boldsymbol{n}_o+\Delta\bar{\boldsymbol{n}}(\boldsymbol{y}))^2}|_{\boldsymbol{z}}$. By solving $\boldsymbol{f}(\boldsymbol{y},\boldsymbol{z})$, we can know the index profile of the object $\Delta\bar{\boldsymbol{n}}(\boldsymbol{y},\boldsymbol{z})$.

Equation (9) can be represented in matrix form as

$$\boldsymbol{J}_t[\boldsymbol{y}'_1,\boldsymbol{y}'_2,\cdots,\boldsymbol{y}'_N;\boldsymbol{z}'_j] = [\mathrm{T}] * \boldsymbol{f}[\boldsymbol{y}'_1,\boldsymbol{y}'_2,\cdots,\boldsymbol{y}'_N;\boldsymbol{z}'_j] \qquad (10)$$

where $\boldsymbol{j}$ denotes the z-position of the cell in the flow direction after $\boldsymbol{j}$ times of AOD scans. The T-matrix is a 251x251 matrix. The dimension of the matrix is determined as follows: At a sampling rate of 25 MS/s and for a single scan of 5μs, we produce 125 data points corresponding to the center positions of the Bessel Gaussian beam over the 40μm scanning range. However, the Bessel Gaussian beam has side lobes. Assuming that the side lobes on each side of the beam center span 20μm, we have the scanning Bessel Gaussian beam cover a total range of 80μm, thus producing a total of 251 points in the transfer matrix in (10). The elements of the T-matrix are defined as follow:

$\boldsymbol{T}_{ij} = \mathbf{1}. \quad \boldsymbol{if} \quad \boldsymbol{i} = \boldsymbol{j}, \quad -\mathbf{65} \le \boldsymbol{i},\boldsymbol{j} \le \mathbf{185}$

$\boldsymbol{T}_{ij} = \boldsymbol{C_l}^2 \boldsymbol{exp}\left[-\frac{2\boldsymbol{u}_l^2}{(\boldsymbol{k}_r\boldsymbol{w}_o)^2}\right] \equiv \boldsymbol{a}_l^2$ where $\boldsymbol{u}_l$ is the $\boldsymbol{lth\ min}$ or $\boldsymbol{max}$ for $\boldsymbol{J_0}(\boldsymbol{u})$ if $\boldsymbol{y}'_i - \frac{\boldsymbol{u}_l}{\boldsymbol{k}_r} = \boldsymbol{y}'_j$

$\boldsymbol{T}_{ij} = \mathbf{0}$. Otherwise (11)

Then $\Delta\bar{\boldsymbol{n}}(\boldsymbol{y},\boldsymbol{z})$ can be obtained from Eq. (12),

$$\boldsymbol{f}\left[\boldsymbol{y}'_{\boldsymbol{1}}, \boldsymbol{y}'_{\boldsymbol{2}}, \cdots, \boldsymbol{y}'_{\boldsymbol{N}}; \boldsymbol{z}'_{\boldsymbol{j}}\right] = [\boldsymbol{T}]^{-\mathbf{1}} * \boldsymbol{J}_{\boldsymbol{t}}\left[\boldsymbol{y}'_{\boldsymbol{1}}, \boldsymbol{y}'_{\boldsymbol{2}}, \cdots, \boldsymbol{y}'_{\boldsymbol{N}}; \boldsymbol{z}'_{\boldsymbol{j}}\right] \qquad (12)$$

From Eq. (12), we can reconstruct the transmission image of the object from the PMT signal. More detailed analyses can be found in the supplementary material.

1.3.5 Waveform-based real-time sorting

The mathematical algorithm in the previous section can recover the object image from the PMT signal. However, the computation of 251x251 matrix multiplication is time-consuming and can limit the throughput. Because most cell features, including size, spottiness, granularity, etc., are encoded in the PMT output waveform, we can extract many image features that differentiate cell types directly from the temporal waveform without reconstructing the 2D cell images. This saves tremendous computation time and resources, and the method is suitable for cell sorting by image features. For all sorting experiments reported in this paper, we define gating based on the characteristics of the temporal waveform, which are closely correlated to specific image features. We then use the mathematical algorithm discussed in the previous section to reconstruct the cell transmission images off-line for verification purposes. To quantify sorting accuracy, we also apply additional methods such as staining and microscopy to verify the performance of waveform-based image-guided cell sorting.

Figure 1.5 shows an example of how the temporal waveform carries features about particle size and how we can use the waveform features to distinguish 15μm and 7μm diameter beads. When there is no object in the microfluidic channel, the scanning Bessel Gaussian beam transmits through the slit and the PMT shows a periodic background signal, caused by any imperfections or dust particles in the COC microfluidic chip intersected by the laser beam. Since these features are still, they appear to be periodic in each scan and can be subtracted by software. When a cell or

bead travels through the optical interrogation area, it creates an instantaneous change in the PMT output signal on top of the background. The PMT waveforms in Figures 1.5(a-i) and 1.5(b-i) show an envelope with a series of spikes. Each spike represents a single scan spanning a duration of 5μs, and the width of the spike is proportional to the size of the bead along the scanning (y-) direction. The width of the overall signal envelope is proportional to the dimension of the bead in the flow direction after correction of the effect of the flow speed. Based on this argument, we develop the following sorting criterion that is equivalent to the particle size:

We find the time interval between the first negative peak and the last negative peak $\boldsymbol{T_1}$, which corresponds to the duration when the bead crosses the optical interrogation zone defined by the width of the slit in the spatial mask. The bead length $\boldsymbol{L}$ along the flow direction equals $\boldsymbol{T_1 * v_{bead}}$, where $\boldsymbol{v_{bead}}$ is bead traveling speed. We then analyze the detailed waveform of each 5μs scan (labelled by "*" in the envelope waveform) to find the bead dimension in the scanning direction. Figures 1.5(a-ii) and (b-ii) show the detailed waveform of each 5μs scan at a given z position. By slicing the object into N sections along the z-position, the object width at the nth section can be represented as $\boldsymbol{T_2^n * v_{scan}}$ with $\boldsymbol{n}$ being the index of the z-position and $\boldsymbol{v_{scan}}$ is the beam scanning speed ($\boldsymbol{v_{scan} = 8m/s}$). Figure 1.5(a-ii) shows two (10th and 16th) of such scans for a 15μm bead. The 10th scan gives the largest value of $\boldsymbol{T_2^n * v_{scan}}$, indicating the widest part (i.e. diameter) of the bead. Similar characteristics can be found in the waveform of 7μm beads. The above example demonstrates how one can relate the temporal waveform features to the geometric features of a travelling object such as size, shape, aspect ratio, etc.

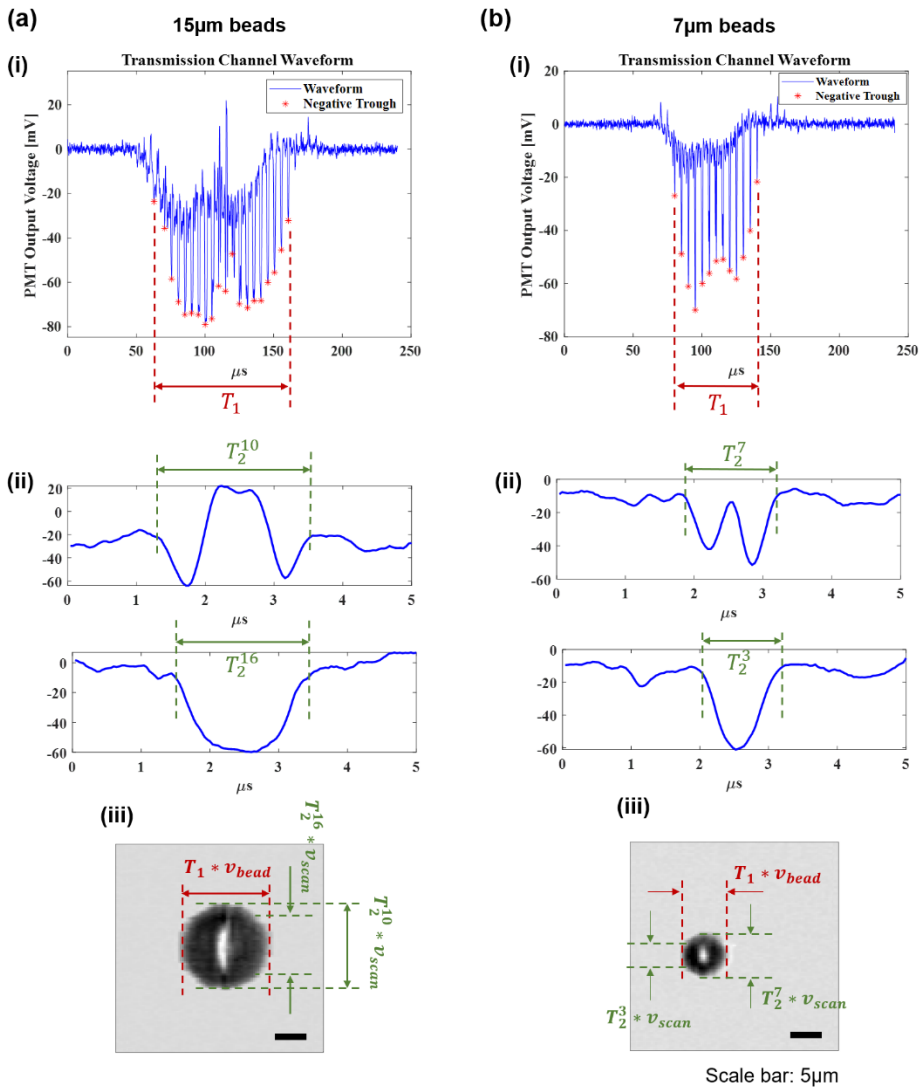

Figure 1.5: Transmission PMT signals for 15μm and 7μm beads and reconstructed images. Scale bar: 5μm. (i) The overall signals. Each "*" represents the peak of each scan. The product of the bead speed v_bead and the width of the overall envelope T_1 produces the bead dimension along the flow direction. (ii) Detailed waveforms for a single 5μs AOD scan. At each specific z-position, the dimension of the bead along the scanning direction is T_2*v_scan where v_scan=8m/s is the beam scanning speed. (iii) Reconstructed transmission images of a 15 μm and 7 μm bead. The relations between the temporal waveforms and the image features are also indicated in the figures.

1.4 EXPERIMENTAL RESULTS

1.4.1 Sorting of 10 and 15μm beads

To validate the sorting algorithm described above, sorting was performed using 7μm, 10μm and 15μm beads. The histogram of $(\boldsymbol{T_1 * v_{bead}}) * (\boldsymbol{T_2 * v_{scan}})$ is shown in Figure 1.6(b).

To evaluate sorting performance, we sorted 10μm beads from a 1:1 mixture of 7μm and 10μm beads, as well as 15μm beads from a 1:1 mixture of 7μm and 15μm beads. The sorted beads were imaged using a microscope to verify the sorting accuracy. The first experiment demonstrated a sorting purity of 97%, verified by 233 microscope images; and the second experiment demonstrated 100% sorting purity, verified by 173 microscope images.

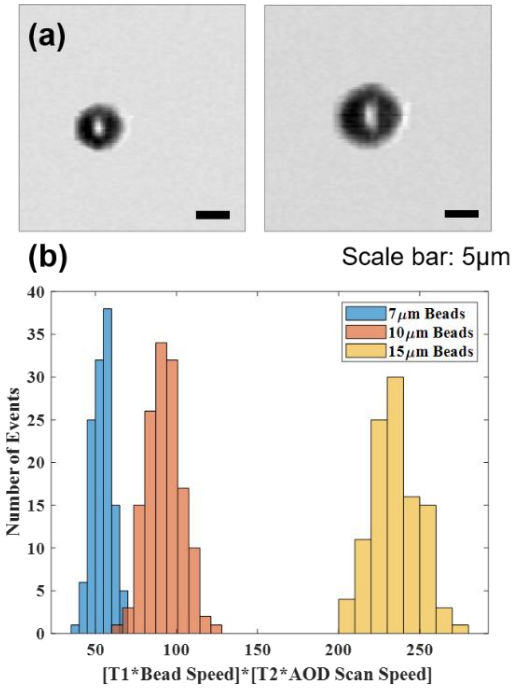

Figure 1.6: Images and histograms of polystyrene beads generated by the Bessel-Gaussian beam image-guided cell sorter. (a) Transmission images of polystyrene beads with 7μm (left) and 10μm (right) diameter. Scale bar: 5μm. (b) Histogram of (T_1*v_bead)*(T_2*v_scan) for 7μm, 10μm and 15μm beads.

1.4.2 Label-free sorting of leukemia cells

Blood cancers such as acute myeloid leukemia (AML) are estimated to account for 9.9% of the 1.8 million new cancer cases diagnosed in 2020 [16]. Leukemia, lymphoma and myeloma are expected to account for 9.4% of all cancer deaths in 2020 [17].

Acute myeloid leukemia is derived from the myeloid line of blood cells and is characterized by its rapid and unchecked growth of abnormal cells in the bone marrow that interferes with normal blood cell production. Diagnosis usually occurs via bone marrow aspiration or antibody-specific blood tests [18]. However, these require costly panels and tedious procedures. An image-guided cell sorter enables the identification and subsequent sorting of AML cells without any antibody or fluorescent labeling, aiding early detection and eliminating the need for costly reagents and tedious laboratory procedures.

In a proof-of-concept experiment, patient-derived SKNO1 acute myeloid leukemia (AML) cells were cultured in cell culture media (90% RPMI + 8% FBS + 1% penicillin + 1% streptomycin) at 37℃ with 5% CO_2. The SKNO1 cells were spiked into white blood cells from healthy donors (San Diego Blood Bank, 3636 Gateway Center Ave Suite 100, San Diego). A number of feature parameters were extracted from the transmission waveform of these cells, which are intuitively related to cell area, perimeter, granularity, roughness, contrast, and texture. The most distinguishing features between SKNO1 cells and white blood cells were determined to be $\boldsymbol{T_1 * v_{cell}}$ and the number of positive peaks of the waveform. The former is related to cell size and the latter to intracellular granularity. To demonstrate image-guided label-free cell sorting, a 2D plot of these parameters was generated and the appropriate gating parameters were chosen to sort SKNO1 cells from healthy white blood cells in a ratio of 1:50. To evaluate the cell sorting, Wright-Giemsa staining was performed. The full details for the staining procedure can be found in the supplementary material. The sorted cells were collected in a tube and deposited on a polyester transparent membrane filter (1300019, Sterlitech). Wright-Giemsa staining was performed and the stained cells were imaged using brightfield microscopy. A total of 124 SKNO1 cells were imaged

from a total of 128 cells found on the membrane, giving rise to a sorting purity of 97%. Given the initial population of 2% SKNO1 cells, the sorting has enriched the sample by 1600 times.

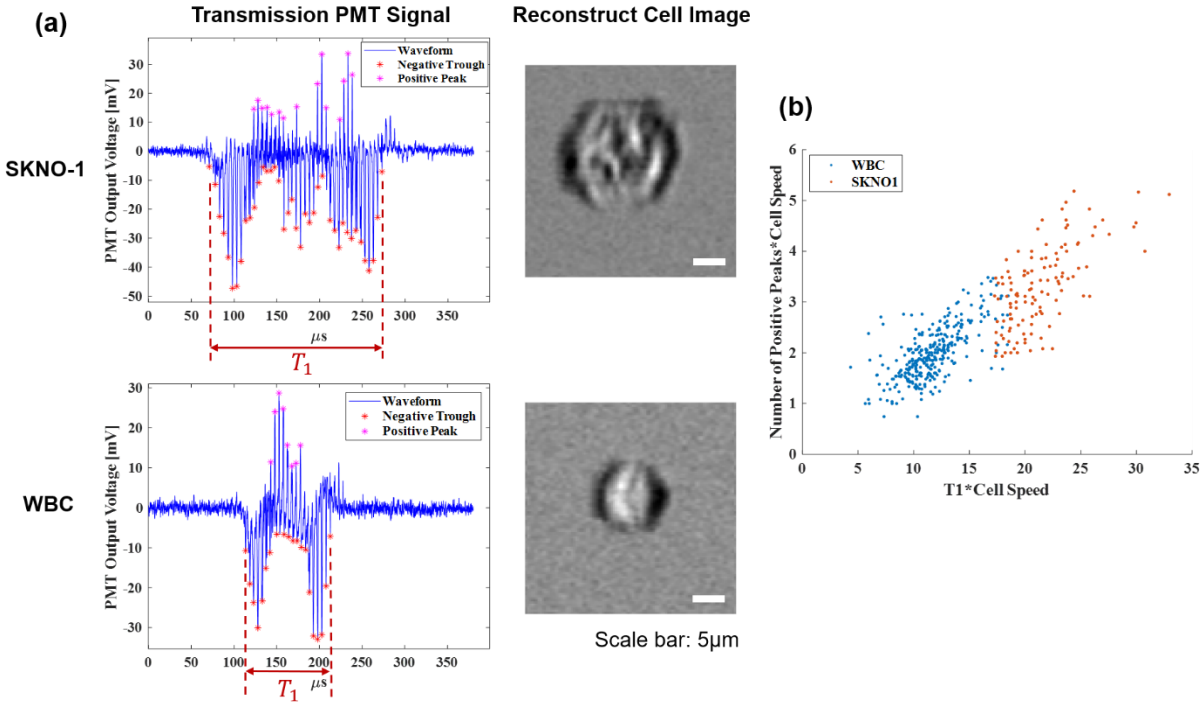

Figure 1.7: (a) Transmission PMT signals and images for SKNO-1 and WBC generated by the Bessel-Gaussian beam image-guided cell sorter. Scale bar: 5μm. (b) Distribution plots using these two parameters: T_1*v_cell and N*v_cell where N is the number of positive peaks in the PMT waveform. Multiplication of cell speed to both parameters removes feature distortions due to cell speed variations.

1.4.3 Label-free sorting of *Scenedesmus sp.*

Algae are a group of photosynthetic, eukaryotic organisms that can be found in oceans, waterways, lakes, and soils all over the world. Algae are commonly used to monitor environmental changes and have a number of industrial uses, including the production of biodiesel, ceramic products, glass products; in wastewater and oil spill cleanup; and in the biotechnology field as anticoagulant, antiviral and antitumor agents [26-29]. Despite their usefulness, little is known regarding the majority of these algae, with the estimated number of microalgae species exceeding

one million [19]. In comparison, the best algae culture collections often contain only a few thousand species [20]. Isolation of microalgae species from the environment is a useful and necessary approach to understanding these organisms and uncovering potential technological solutions. Traditionally, these organisms are isolated by hand using micropipettes or capillary tubes, or by fluorescence-activated cell sorting, and are subsequently cultured [21]. However, the throughput and usefulness of these approaches are limited, as microalgae and other microorganisms experience complex relationships with surrounding organisms that affect algae phenotype.

Scenedesmus sp. is one of the most common freshwater green algae. These colonial, non-motile algae have been researched for its high biomass productivity and its efficiency at capturing CO_2 [22]. *Scenedesmus* is capable of producing many types of biofuels and has been most extensively studied for biodiesel production. As there are over seventy taxonomically accepted species of *Scenedesmus*, including some with unique properties that only exist in local populations, the high-throughput identification and sorting of these algae from field-collected samples could unlock new opportunities [22].

As a proof-of-concept sorting experiment, *Scenedesmus* (Carolina Biological Supply, 152510) were spiked into field-collected microorganisms (Miramar Lake, San Diego, California) in a ratio of 1:5. The sample was run through a 35μm filter to remove clumps and large particles. The distinguishing feature of Scenedesmus from the other microorganisms was $\boldsymbol{T_1 * v_{algae}}$, which intuitively relates to size. A histogram with these parameters was generated and the appropriate portion was gated. The sorted samples were collected into tubes and visualized using brightfield microscopy. From a total of 253 sorted cells verified by microscope, 248 of them were Scenedesmus and 5 were other microorganisms, resulting in a sorting purity of 98%.

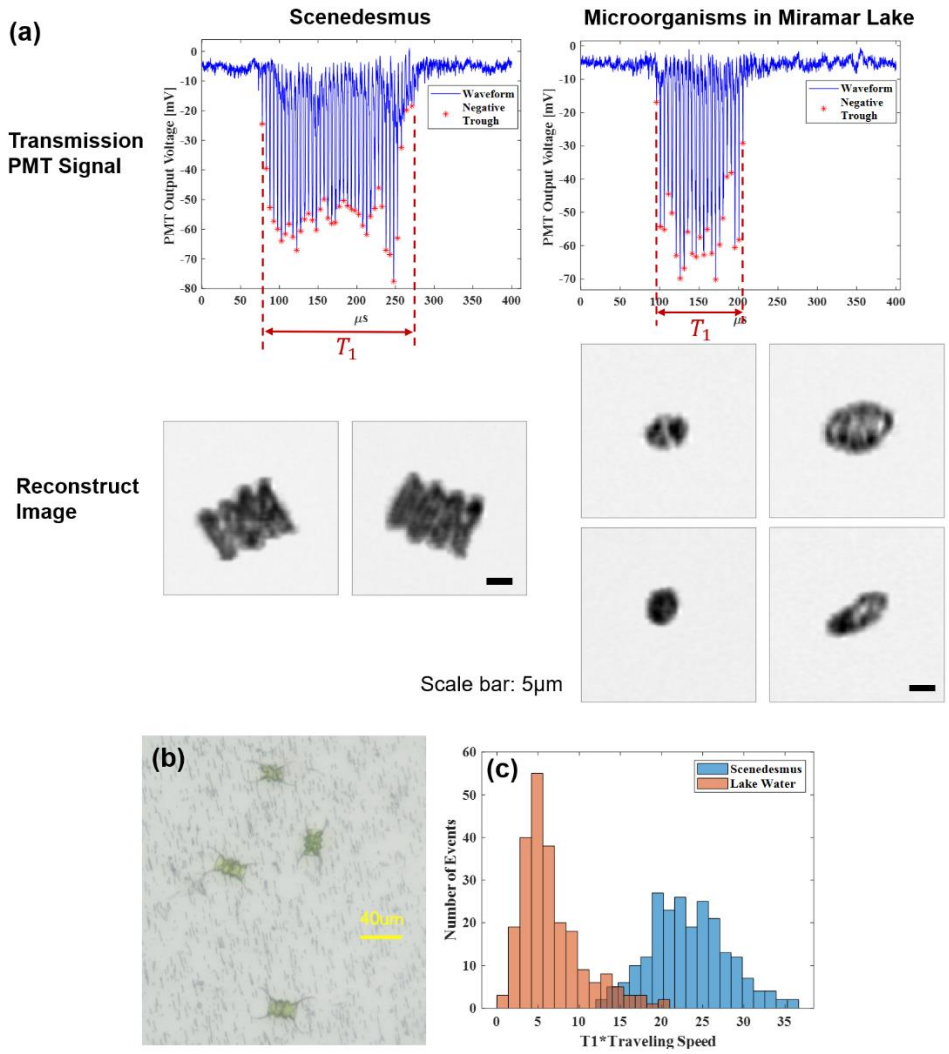

Figure 1.8: (a) Transmission channel waveforms and reconstructed images of Scenedesmus and microorganisms in Miramar Lake water. Scale bar: 5μm. (b) Optical microscope images of Scenedesmus being sorted on membrane filter. (c) Histogram of $\boldsymbol{T_1 * v_{algae}}$ for Scenedesmus and other microorganisms in lake water.

1.5 DISCUSSION AND CONCLUSION

Leveraging the unique properties of Bessel beam illumination, we present a microfluidic, label-free image-guided cell sorter with an ultra-long depth of focus, resulting in a threefold increase in the number of in-focus cells compared with Gaussian beam systems. Proof-of-concept experiments were demonstrated with high sorting purity using the label-free transmission waveform features as sorting criteria. For the sorting of polystyrene beads, SKNO1 leukemia cells,

and *Scenedesmus* green algae, our results indicate a sorting purity of 97%, 97%, and 98%, respectively. Because of the side lobes inherent to the Bessel beam, a significant amount of computation is required to restore the cell image from the measured temporal signal, and this computation time can limit the throughput. By approximating the zero-order Bessel function by a series of delta functions at its maxima and minima, we have developed an effective mathematical algorithm to restore the cell image from the waveform. The restored images have shown sufficient quality to allow users to visualize the object that is being analyzed and sorted. More importantly, we have demonstrated the method of using the waveform features as gating criteria to sort cells with superior sorting purity, utilizing the close relations between the waveform features and the image features. The successful demonstration of this approach eliminates the need for real-time image reconstruction, greatly reducing the computation resource and time delay. The ability to restore the cell images from the waveform in an off-line process facilitates the human-machine interface, enhancing the operability and user-friendliness of the system.

The current Bessel beam-based flow cytometer/ cell sorting system can be improved with further development. First, Bessel beam illumination requires additional matrix computation while restoring the cell image. In the current system, the image features are extracted directly from the temporal waveform without reconstructing the 2D cell images, which saves a significant amount of computation power. The system refreshes the cell images for data visualization purpose with a processing time of ~3ms under current FPGA processor (Xilinx Kintex-7 XC7K410T). The processing time and system throughput can be further improved by simply using more powerful FPGA. Second, by putting a 500μm x 15μm slit at the image plane, the sidelobes of the Bessel-Gaussian beam along the flow direction are blocked and only the sidelobes along the scanning direction can pass the slit. This configuration simplifies the deconvolution into single dimension.

Our "T-matrix" deconvolution algorithm only needs to do a matrix multiplication in the time domain, which reduces the computation overhead compared to 2D Fourier transform. However, the efficiency of image reconstruction algorithm can be further optimized by leveraging dimensionality reduction algorithms such as compressed sensing techniques to reduce the matrix computation workload.

1.6 SUPPLEMENTARY MATERIAL

This section provides supplementary information in the following areas: detailed algorithms for image reconstruction and protocols for sample preparation.

1.6.1 Image reconstruction algorithm

The electric field of the Bessel-Gaussian beam is given by:

$$\boldsymbol{E_{BG}(r,x)\sim E_0 J_0(k_r r)\frac{w_0}{w(x)} e^{-\frac{r^2}{w_0^2}}\cdot e^{-ik_x x}e^{-i\emptyset}} \qquad \text{(S1)}$$

where $\boldsymbol{r=\sqrt{y^2+z^2}}$ is the distance from the center of the Bessel Gaussian beam. $\boldsymbol{E_0}$ is a field amplitude constant. $\boldsymbol{k_r}$ is the wavevector in the transverse plane and $\boldsymbol{{k_r}^2+{k_x}^2={k}^2}$. $\boldsymbol{w_0}$ is the waist width of Gaussian amplitude. $\emptyset=\boldsymbol{tan^{-1}\frac{x}{x_0}}$. $\boldsymbol{x_0}$ is Rayleigh length of the Gaussian beam.

We use $\boldsymbol{n(x,y,z)}$ to denote the cell or bead index profile $\boldsymbol{n(x,y,z)=n_o+\Delta n(x,y,z)}$. We assume $\boldsymbol{n_o}$ is the index of water and $\boldsymbol{\Delta n>0}$ since the index of cells and beads is greater than the index of water. Assume cell or bead thickness is within $\boldsymbol{x_c}$. For the 2D imaging system, we cannot resolve index change along the beam propagation direction, so we make the following approximation:

$$\boldsymbol{\int_0^{x_c}\Delta n(x,y,z)dx=\Delta\bar{n}(y,z)x_c} \qquad \text{(S2)}$$

Adding a slit in parallel with the laser scanning (y-) direction on the image plane and assuming the slit is narrow enough to be approximated by a 1-D delta function in its transmission characteristic, the transmitted field focused by a lens and after the slit can be approximated by (S3).

$$\boldsymbol{E_t(y',z')} = \boldsymbol{E_0'} e^{-ik_o x} e^{-i\emptyset} \frac{w_0}{w(x)} \int_y \int_z \boldsymbol{\delta(z-}$$

$$\boldsymbol{z'}) \left(\frac{2\sqrt{n_o(n_o+\Delta\bar{n}(y,z))}}{2n_o+\Delta\bar{n}(y,z)}\right) \boldsymbol{J_0}\left[k_r\sqrt{(y'-y)^2+(z'-z)^2}\right] e^{-\frac{(y'-y)^2+(z'-z)^2}{w_0^2}} e^{-ik_o\Delta\bar{n}(y,z)x_c} \boldsymbol{dydz} \qquad \text{(S3)}$$

The term $\left(\frac{2\sqrt{n_o(n_o+\Delta\bar{n}(y,z))}}{2n_o+\Delta\bar{n}(y,z)}\right)$ in Eq. (S3) is the approximate transmission coefficient assuming there is no absorption. Here $(\boldsymbol{y},\boldsymbol{z})$ refers to the transverse coordinate in the object plane, and $(\boldsymbol{y'},\boldsymbol{z'})$ refers to the transverse coordinate in the image (detection) plane. For simplicity, we have transformed the actual position $(\boldsymbol{Y'},\boldsymbol{Z'})$ in the image plane into $(\boldsymbol{y'},\boldsymbol{z'})$ by defining $\boldsymbol{y'} = \frac{\boldsymbol{Y'}}{\boldsymbol{M}}$ and $\boldsymbol{z'} = \frac{\boldsymbol{Z'}}{\boldsymbol{M}}$ with M being the magnification of the detection optics.

Also note that $(\boldsymbol{y'},\boldsymbol{z'})$ is related to time by the following relations:

$$\boldsymbol{y'} = \frac{\boldsymbol{FOV_y}}{\boldsymbol{T}}\,\boldsymbol{t} \qquad \text{(S4-a)}$$

$$\boldsymbol{z'} = \boldsymbol{v_{cell}t} \qquad \text{(S4-b)}$$

From the relations in (S4), we can relate a signal in time domain to the space domain, thus reconstructing the image from a temporal waveform.

To analyze the detected cell transmission signal behind the slit when the center of the scanning Bessel Gaussian beam is at a given position in the flow ($\boldsymbol{z'}$-) direction, we can represent the transmitted field in (S5) under a given position $\boldsymbol{z'}$.

$$\boldsymbol{E_t(y')|_{z'} \propto \int_y \left(\frac{2\sqrt{n_o(n_o+\Delta\bar{n}(y)|_{z'}}}{2n_o+\Delta\bar{n}(y)|_{z'}}\right) J_0\left[k_r\sqrt{(y'-y)^2}\right] e^{-\frac{(y'-y)^2}{w_0^2}} e^{-ik_o\Delta\bar{n}(y)|_{z'}x_c} dy} \quad \text{(S5)}$$

Equation (S5) shows that $\boldsymbol{E_t(y')|_{z'}}$ is the convolution of the index function $\boldsymbol{\left(\frac{2\sqrt{n_o(n_o+\Delta\bar{n}(y)|_{z'}}}{2n_o+\Delta\bar{n}(y)|_{z'}}\right) e^{-ik_o\Delta\bar{n}(y)|_{z'}x_c}}$ and the Bessel Gaussian function $\boldsymbol{J_0[k_r y]e^{-\frac{y^2}{w_0^2}}}$ along the scanning (y-) direction. To save computational power for image reconstruction, we approximate the Bessel function $\boldsymbol{J_0[k_r y]}$ by a series of delta functions at its maxima and minima (Fig. S1):

$$\boldsymbol{J_o(u) \sim \sum_m c_{max,m}\delta(u-u_{max,m}) + \sum_n c_{min,n}\delta(u-u_{min,n})} \quad \text{(S6)}$$

$\boldsymbol{u_{max,m}}$: positions of *mth* maximum of $\boldsymbol{J_o(u)}$. $\boldsymbol{J_o(u_{max,m}) > 0;\ m = 0, \pm1, \pm2, \pm3, \cdots}$

$\boldsymbol{u_{min,n}}$: positions of *nth* minimum of $\boldsymbol{J_o(u)}$. $\boldsymbol{J_o(u_{min,n}) < 0;\ n = \pm1, \pm2, \pm3, \cdots}$

The coefficients for each delta function are defined as

$$\boldsymbol{c_{max,m} = J_0(u_{max,m}) \quad m = 0, \pm1, \pm2, \pm3, \cdots}$$

$$\boldsymbol{c_{min,n} = J_0(u_{min,n}) \quad n = \pm1, \pm2, \pm3, \cdots} \quad \text{(S7)}$$

Substituting (S6) and (S7) into (S5) and dropping the parameter $\boldsymbol{z'}$ for simplicity, we obtain the following approximate expression of the transmitted E-field behind the slit,

$$\boldsymbol{E_t(y')|_{z'} \sim \left[\sum_m C_{max,m} exp\left[-\frac{u_{max,m}^2}{(k_r w_o)^2}\right]\left(\frac{2\sqrt{n_o(n_o+\Delta\bar{n}\left(y'-\frac{u_{max,m}}{k_r}\right)|_{z'}}}{2n_o+\Delta\bar{n}\left(y'-\frac{u_{max,m}}{k_r}\right)|_{z'}}\right) e^{-ik_o\Delta\bar{n}\left(y'-\frac{u_{max,m}}{k_r}\right)|_{z'}x_c}\right] -}$$

$$\boldsymbol{\left[\sum_n C_{min,n} exp\left[-\frac{u_{min,n}^2}{(k_r w_o)^2}\right]\left(\frac{2\sqrt{n_o(n_o+\Delta\bar{n}\left(y'-\frac{u_{min,n}}{k_r}\right)|_{z'}}}{2n_o+\Delta\bar{n}\left(y'-\frac{u_{min,n}}{k_r}\right)|_{z'}}\right) e^{-ik_o\Delta\bar{n}\left(y'-\frac{u_{min,n}}{k_r}\right)|_{z'}x_c}\right]} \quad \text{(S8)}$$

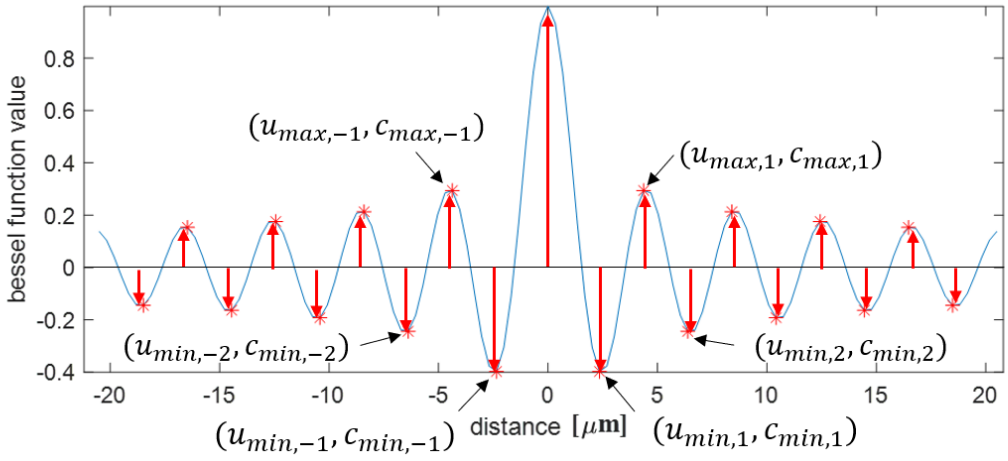

Figure S1.1. Approximate Bessel function by a series of delta functions at the maxima and minima. $\boldsymbol{u_{max,m}}$ and $\boldsymbol{u_{min,n}}$ are positions of $\boldsymbol{mth}$ maximum and $\boldsymbol{nth}$ minimum of $\boldsymbol{J_o(u)}$. $\boldsymbol{c_{max,m} = J_0(u_{max,m})}$, $\boldsymbol{c_{min,n} = J_0(u_{min,n})}$.

Representing $\boldsymbol{E_t(y')} \sim \boldsymbol{A - B}$ in brief form, we can write the transmitted power through the slit as

$$\boldsymbol{J_t(y')|_{z'} \propto E_t^*(y')|_{z'} E_t(y')|_{z'} \propto AA^* + BB^* - AB^* - BA^*} \qquad \text{(S9)}$$

Next we analyze each term in (S9):

$$\boldsymbol{AA^*(y') \sim \left[\sum_{m,m'} C_{max,m} C_{max,m'} exp\left[-\frac{u_{max,m}^2 + u_{max,m'}^2}{(k_r w_o)^2}\right]\left(\frac{2\sqrt{n_o(n_o+\Delta\bar{n}\left(y'-\frac{u_{max,m}}{k_r}\right)|_{z'}}}{2n_o+\Delta\bar{n}\left(y'-\frac{u_{max,m}}{k_r}\right)|_{z'}}\right)\times\right.}$$

$$\boldsymbol{\left.\left(\frac{2\sqrt{n_o(n_o+\Delta\bar{n}\left(y'-\frac{u_{max,m'}}{k_r}\right)|_{z'}}}{2n_o+\Delta\bar{n}\left(y'-\frac{u_{max,m'}}{k_r}\right)|_{z'}}\right)\right] e^{-ik_o[\Delta\bar{n}\left(y'-\frac{u_{max,m}}{k_r}\right)-\Delta\bar{n}\left(y'-\frac{u_{max,m'}}{k_r}\right)]x_c}} \qquad \text{(S10)}$$

It can be shown that the imaginary part of $\boldsymbol{AA^*}$ is zero. Thus

$$AA^*(y') \sim \left[\sum_{m,m'} C_{max,m} C_{max,m'} exp\left[-\frac{u_{max,m}^2+u_{max,m'}^2}{(k_r w_o)^2}\right]\left(\frac{2\sqrt{n_o(n_o+\Delta\bar{n}\left(y'-\frac{u_{max,m}}{k_r}\right)|_{z'}}}{2n_o+\Delta\bar{n}\left(y'-\frac{u_{max,m}}{k_r}\right)|_{z'}}\right)\times\right.$$

$$\left.\left(\frac{2\sqrt{n_o(n_o+\Delta\bar{n}\left(y'-\frac{u_{max,m'}}{k_r}\right)|_{z'}}}{2n_o+\Delta\bar{n}\left(y'-\frac{u_{max,m'}}{k_r}\right)|_{z'}}\right)\right] cos\left[k_o[\Delta\bar{n}\left(y'-\frac{u_{max,m}}{k_r}\right)-\Delta\bar{n}\left(y'-\frac{u_{max,m'}}{k_r}\right)]x_c\right] \quad \text{(S10-A)}$$

For $m \neq m'$, the summation of the phase mismatched terms in (S10-A) leads to cancellation and produces small effects. Keeping the $m = m'$ terms only and having $u_{max,m=0} = 0$ (i.e. the first max for the zero-order Bessel function is at the origin).

$$AA^*(y') \cong \frac{4n_o(n_o+\Delta\bar{n}(y')|_{z'}}{(2n_o+\Delta\bar{n}(y')|_{z'})^2} + \left[\sum_{m\neq 0} C_{max,m}{}^2 exp\left[-\frac{2u_{max,m}^2}{(k_r w_o)^2}\right]\frac{4n_o(n_o+\Delta\bar{n}\left(y'-\frac{u_{max,m}}{k_r}\right)|_{z'}}{\left(2n_o+\Delta\bar{n}\left(y'-\frac{u_{max,m}}{k_r}\right)|_{z'}\right)^2}\right]$$

(S10-B)

Similarly, we have

$$BB^*(y') \sim \left[\sum_{n,n'} C_{min,n} C_{min,n'} exp\left[-\frac{u_{min,n}^2+u_{min,n'}^2}{(k_r w_o)^2}\right]\left(\frac{2\sqrt{n_o(n_o+\Delta\bar{n}\left(y'-\frac{u_{min,n}}{k_r}\right)|_{z'}}}{2n_o+\Delta\bar{n}\left(y'-\frac{u_{min,n}}{k_r}\right)|_{z'}}\right)\times\right.$$

$$\left.\left(\frac{2\sqrt{n_o(n_o+\Delta\bar{n}\left(y'-\frac{u_{min,n'}}{k_r}\right)|_{z'}}}{2n_o+\Delta\bar{n}\left(y'-\frac{u_{min,n'}}{k_r}\right)|_{z'}}\right)\right] e^{-ik_o[\Delta\bar{n}\left(y'-\frac{u_{min,n}}{k_r}\right)-\Delta\bar{n}\left(y'-\frac{u_{min,n'}}{k_r}\right)]x_c} \quad \text{(S11)}$$

$$BB^*(y') \sim \left[\sum_{n,n'} C_{min,n} C_{min,n'} exp\left[-\frac{u_{min,n}^2+u_{min,n'}^2}{(k_r w_o)^2}\right]\left(\frac{2\sqrt{n_o(n_o+\Delta\bar{n}\left(y'-\frac{u_{min,n}}{k_r}\right)|_{z'}}}{2n_o+\Delta\bar{n}\left(y'-\frac{u_{min,n}}{k_r}\right)|_{z'}}\right)\times\right.$$

$$\left.\left(\frac{2\sqrt{n_o(n_o+\Delta\bar{n}\left(y'-\frac{u_{min,n'}}{k_r}\right)|_{z'}}}{2n_o+\Delta\bar{n}\left(y'-\frac{u_{min,n'}}{k_r}\right)|_{z'}}\right)\right] cos\left[k_o[\Delta\bar{n}\left(y'-\frac{u_{min,n}}{k_r}\right)-\Delta\bar{n}\left(y'-\frac{u_{min,n'}}{k_r}\right)]x_c\right] \quad \text{(S11-A)}$$

For the same argument as before, we take only the terms where $n = n'$, then (S11-A) can be represented approximately as

$$\boldsymbol{BB^*(y')} \cong \left[\sum_n \boldsymbol{C_{min,n}}^2 \boldsymbol{exp}\left[-\frac{2u_{min,n}^2}{(k_r w_o)^2}\right]\frac{4n_o(n_o+\Delta\bar{n}\left(y'-\frac{u_{min,n}}{k_r}\right)|_{z'}}{\left(2n_o+\Delta\bar{n}\left(y'-\frac{u_{min,n}}{k_r}\right)|_{z'}\right)^2}\right] \qquad \text{(S11-B)}$$

Similarly,

$$\boldsymbol{AB^*(y')} \sim \left[\sum_{m,n'} \boldsymbol{C_{max,m}}\,\boldsymbol{C_{min,n'}} \boldsymbol{exp}\left[-\frac{u_{max,m}^2+u_{min,n'}^2}{(k_r w_o)^2}\right]\left(\frac{2\sqrt{n_o(n_o+\Delta\bar{n}\left(y'-\frac{u_{max,m}}{k_r}\right)|_{z'}}}{2n_o+\Delta\bar{n}\left(y'-\frac{u_{max,m}}{k_r}\right)|_{z'}}\right)\times\right.$$

$$\left.\left(\frac{2\sqrt{n_o(n_o+\Delta\bar{n}\left(y'-\frac{u_{min,n'}}{k_r}\right)|_{z'}}}{2n_o+\Delta\bar{n}\left(y'-\frac{u_{min,n'}}{k_r}\right)|_{z'}}\right)\right] \qquad \boldsymbol{e}^{-i\boldsymbol{k_o}[\Delta\bar{n}\left(y'-\frac{u_{max,m}}{k_r}\right)-\Delta\bar{n}\left(y'-\frac{u_{min,n'}}{k_r}\right)]\boldsymbol{x}_c} \qquad \text{(S12)}$$

$$\boldsymbol{AB^*(y')} \sim \left[\sum_{m,n'} \boldsymbol{C_{max,m}}\,\boldsymbol{C_{min,n'}} \boldsymbol{exp}\left[-\frac{u_{max,m}^2+u_{min,n'}^2}{(k_r w_o)^2}\right]\left(\frac{2\sqrt{n_o(n_o+\Delta\bar{n}\left(y'-\frac{u_{max,m}}{k_r}\right)|_{z'}}}{2n_o+\Delta\bar{n}\left(y'-\frac{u_{max,m}}{k_r}\right)|_{z'}}\right)\times\right.$$

$$\left.\left(\frac{2\sqrt{n_o(n_o+\Delta\bar{n}\left(y'-\frac{u_{min,n'}}{k_r}\right)|_{z'}}}{2n_o+\Delta\bar{n}\left(y'-\frac{u_{min,n'}}{k_r}\right)|_{z'}}\right)\right] \quad \boldsymbol{cos}\left[\boldsymbol{k_o}[\Delta\bar{\boldsymbol{n}}\left(\boldsymbol{y'}-\frac{\boldsymbol{u_{max,m}}}{\boldsymbol{k_r}}\right)-\Delta\bar{\boldsymbol{n}}\left(\boldsymbol{y'}-\frac{\boldsymbol{u_{min,n'}}}{\boldsymbol{k_r}}\right)]\boldsymbol{x_c}\right] \qquad \text{(S12-A)}$$

By the same argument as above, we have $\boldsymbol{AB^*(y')}\sim\mathbf{0}$, since the $\boldsymbol{cos}$ terms contain random phases.

$$\boldsymbol{BA^*(y')} \sim \left[\sum_{n,m'} \boldsymbol{C_{min,n}}\,\boldsymbol{C_{max,m'}} \boldsymbol{exp}\left[-\frac{u_{min,n}^2+u_{max,m'}^2}{(k_r w_o)^2}\right]\left(\frac{2\sqrt{n_o(n_o+\Delta\bar{n}\left(y'-\frac{u_{min,n}}{k_r}\right)|_{z'}}}{2n_o+\Delta\bar{n}\left(y'-\frac{u_{min,n}}{k_r}\right)|_{z'}}\right)\times\right.$$

$$\left.\left(\frac{2\sqrt{n_o(n_o+\Delta\bar{n}\left(y'-\frac{u_{max,m'}}{k_r}\right)|_{z'}}}{2n_o+\Delta\bar{n}\left(y'-\frac{u_{max,m'}}{k_r}\right)|_{z'}}\right)\right] \qquad \boldsymbol{e}^{-i\boldsymbol{k_o}[\Delta\bar{n}\left(y'-\frac{u_{min,n}}{k_r}\right)-\Delta\bar{n}\left(y'-\frac{u_{max,m'}}{k_r}\right)]\boldsymbol{x}_c} \qquad \text{(S13)}$$

For the same reason above, $\boldsymbol{BA^*(y')}\sim\mathbf{0}$.

Consequently, we have

$$J_t(y',x)\sim\frac{4n_o(n_o+\Delta\bar{n}(y')|_{z'}}{(2n_o+\Delta\bar{n}(y')|_{z'})^2}+\left[\sum_{m\neq0}C_{max,m}{}^2\,exp\left[-\frac{2u_{max,m}^2}{(k_rw_o)^2}\right]\frac{4n_o(n_o+\Delta\bar{n}\left(y'-\frac{u_{max,m}}{k_r}\right)|_{z'}}{\left(2n_o+\Delta\bar{n}\left(y'-\frac{u_{max,m}}{k_r}\right)|_{z'}\right)^2}\right]+$$

$$\left[\sum_nC_{min,n}{}^2\,exp\left[-\frac{2u_{min,n}^2}{(k_rw_o)^2}\right]\frac{4n_o(n_o+\Delta\bar{n}\left(y'-\frac{u_{min,n}}{k_r}\right)|_{z'}}{\left(2n_o+\Delta\bar{n}\left(y'-\frac{u_{min,n}}{k_r}\right)|_{z'}\right)^2}\right] \quad \text{(S14)}$$

Define $f(y,z)=\frac{4n_o(n_o+\Delta\bar{n}(y)}{(2n_o+\Delta\bar{n}(y))^2}|_z$. By solving $f(y,z)$, we can obtain the index profile of the object $\Delta\bar{n}(y,z)$.

According to (S14), we have

$$J_t(y',z')=f(y',z')+\left[\sum_{m\neq0}C_{max,m}{}^2\,exp\left[-\frac{2u_{max,m}^2}{(k_rw_o)^2}\right]f\left(y'-\frac{u_{max,m}}{k_r},z'\right)\right]+$$

$$\left[\sum_nC_{min,n}{}^2\,exp\left[-\frac{2u_{min,n}^2}{(k_rw_o)^2}\right]f\left(y'-\frac{u_{min,n}}{k_r},z'\right)\right]$$

$$=f(y',z')+\left[\sum_{m\neq0}a_{max,m}{}^2\,f\left(y'-\frac{u_{max,m}}{k_r},z'\right)\right]+\left[\sum_na_{min,n}{}^2\,f\left(y'-\frac{u_{min,n}}{k_r},z'\right)\right] \quad \text{(S15)}$$

$$a_{max,m}{}^2=C_{max,m}{}^2e^{-\frac{2u_{max,m}{}^2}{k_r^2w_o^2}} \qquad m=\pm1,\pm2,\pm3,\cdots \qquad \text{(S16-a)}$$

$$a_{min,m}{}^2=C_{min,n}{}^2e^{-\frac{2u_{min,n}{}^2}{k_r^2w_o^2}} \qquad n=\pm1,\pm2,\pm3,\cdots \qquad \text{(S16-b)}$$

Next we discuss how to determine the limits of m and n in (S15). We assume the scanning range of the laser beam is from $-L_y/2$ to $L_y/2$, and the laser beam spot covers a range from $-W_y/2$ to $+W_y/2$ due to the side lobes of the Bessel Gaussian beam. Assume a scanning rate of 200kHz and a sampling rate of 25 MS/s, we have 125 sampling points for each scan corresponding to the beam center position.

We assume the width of the side lobes of a Bessel Gaussian beam is W_y. The transmitted light intensity becomes nonzero when $-\frac{W_y}{2}<y'-y<\frac{W_y}{2}$. Then

$$-\frac{L_y}{2}-\frac{W_y}{2}<y<\frac{L_y}{2}+\frac{W_y}{2} \qquad \text{(S17)}$$

Equation (S17) defines the integration range for (S15). In other words, we need to integrate at least over this range defined in (S17) to restore the object image from the measured data in each scan.

The dimension of the T-matrix we will discuss next would be a $\left\{125\left[1+\frac{W_y}{L_y}\right]+1\right\}\times\left\{125\left[1+\frac{W_y}{L_y}\right]+1\right\}$ matrix. If we choose $\frac{W_y}{L_y}=1$, then the T-matrix is a 251x251 matrix.

We write $J_t(y',z')$ into a column matrix with 125 non-zero elements defined by the "width" of the Bessel Gaussian beam. Arbitrarily, we choose these 125 nontrivial points in an index range from -2 to 122, as shown in (S18). Outside this range, we define the "padding values" $B=J_t(y'_0,z')$ and $B'=J_t(y'_{120},z')$.

$$\begin{bmatrix} B \\ \cdots \\ B \\ J_t(y'_{-2},z') \\ J_t(y'_{-1},z') \\ J_t(y'_0,z') \\ J_t(y'_1,z') \\ J_t(y'_2,z') \\ \vdots \\ J_t(y'_{120},z') \\ J_t(y'_{121},z') \\ J_t(y'_{122},z') \\ B' \\ B' \\ \cdots \\ B' \end{bmatrix}_{251x1} = [T]_{251x251} \begin{bmatrix} f(y'_{-65},z') \\ \cdots \\ f(y'_{-3},z') \\ f(y'_{-2},z') \\ f(y'_{-1},z') \\ f(y'_0,z') \\ f(y'_1,z') \\ f(y'_2,z') \\ \vdots \\ f(y'_{120},z') \\ f(y'_{121},z') \\ f(y'_{122},z') \\ f(y'_{123},z') \\ f(y'_{124},z') \\ \cdots \\ f(y'_{185},z') \end{bmatrix}_{251x1} \qquad \text{(S18)}$$

$\boldsymbol{J_t(y'_0, z')}, \cdots, \boldsymbol{J_t(y'_{120}, z')}$ and $\boldsymbol{f(y'_0, z')}, \cdots, \boldsymbol{f(y'_{120}, z')}$ are within the "chosen" field of view. $\boldsymbol{J_t(y'_{-2}, z')}, \boldsymbol{J_t(y'_{-1}, z')}, \boldsymbol{J_t(y'_{121}, z')}, \boldsymbol{J_t(y'_{122}, z')}$ are measured signal within the laser scanning range. The reason why we have nontrivial $\boldsymbol{f(y'_{-65}, z')}, \cdots, \boldsymbol{f(y'_{-3}, z')}$ and $\boldsymbol{f(y'_{123}, z')}, \cdots, \boldsymbol{f(y'_{185}, z')}$ is because the side lobes of the Bessel Gaussian beam can illuminate objects outside the field of view.

Calculating the inverse of the T-matrix, we can solve $\boldsymbol{f(y', z')}$

$$\begin{bmatrix} \boldsymbol{f(y'_{-65}, z')} \\ \cdots \\ \boldsymbol{f(y'_{-3}, z')} \\ \boldsymbol{f(y'_{-2}, z')} \\ \boldsymbol{f(y'_{-1}, z')} \\ \boldsymbol{f(y'_0, z')} \\ \boldsymbol{f(y'_1, z')} \\ \boldsymbol{f(y'_2, z')} \\ \vdots \\ \boldsymbol{f(y'_{120}, z')} \\ \boldsymbol{f(y'_{121}, z')} \\ \boldsymbol{f(y'_{122}, z')} \\ \boldsymbol{f(y'_{123}, z')} \\ \boldsymbol{f(y'_{124}, z')} \\ \cdots \\ \boldsymbol{f(y'_{185}, z')} \end{bmatrix}_{\boldsymbol{251x1}} = [\boldsymbol{T}]^{-1}{}_{\boldsymbol{251x251}} \begin{bmatrix} \boldsymbol{B} \\ \cdots \\ \boldsymbol{B} \\ \boldsymbol{J_t(y'_{-2}, z')} \\ \boldsymbol{J_t(y'_{-1}, z')} \\ \boldsymbol{J_t(y'_0, z')} \\ \boldsymbol{J_t(y'_1, z')} \\ \boldsymbol{J_t(y'_2, z')} \\ \vdots \\ \boldsymbol{J_t(y'_{120}, z')} \\ \boldsymbol{J_t(y'_{121}, z')} \\ \boldsymbol{J_t(y'_{122}, z')} \\ \boldsymbol{B'} \\ \boldsymbol{B'} \\ \cdots \\ \boldsymbol{B'} \end{bmatrix}_{\boldsymbol{251x1}} \quad \text{(S19)}$$

The elements of the T-matrix are defined as follow:

$\boldsymbol{T_{ij} = 1.} \quad \boldsymbol{if} \quad \boldsymbol{i = j,} \quad \boldsymbol{-65 \le i, j \le 185}$

$\boldsymbol{T_{ij} = C_l{}^2 exp\left[-\frac{2u_l^2}{(k_r w_o)^2}\right] \equiv a_l^2}$ where $\boldsymbol{u_l}$ is the $\boldsymbol{lth\ min}$ or $\boldsymbol{max}$ for $\boldsymbol{J_0(u)}$ if $\boldsymbol{y'_i - \frac{u_l}{k_r} = y'_j}$

$\boldsymbol{T_{ij} = 0.} \quad \boldsymbol{otherwise}$ (S20)

Equations (S19) and (S20) describe how we reconstruct the transmission images for cells or beads from the PMT signal.

1.6.2 Sample preparation

Culture of AML cells:

SKNO-1 leukemia cells were seeded at a concentration of ~$0.5x10^6$ cells/ml and incubated at 37ºC, 5% CO_2 in culture medium (90% RPMI-1640+10% FBS+1%PS). Cells were split by a ratio of 1:2 to 1:3 every 2-3 days when confluency was reached (~$2.5x10^6$ cells/ml). Prior to the sorting experiment, cells were collected from medium via centrifugation, then resuspended in PBS.

Preparation of normal white blood cells:

Whole blood from healthy donors was obtained from San Diego Blood Bank (3636 Gateway Center Ave Suite 100, San Diego, CA, 92102). The following steps were performed to lyse the red blood cells and to collect the white blood cells from whole blood:

1. Mix 1ml of whole blood and 10ml of 1X Lysis Buffer (Invitrogen, 00-4333-57) in a 15mL conical tube.
2. Incubate for 12mins at room temperature.
3. Centrifuge at 400g for 6 mins.
4. Pipette out supernatant, making sure to leave no red layer in the tube.
5. Add 5ml of 1X Lysis buffer and wash at 400g.
6. Pipette out supernatant, making sure to leave no red layer in the tube.
7. Dilute sample with PBS to desired concentration. The sample should contain concentrated WBCs.

Wright-Giemsa staining of white blood cells/leukemia cells on membrane filter

1. Place cells on membrane filter and let dry.

2. Fix cells by placing them in pure Methanol for 5 minutes.

3. Place the membrane filter in a staining tray and immerse it in Working Wright Giemsa Solution for 5 minutes.

4. Rinse the cells in deionized/distilled water.

5. Flood with Phosphate Buffer Solution, pH 6.8 until no stain runs off. Allow the membrane filter to remain in pH 6.8 PBS for an additional 1 minute.

6. Dip the membrane filter in distilled water and air dry at room temperature.

7. Dip the membrane filter in Xylene or Xylene Substitute several times.

9. Put the membrane filter on a glass slide and mount it in synthetic resin.

1.7 REFERENCES

[1] S. L. Goldman, M. MacKay, E. Afshinnekoo, A. M. Melnick, S. Wu, and C. E. Mason, "The impact of heterogeneity on single-cell sequencing," Front. Genet. 10, 8 (2019).

[2] N. Hasle, Anthony Cooke, Sanjay Srivatsan, Heather Huang, Jason J Stephany, Zachary Krieger, Dana Jackson, Weiliang Tang, Sriram Pendyala, Raymond J Monnat Jr., Cole Trapnell, Emily M Hatch, and Douglas M Fowler. "High-throughput, microscope-based sorting to dissect cellular heterogeneity," Mol. Syst. Biol. 16, e9442 (2020).

[3] A. Hochstetter, Rohan Vernekar, Robert H. Austin, Holger Becker, Jason P. Beech, Dmitry A. Fedosov, Gerhard Gompper, Sung-Cheol Kim, Joshua T. Smith, Gustavo Stolovitzky, Jonas O. Tegenfeldt, Benjamin H. Wunsch, Kerwin K. Zeming, Timm Krüger*, and David W. Inglis. "Deterministic lateral displacement: Challenges and perspectives," ACS Nano 14(9), 10784–10795 (2020).

[4] M. K. Brakke, "Density gradient centrifugation: A new separation technique," J. Am. Chem. Soc. 73(4), 1847–1848 (1951).

[5] W. A. Bonner, H. R. Hulett, R. G. Sweet, and L. A. Herzenberg, "Fluorescence activated cell sorting," Rev. Sci. Instrum. 43, 404 (1972).

[6] G. Welzel, D. Seitz, and S. Schuster, "Magnetic-activated cell sorting (MACS) can be used as a large-scale method for establishing zebrafish neuronal cell cultures," Sci. Rep. 5, 7959 (2015).

[7] A. Gross, J. Schoendube, S. Zimmermann, M. Steeb, R. Zengerle, and P. Koltay, "Technologies for single-cell isolation," Int. J. Mol. Sci. 16, 16897–16919 (2015).

[8] P. Hu, W. Zhang, H. Xin, and G. Deng, "Single cell isolation and analysis," Front. Cell Dev. Biol. 4, 116 (2016).

[9] Y. Gu, A. C. Zhang, Y. Han, J. Li, C. Chen, and Y. H. Lo, "Machine learning based real-time image-guided cell sorting and classification," Cytometry 95, 499–509 (2019).

[10] S. Li, Xiaoyun Ding, Feng Guo, Yuchao Chen, Michael Ian Lapsley, Sz-Chin Steven Lin, Lin Wang, J. Philip McCoy, Craig E. Cameron, and Tony Jun Huang. "An on-chip, multichannel droplet sorter using standing surface acoustic waves," Anal. Chem. 85(11), 5468–5474 (2013).

[11] Y. Pan, X. Du, F. Zhao, and B. Xu, "Magnetic nanoparticles for the manipulation of proteins and cells," Chem. Soc. Rev. 41(7), 2912–2942 (2012).

[12] B. H. Lapizco-Encinas, B. A. Simmons, E. B. Cummings, and Y. Fintschenko, "Insulator-based dielectrophoresis for the selective concentration and separation of live bacteria in water," Electrophoresis 25(10-11), 1695–1704 (2004).

[13] N. Nitta, T. Sugimura, A. Isozaki, H. Mikami, K. Hiraki, S. Sakuma, T. Iino, F. Arai, T. Endo, Y. Fujiwaki, H. Fukuzawa, M. Hase, T. Hayakawa, K. Hiramatsu, Y. Hoshino, M. Inaba, T. Ito, H. Karakawa, Y. Kasai, K. Koizumi, S.W. Lee, C. Lei, M. Li, T. Maeno, S. Matsusaka, D. Murakami, A. Nakagawa, Y. Oguchi, M. Oikawa, T. Ota, K. Shiba, H. Shintaku, Y. Shirasaki, K. Suga, Y. Suzuki, N. Suzuki, Y. Tanaka, H. Tezuka, C. Toyokawa, Y. Yalikun, M. Yamada, M. Yamagishi, T. Yamano, A. Yasumoto, Y. Yatomi, M. Yazawa, D. Di Carlo, Y. Hosokawa, S. Uemura, Y. Ozeki, and K. Goda. "Intelligent image-activated cell sorting," Cell 175, 266–276 (2018).

[14] M. Sesen and G. Whyte, "Image-based single cell sorting automation in droplet microfluidics," Sci. Rep. 10, 8736 (2020).

[15] Chen X, Gu Y, Chen J, Lee C-H, Gagne I, Tang R, Waller L, Zhang Z, Zhang AC, Han Y, Wang W, Lian I, Cho SH, Lo Y-H. "Image-guided cell sorting using fast scanning lasers," APL Photonics 5(4), 040801 (2020).

[16] C. H. Chen, S. H. Cho, F. Tsai, A. Erten, and Y.-H. Lo, "Microfluidic cell sorter with integrated piezoelectric actuator," Biomed. Microdevices 11(6), 1223–1231 (2009).

[17] L. Gao, L. Shao, B.-C. Chen, and E. Betzig, "3D live fluorescence imaging of cellular dynamics using Bessel beam plane illumination microscopy," Nat. Protoc. 9, 1083–1101 (2014).

[18] M. C. Müllenbroich, Lapo Turrini , Ludovico Silvestri, Tommaso Alterini, Ali Gheisari, Natascia Tiso, Francesco Vanzi, Leonardo Sacconi, and Francesco S Pavone. "Bessel beam

illumination reduces random and systematic errors in quantitative functional studies using light-sheet microscopy," Front. Cell. Neurosci. 12, 315 (2018).

[19] V. Grillo, Jérémie Harris, Gian Carlo Gazzadi, Roberto Balboni, Erfan Mafakheri, Mark R. Dennis, Stefano Frabboni, Robert W. Boyd, and Ebrahim Karimi, "Generation and application of Bessel beams in electron microscopy," Ultramicroscopy 166, 48–60 (2016).

[20] D. S. Simon, A Guided Tour of Light Beams: From Lasers to Optical Knots (IOP Science, 2016).

[21] R. M. Herman and T. A. Wiggins, "Production and uses of diffractionless beams," J. Opt. Soc. Am. A 8(6), 932–942 (1991).

[22] C. H. Chen, S. H. Cho, H.-I. Chiang, F. Tsai, K. Zhang, and Y.-H. Lo, "Specific sorting of single bacterial cells with microfabricated fluorescence-activated cell sorting and tyramide signal amplification fluorescence in situ hybridization," Anal. Chem. 83(19), 7269–7275 (2011).

[23] Cancer stat facts: Leukemia—Acute myeloid leukemia (AML), NIH, available at https://seer.cancer.gov/statfacts/html/amyl.html.

[24] Cancer facts and figures 2020, American Cancer Society, 2020, available at https://www.cancer.org/content/dam/cancer-org/research/cancer-facts-and-statistics/annual-cancer-facts-and-figures/2020/cancer-facts-and-figures-2020. pdf.

[25] H. Döhner, D. J. Weisdorf, and C. D. Bloomfield, "Acute myeloid leukemia," N. Engl. J. Med. 373, 1136–1152 (2015).

[26] Aishwarye Sharma, Shruti Sharma, Kuldeep Sharma, Siva P. K. Chetri, Amit Vashishtha, Pushpa Singh, Ravindra Kumar, Brijesh Rathi, and Veena Agrawal. "Algae as crucial organisms in advancing nanotechnology: A systematic review," J. Appl. Phycol. 28, 1759–1774 (2016).

[27] A. Ahmadi, S. Z. Moghadamtousi, S. Abubakar, and K. Zandi, "Antiviral potential of algae polysaccharides isolated from marine sources: A review," BioMed Res. Int. 2015, 825203.

[28] N. Abdel-Raouf, A. A. Al-Homaidan, and I. B. M. Ibraheem, "Microalgae and wastewater treatment," Saudi J. Biol. Sci. 19(3), 257–275 (2012).

[29] Liliana Rodolfi, Graziella Chini Zittelli, Niccolò Bassi, Giulia Padovani, Natascia Biondi, Gimena Bonini, and Mario R Tredici. "Microalgae for oil: Strain selection, induction of lipid synthesis and outdoor mass cultivation in a low-cost photobioreactor," Biotechnol. Bioeng. 102(1), 100–112 (2009).

[30] F. B. Metting, Jr., "Biodiversity and application of microalgae," J. Ind. Microbiol. 17, 477–489 (1996).

[31] A. Darzins, P. Pienkoes, and L. Edye, Current status and potential for algal biofuels production, National Renewable Energy Laboratory (NREL), T39–T2, available at http://task39.sites.olt.ubc.ca/files/2013/05/IEA-Task-39-Current-Statusand-Potential-of-Algal-biofuels0.pdf.

[32] R. J. Best, J. J. Lyczakowski, S. Abalde-Cela, Z. Yu, C. Abell, and A. G. Smith, "Label-free analysis and sorting of microalgae and cyanobacteria in microdroplets by intrinsic chlorophyll fluorescence for the identification of fast growing strains," Anal. Chem. 88(21), 10445–10451 (2016).

[33] R. S. Gour, A. Chawla, H. Singh, R. S. Chauhan, and A. Kant, "Characterization and screening of native Scenedesmus sp. isolates suitable for biofuel feedstock," PLoS One 11, e0155321 (2016).

Acknowledgements

Chapter 1, in full, is a near-verbatim reprint of the material as it appears in APL Photonics 2021. Chen X*, Waller L*, Chen J, Tang R, Zhang Z, Gagne I, Gutierrez B, Cho SH, Tseng C-Y, Lian I, Lo Y-H., AIP Publishing, 2021. The dissertation author was the co-primary investigator and author of this paper.

CHAPTER 2: HIGH SENSITIVITY, RAPID DETECTION OF VIRUS IN HIGH TRAFFIC ENVIRONMENTS

2.1 ABSTRACT

The global pandemic caused by the SARS-CoV-2 virus has underscored the need for rapid, simple, scalable, and high-throughput multiplex diagnostics in non-laboratory settings. Here we demonstrate a multiplex reverse-transcription loop-mediated isothermal amplification (RT-LAMP) coupled with a gold nanoparticle-based lateral flow immunoassay (LFIA) capable of detecting up to three unique viral gene targets in 15 minutes. RT-LAMP primers associated with three separate gene targets from the SARS-CoV-2 virus (Orf1ab, Envelope, and Nucleocapsid) were added in a one-pot mix. A colorimetric change from red to yellow occurs in the presence of a positive sample. Positive samples are run through a LFIA to achieve specificity on a multiplex three- testline paper assay. Positive results are indicated by a characteristic crimson line. The device is almost fully automated and is deployable in any community setting with a power source.

2.2 INTRODUCTION

In late December 2019, a major outbreak of a novel coronavirus of zoonotic origin broke out in Wuhan, Hubei province, China [34]. The rampant global spread of COVID-19 has shocked and forever changed the world, with 271,376,643 confirmed cases and 5,324,969 deaths globally as of 16 December 2021 [35].

Socioeconomic expansion and increased travel in this modern age have become associated with a rise in the emergence of novel viruses, with notable examples including the 2003 severe acute respiratory syndrome coronavirus (SARS) outbreak, the 2009 swine flu pandemic, the 2012 Middle East respiratory syndrome coronavirus outbreak (MERS), the 2013-2016 Ebola epidemic, and the 2015 Zika virus epidemic [36]. With modern transportation capable of moving a person

with a contagious illness to nearly any location in the world in under 24 h, the potential for highly contagious new outbreaks poses an incredible global health risk.

Novel respiratory pathogens such as SARS-CoV-2 have an established precedent of elevated transmissibility via high-traffic hubs of national or international travel such as airports, train stations, and cruise terminals [37][38]. Fueled by its high reproduction number, asymptomatic carriers, superspreading events, increasing socio economic globalization, and an immunologically naive population, COVID-19 has wreaked havoc across the world [39].

More than ever before, rapid diagnostic tests have become a fundamental component of outbreak mitigation, with crucial roles ranging from initial detection and quarantining procedures to population-level monitoring[40]. Although a number of diagnostic technologies exist, RT-qPCR is commonly considered the gold standard and is consequently the most widely adopted diagnostic method in test centers and hospitals. The technique consists of three steps: collection of nasopharyngeal or oropharyngeal swabs from patients; total RNA extraction or isolation; and specific detection of target viral genome sequences via RT-qPCR. In RT-qPCR, the viral RNA is transcribed into cDNA by reverse transcriptase. The cDNA is the template for qPCR. Amplification products are quantified by the addition of a fluorescent label during replication. As the reaction proceeds, the fluorescence signal is directly proportional to DNA concentration and the linear correlation can be used to determine the amount of template at the start of the reaction [41]. The inclusion of reverse transcription for the diagnosis of RNA viruses provides the necessary sensitivity and specificity for widespread use in a laboratory setting.

However, RT-qPCR is not sufficient for use in many high-traffic community settings for a number of reasons. This technique includes several sample handling steps; therefore, the sample-to-result procedure in a clinical diagnostic laboratory can take about 3–24 h or more, depending

on the test center [42]. RT-qPCR also requires specialized lab equipment such as thermocyclers and fluorometers, and skilled operational personnel. These requirements are not easily implementable in community settings without significant equipment, training, and staffing costs, especially in underdeveloped and remote areas.

Isothermal amplification techniques are a popular solution for bringing diagnostic testing to non-laboratory environments due to its impressive sensitivity and ability to be performed with minimal resources [43]. While a large number of isothermal amplification methods exist, loop-mediated isothermal amplification (LAMP) is amongst the most popular. LAMP enables nucleic acid amplification in 10–40 min using 4 to 6 primers and a polymerase with chain displacing ability at a constant temperature of around 65°C. In the case of reverse transcription LAMP (RT-LAMP), the process is initiated by reverse transcription from the backward inner primer (BIP) by binding onto the 3' end. Concurrently, a new cDNA strand is created by binding of the B3 primer to the template aided by a strand displacing DNA polymerase. Loops at the 3' end are created as the single stranded copy binds to itself. Then, the forward inner primer (FIP) binds to the 5' end and aided by DNA polymerase, synthesizes a complementary strand. The F3 primer with DNA polymerase binds to the complementary strand and generates a new double stranded DNA while displacing the previous single strand. The amplification products are an amalgamation of target RNA and primers. The single stranded DNA forms dumbbell-like structures as the ends fold and bind to themselves. Exponential amplification of the dumbbell-like structure is then initiated. The addition of loop primers greatly speeds up the reaction [44] [45] [46].

The detection of target amplification products in RT-LAMP assays is frequently colorimetric. One common method is to use a pH indicator (e.g., phenol red) and execute the reaction in a weakly buffered environment. The lowering of the pH as the reaction proceeds results

in a visible color change from red to yellow [42]. With pre-mixed reverse transcription and colorimetric LAMP reagents widely available (e.g., WarmStart Colorimetric LAMP 2X Master Mix, New England Biolabs, MA, United States), RT-LAMP is an appealing technique for deployment in high-traffic community settings. The colorimetric detection can be accelerated by adding chemicals (e.g., guanidine hydrochloride) and primers associated with additional target gene segments from the same virus. In the same spirit, primers for multiple diseases can be multiplexed to yield a single positive or negative in a one-pot mixture.

To achieve specificity of specific disease targets within this one-pot mixture, RT-LAMP can be coupled with a lateral flow immunoassay (LFIA). LFIAs offer an enticing solution to point-of-care diagnostics due to their low cost, high specificity, and simplicity of use [47][48] [49][50]. Lateral flow assays are a paper-based platform that allows a sample to be placed on a test device and results to be displayed in about 10 min. The device usually consists of a sample pad, a conjugate pad, a nitrocellulose membrane, and an absorbent pad. The sample is mixed with running buffers and placed onto the sample pad. The conjugate pad usually contains reporter particles such as functionalized gold nanoparticles. If a positive sample is present, the reporter particles will bind to the analyte. Striped lines of antibody on the nitrocellulose membrane capture the analyte, and a control line captures extraneous reporter particles to validate the test. Positive results for an analyte will appear as a red line.

Here we present a high-throughput, rapid diagnostic machine that can be employed in almost any high-traffic public setting for the rapid detection of up to three gene targets, and the method can be readily extended to more targets from different organisms. The system uses RT-LAMP to isothermally amplify target sequences and provide a rapid yes or no diagnostic response based on the colorimetric change from red to yellow. Then, the RT-LAMP product is run through

a lateral flow immunoassay to provide specificity. Here we use three gene targets of SARS-CoV-2 (Orf1ab, N, and E); however, the diagnostic ability can be more broadly applied by substituting the appropriate primers for other viral gene targets.

2.3 MATERIALS AND METHODS

2.3.1 Automated System Architecture

A customized machine is utilized to automate all steps beyond the loading of patient samples. The machine leverages an existing pipetting robot (OT2-Pipettes, Opentrons, Long Island City, NY, United States) for precision liquid transfer. Customized 96-well plate holders and cassette holders driven by stepper motors are used to convey 96-well plates and LFIA cassettes into and out from the machine. Position sensors are installed to ensure precision and repeatability. A customized heating unit is installed under the 96-well plate to enable LAMP reaction heating. The colorimetric reaction readouts are detected using an overview camera (Flea3 USB3, Model: FL3-U3-13E4C-C, Teledyne FLIR LLC). A process chiller unit (Temperature Module, Opentrons) is adopted for liquid storage (e.g., LAMP reagents).

The machine is controlled by a desktop computer and a two-level user interface. The first level user interface opens to the system developers, which includes the system installation and calibration access. After initial installation and calibration, the second level user interface is opened to system operators for information loading and result display. Given the simplicity of the graphical user interface (GUI), system operators can be trained in minutes.

2.3.2 System Automation and Overarching Workflow

Nasopharyngeal swabs are collected from patients using a nasal swab and stored in iSwab Microbiome-EL (Extraction-Less) buffer (MAWI DNA Technologies, Hayward, CA, United

States). Collected patient samples are loaded into the sample holder by a human operator (Figure 1B). All reagents are stored on top of the process chiller unit. Upon initialization, 96-well plates and cassettes filled with LFIA are conveyed into the LAMP reaction zone and the lateral flow assay zone, respectively. After the system operator enters the sample information (e.g., number of samples, sample identification numbers), the machine first loads the pre-mixed LAMP reaction concoction (Table 2.1, Table 2.2) into a new 96-well plate. Next, the machine pipettes 2 µl of each patient sample into a single well in the 96-well plate. Pipette tips are changed after each sample to prevent cross-contamination of samples. Once all samples are loaded, the heating unit under the LAMP reaction zone heats the plate up to 65°C. A system timer starts once it reaches 65°C. After a preset reaction time (15–30 min), the RT-LAMP reaction is complete and positive samples are clearly identifiable by a colorimetric change from red to yellow. The colorimetric change is detected and quantitatively measured by the overview camera (Flea3 USB3, Model: FL3-U3-13E4C-C, Teledyne FLIR LLC), and the process is complete for samples that meet the threshold for a negative result. For samples that meet the criteria for a positive result, 3 µl of the LAMP product is mixed with 40 µl of running buffer (1 × PBS, pH 7.4 with 2% Tween 20) and deposited onto a lateral flow immunoassay. A system timer begins, and the result is detected and quantified after a predetermined amount of time. On the lateral flow immunoassay, positive results for each specific viral gene target will appear as a characteristic crimson line. A fourth crimson line acts as a control line and serves to validate the test. The positive readings which stand for the presence of COVID-19 RT-LAMP products are visible after 5 to 10 min using the LFIA. The colorimetric change of the LFIA is detected using the overview camera and then quantitatively measured on the computer. The final result for each sample is displayed on the user interface and a Portable Document Format (PDF) file including the sample information and detection results will be

automatically stored in the local disk (or on the cloud if internet access is enabled). The system automatically displays a warning window on the user interface for 96-well plates and cassettes replenishment when needed (e.g., all the wells have been used).

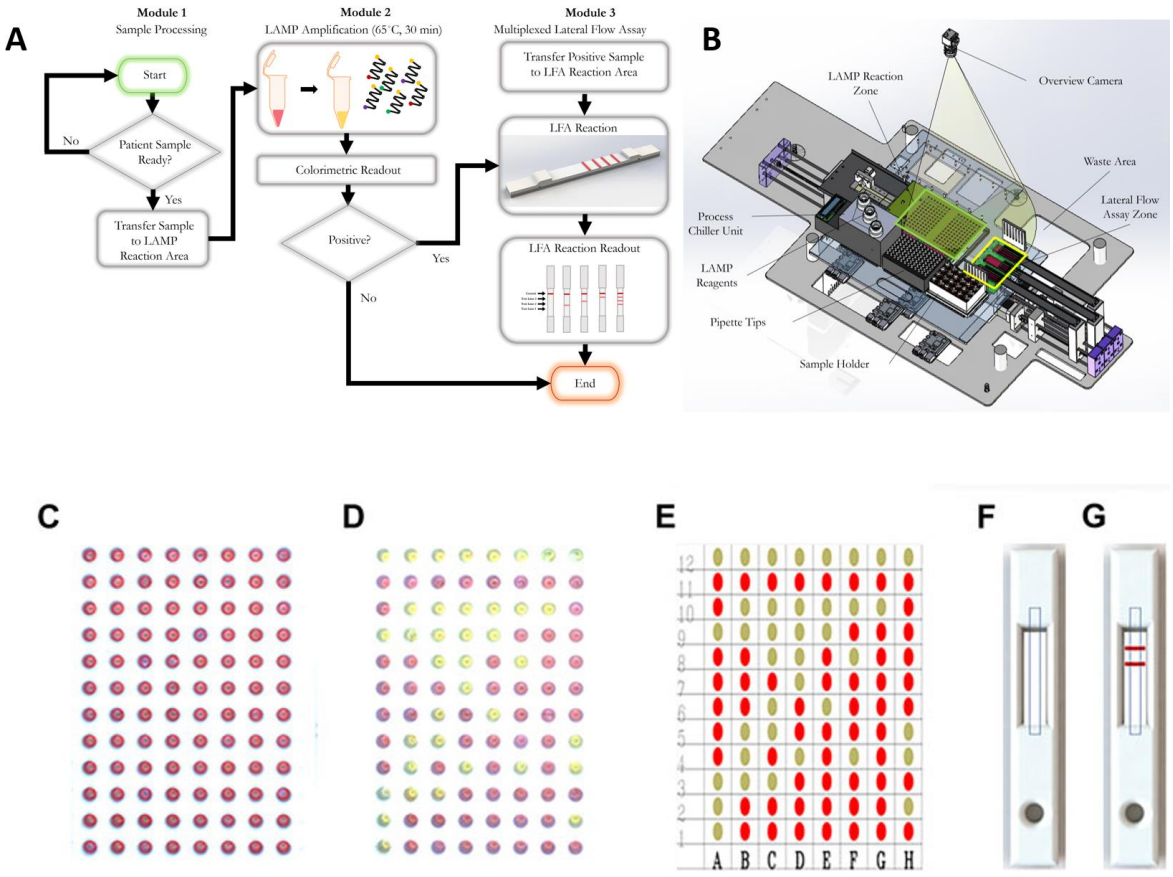

Figure 2.1: The workflow of our RT-LAMP-LFIA prototype system and the schematic of our automatic system. A) Workflow schematic from initial patient sample placement to end. Samples undergo a colorimetric loop-mediated isothermal amplification reaction. Samples that are positive (as indicated by a colorimetric change from red to yellow) are transferred to a multiplexed lateral flow assay test strip, which can differentiate from up to three target sequences. B) Machine schematic. (C) Example 96-well plate image captured by the overview camera before RT-LAMP reaction. The red circle represents the region of interest (ROI) of each well. The decision matrix is determined by the color change within the red circles. (D) Example 96-well plate image captured by the overview camera after RT-LAMP reaction. (E) Final decision matrix for RT-LAMP reaction readout. (F) Example rendering of LFIA cassette image captured by the overview camera before LFIA. Dashed rectangles represent ROIs of the LFIA cassettes. (G) Example rendering of LFIA cassette image captured by the overview camera after LFIA.

2.3.3 RT-LAMP Primer Design and Viral Targets Information

RT-LAMP primers against Nucleocapsid (N-2), Envelope (E-2), and ORFla-1 genes (Table 2.3) were designed according to previously published specifications [51]and were synthesized by Integrated DNA Technologies (IDT, San Diego, CA, USA). The sequence of primers and concentrations of each oligonucleotide in the 10x primer mix are shown in Tables 2.1 and 2.2. The 10x primer mix was prepared by dissolving the oligonucleotides in nuclease-free water. It was stored at -20 ℃ before using.

The RT-LAMP primer sets corresponding to the N-2, E-2, and ORF1a-1 genes were each designed to incorporate a unique tag onto each amplified RT-LAMP product. Texas Red was labeled on the 5’ end of the E-2 LF primer, FITC was labeled on the 5’ end of the N-2 FIP primer, and Digoxigenin was labeled on the 5’ end of the ORF1a-1 FIP primers. Biotin was labeled on the 5’ end of the LB primers for all three genes. Accordingly, Anti-Texas Red, Anti-Fluorescein, and Anti-Digoxigenin antibodies were striped onto the nitrocellulose membrane of the LFIA as test lines, while the biotin-BSA was used as the control line. Streptavidin gold nanoparticles (Streptavidin, 40nm 10 OD Colloidal Gold, Attogene, TX, USA) served as the reporter particle. Therefore, the RT-LAMP products for each gene only bind to one test line, enabling the detection of up to three distinct viral gene target detections on a single LFIA. Because in this instance all three gene targets were from RNA from the same virus and thus competition between templates can occur, gene blocks (sub-sequences of the entire SARS-CoV-2 RNA template) are used to validate the test. In the clinical and contrived viral tests, competition between primer sets can obscure some gene sequences on the LFIA; however, the RT-LAMP colorimetric change from red to yellow will be unaffected.

The SARS-CoV-2 RNA (VR-3280SD) was purchased from the American Type Culture Collection (ATCC, Manassas, Virginia, USA). The COVID-19 RNA was diluted as necessary by nuclease-free water. The Nucleocapsid (N), Envelope (E), and ORF1ab gene blocks were synthesized by Integrated DNA Technologies (IDT, IA, USA), with sequences shown in Table 2.4.

Table 2.1: Concentrations of each oligonucleotide in the 10x primer mix

Primer	10X Concentration (Stock)	1X Concentration (Final)
FIP	16 µM	1.6 µM
BIP	16 µM	1.6 µM
F3	2 µM	0.2 µM
B3	2 µM	0.2 µM
LF	8 µM	0.8 µM
LB	8 µM	0.8 µM

Table 2.2: Concentrations of each reagent in the RT-LAMP assay

Reagents	Volume
WarmStart Colorimetric LAMP 2X Master Mix	10 µL
LAMP Primer Mix (10X)	2 µL
Guanidine Hydrochloride	2 µL
Nasopharyngeal Swab Sample	2 µL
dH_2O	4 µL
Total Volume	20 µL

Table 2.3: Primer sequences against Nucleocapsid (N-2), Envelope (E-2), and Orf1a-1 genes of the SARS-CoV-2 virus

Gene Target	Primer	Name	Tag	Sequence
N2	FIP	N2 FIP	5'-FITC	TGCGGCCAATGTTTGTAATCAGCCAAGGAAATTTTGGGGAC
	BIP	N2 BIP	-	CGCATTGGCATGGAAGTCACTTTGATGGCACCTGTGTAG
	F3	N2 F3	-	AACACAAGCTTTCGGCAG
	B3	N2 B3	-	GAAATTTGGATCTTTGTCATCC
	LF	N2 LF	-	TTCCTTGTCTGATTAGTTC
	LB	N2 LB	5'-Biotin	ACCTTCGGGAACGTGGTT
Orf1a	FIP	Orf1a FIP	5'-DigN	GAGGGACAAGGACACCAAGTGTATGGTTGAGCTGGTAGCAGA
	BIP	Orf1a BIP	-	CCAGTGGCTTACCGCAAGGTTTTAGATCGGCGCCGTAAC
	F3	Orf1a F3	-	CTGCACCTCATGGTCATGTT
	B3	Orf1a B3	-	AGCTCGTCGCCTAAGTCAA
	LF	Orf1a LF	-	CCGTACTGAATGCCTTCGAGT
	LB	Orf1a LB	5'-Biotin	TTCGTAAGAACGGTAATAAAGGAGC
E2	FIP	E2 FIP	-	ACCTGTCTCTTCCGAAACGAATTTGTAAGCACAAGCTGATG
	BIP	E2 BIP	-	CTAGCCATCCTTACTGCGCTACTCACGTTAACAATATTGCA
	F3	E2 F3	-	CCGACGACGACTACTAGC
	B3	E2 B3	-	AGAGTAAACGTAAAAAGAAGGTT
	LF	E2 LF	5'-TexRed	TCGATTGTGTGCGTACTGC
	LB	E2 LB	5'-Biotin	TGAGTACATAAGTTCGTAC

Table 2.4: Sequences of N, E, and Orf1ab gene blocks

Gene Blocks	Sequence
N gene (229 nt)	AACACAAGCTTTCGGCAGACGTGGTCCAGAACAAACCCAAGGA AATTTTGGGGACCAGGAACTAATCAGACAAGGAACTGATTACAA ACATTGGCCGCAAATTGCACAATTTGCCCCCAGCGCTTCAGCGTT CTTCGGAATGTCGCGCATTGGCATGGAAGTCACACCTTCGGGAA CGTGGTTGACCTACACAGGTGCCATCAAATTGGATGACAAAGAT CCAAATTTC
E gene (234 nt)	CCGACGACGACTACTAGCGTGCCTTTGTAAGCACAAGCTGATGA GTACGAACTTATGTACTCATTCGTTTCGGAAGAGACAGGTACGTT AATAGTTAATAGCGTACTTCTTTTTCTTGCTTTCGTGGTATTCTTG CTAGTTACACTAGCCATCCTTACTGCGCTTCGATTGTGTGCGTAC TGCTGCAATATTGTTAACGTGAGTCTTGTAAAACCTTCTTTTTAC GTTTACTCT
Orf1ab gene (289 nt)	TCCAGATGAGGATGAAGAAGAAGGTGATTGTGAAGAAGAAGAG TTTGAGCCATCAACTCAATATGAGTATGGTACTGAAGATGATTA CCAAGGTAAACCTTTGGAATTTGGTGCCACTTCTGCTGCTCTTCA ACCTGAAGAAGAGCAAGAAGAAGATTGGTTAGATGATGATAGT CAACAAACTGTTGGTCAACAAGACGGCAGTGAGGACAATCAGA CAACTACTATTCAAACAATTGTTGAGGTTCAACCTCAATTAGAG ATGGAACTTACACCAGTTGTTCAGACT

2.3.4 Lateral Flow Immunoassay

The lateral flow immunoassay (LFIA) (Figure 2. 2) was comprised of a conjugate pad (GFCP203000 Glass Fiber Conjugate Pad Sheets, Millipore Sigma, St. Louis, MO, USA), a nitrocellulose membrane (Whatman FF120HP, Cytiva Life Sciences, Marlborough, MA, USA), an absorbent pad (Blotting Paper, Grade 222, Ahlstrom-Munksjö, Helsinki, Finland), and a backing card (DCN Diagnostics, Carlsbad, CA, USA). The dimensions of the conjugate pad were 2 cm x 30 cm; the dimensions of the nitrocellulose membrane were 2.5 cm x 30 cm; the dimensions of the absorbent pad were 2 cm x 30 cm); and the dimensions of the backing card were 6 cm x 30 cm. The conjugate pad was soaked in a blocking solution (1% bovine serum albumin + .05%

Tween 20 + 0.2% sucrose, diluted in PBS) on a shaker at low speed for 10 min and the conjugate pads were dried on a drying rack overnight. Anti-texas red antibody (anti-TexR, 1 mg/ml, Cat. # A-6399, ThermoFisher Scientific, Waltham, MA, USA), rabbit anti-fluorescein antibody (anti-FITC, 1 mg/ml, Cat. # ab19491, Abcam, Cambridge, UK), sheep anti-digoxigenin antibody (anti-DigN, 2.5 mg/ml, Cat. # 3210-0488, Bio-Rad, Hercules, CA, USA) and biotinylated bovine serum albumin (biotin-BSA, 3 mg/ml, Cat. #B-2007-10, Vector Labs, Burlingame, CA, USA) were striped at the detection regions on the nitrocellulose using a lateral flow reagent dispenser (Claremont Biosolutions, Upland, CA, USA) at test line 1 (TL1), test line 2 (TL2), test line 3 (TL3) and control line (Ctrl), respectively, with each line separated by 5 mm. The membranes were then assembled together and the assembled LFIA were cut into 4-mm dipsticks. Then, 3 µL of streptavidin gold nanoparticles (Streptavidin, 40nm 10 OD Colloidal Gold, Attogene, TX, USA) were immobilized at one end of the conjugate pad for each strip and dried in a vacuum. The dipsticks were packaged in a plastic cassette (DCNDx, Carlsbad, CA, USA) and stored in a 4°C fridge in a heat-sealed foil packet with a silica gel desiccant until use. The LFIAs were tested three months later and found to still be viable.

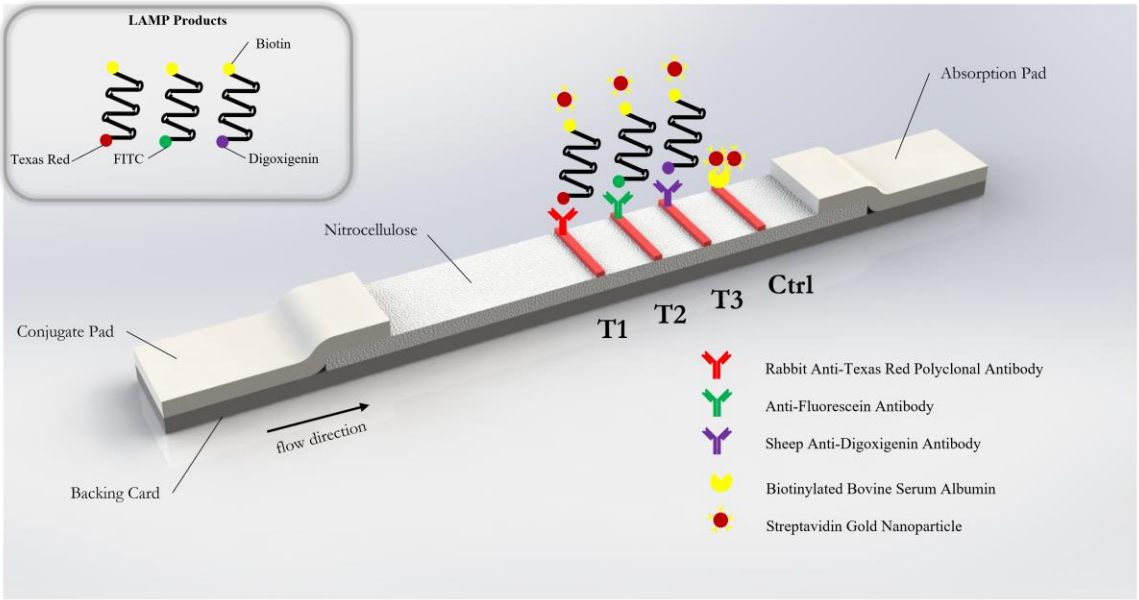

Figure 2.2: Schematic of gold nanoparticle based lateral flow immunosorbent assay for the detection of SARS-CoV-2 Orf1a, N2, and E2 target genes.

2.3.5 Quantification of the RT-LAMP Reaction and LFIA Readout

The colorimetric change of the RT-LAMP reaction is quantitatively measured by the overview camera (Flea3 USB3, Model: FL3-U3-13E4C-C, Teledyne FLIR LLC). The prototype algorithm identifies the region of interest (ROI) of all RT-LAMP wells in the 96-well plate. The grayscale and red values of each well are evaluated inside the ROI. In each batch, at least three negative samples are present to serve as negative controls. The average value of the red/grayscale value of these negative controls are used to normalize the red/grayscale value for every well. Intuitively, a larger red/grayscale value means that the sample is more red, corresponding to a negative result of colorimetric RT-LAMP. A smaller red/grayscale value means that the sample is less red – and thus a colorimetric change from red to yellow has occurred. Accordingly, our algorithm assigns a cutoff value of >0.98 for negative samples and <0.98 for positive samples.

Independently, the same algorithm was employed using the built-in tools of ImageJ for quantification for the experiments denoted in the Results section.

2.3.6 Clinical Sample Handling and RT-qPCR

Clinical samples were obtained from the UCSD COVID-19 Research Biobank (University of California, San Diego, CA, USA). Nasopharyngeal swabs from patients both positive and negative for the SARS-CoV-2 virus were collected in iSwab Microbiome-EL (Extraction-Less) buffer. Collected samples were aliquoted into freezer tubes in a BSL2+ hood and were stored at -80°C prior to use. RT-qPCR was performed on all samples. Cq values are noted in Table 2.5.

2.4 RESULTS

2.4.1 Time-to-Result Test

WarmStart Colorimetric LAMP 2X Master Mix and guanidine hydrochloride solution (New England Biolabs, Ipswich, MA, USA) were used to detect the SARS-CoV-2 RNA template. The RNA template was diluted by nuclease-free water into samples with 3, 5, 10, 25, 50, 100, and 1000 genome copies/ well. The three custom RT-LAMP primers against Nucleocapsid (N-2), Envelope (E-2), and ORFla-1 genes (Table 2.3) were mixed together. The colorimetric RT-LAMP reaction was conducted at 65℃ and imaged after 15 minutes and 30 minutes. The test demonstrated a sensitivity of 3 copies/well of SARS-CoV-2 RNA template after 15 minutes, as observed by the red to yellow color change, while the negative sample stayed red after the reaction (Figure 2.3). The 30 minute time point was chosen for subsequent experiments to allow ample time for the reaction to proceed to completion.

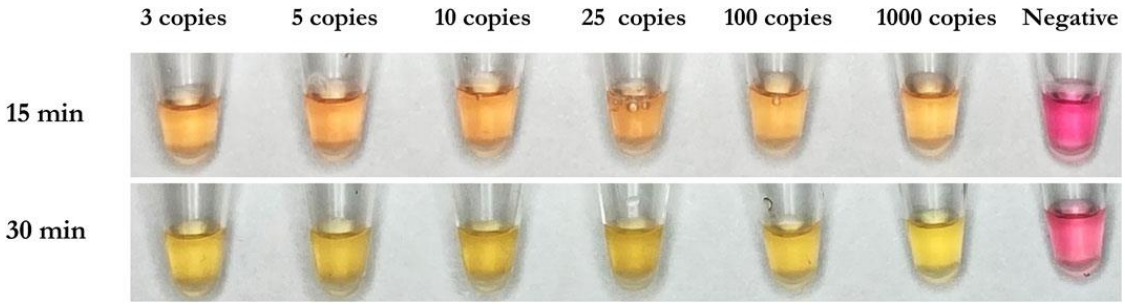

Figure 2.3: Demonstrative colorimetric loop-mediated isothermal reaction using primers as listed in Table 2.1. Viral RNA from SARS-CoV-2 (ATCC) were spiked in the amounts of 0, 3, 5, 10, 25, 100, and 1,000 RNA copies per microwell and reactions were imaged after 15 and 30 min, respectively.

2.4.2 Multiplexed Gene Detection by Colorimetric RT-LAMP and LFIA

Using each single gene block (N, E, and Orf1ab), RT-LAMP reactions were carried out in triplicate with all three primers present. Following the reaction, 3 µL of LAMP product was applied to the sample region of the LFIA with 40 µL of running buffer. As expected, only one positive line relative to the corresponding amplified RT-LAMP product was observed on each strip, confirming that in the presence of a single non-competing RNA template (gene block), the three mixed primer sets from Orf1a, E-2, and N-2 genes will produce a single positive result on the LFIA corresponding to their appropriate tag (Digoxigenin, Texas Red, or Fluorescein). The no template control showed no result at any test line. Accumulation of streptavidin AuNPs at the control line was observed in all cases. Results are depicted in Figure 2.4.

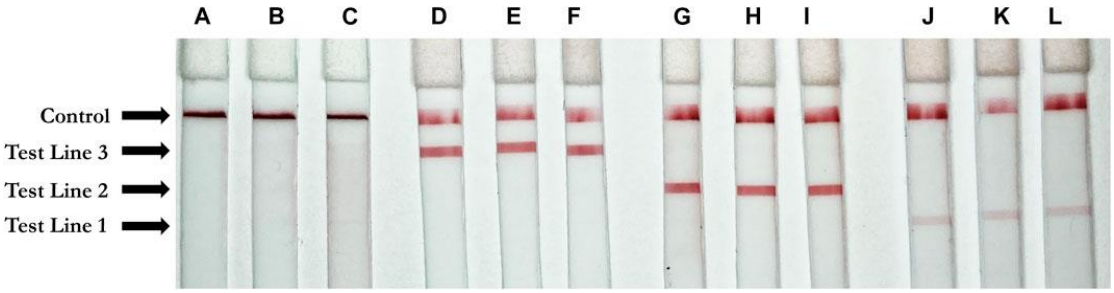

Figure 2.4: Positive test results for three unique gene blocks (subsections of SARS-CoV-2 viral genome). Test Line 1 (Texas Red Antibody, 1 mg/ml, Cat. #A-6399, ThermoFisher Scientific, Waltham, MA, United States); Test line 2 (Fluorescein antibody, 1 mg/ml, Cat. #ab19491, Abcam, Cambridge, United Kingdom); Test Line 3 (Digoxigenin antibody, 2.5 mg/ml, Cat. #3210-0488, Bio-Rad, Hercules, CA, United States); Control line (biotinylated bovine serum albumin, 3 mg/ml, Cat. #B-2007-10, Vector Labs, Burlingame, CA, United States) (A–C) Negative control. (D–F) Orf1a gene block (1 ng/µl) (G–I) N gene block (1 ng/µl) (J–L) E gene block (1 ng/µl).

2.4.3 Sensitivity of Colorimetric RT-LAMP and LFIA

To test the sensitivity of the colorimetric RT-LAMP reaction of the SARS-CoV-2 RNA template, N-2, E-2, and ORF1a-1 primer sets were added individually and together in colorimetric RT-LAMP master mix solutions with 3, 5, 10, 25, 50, 100, and 1000 RNA copies per well (Figure 2.5). All conditions were tested in triplicate. All positive samples turned yellow within 30 mins, while negative samples remained red. The results were quantified using red/grayscale values measured by ImageJ. Positive samples amplified by primer sets alone or together were distributed between 0.9 to 0.96. For negative samples, these values were around 1. For RT-LAMP products amplified by one set of primers, 3 µL of each amplification product was run on the LFIA. As expected, only one positive line relative to the appropriate amplified gene was observed on each strip for all positive samples.

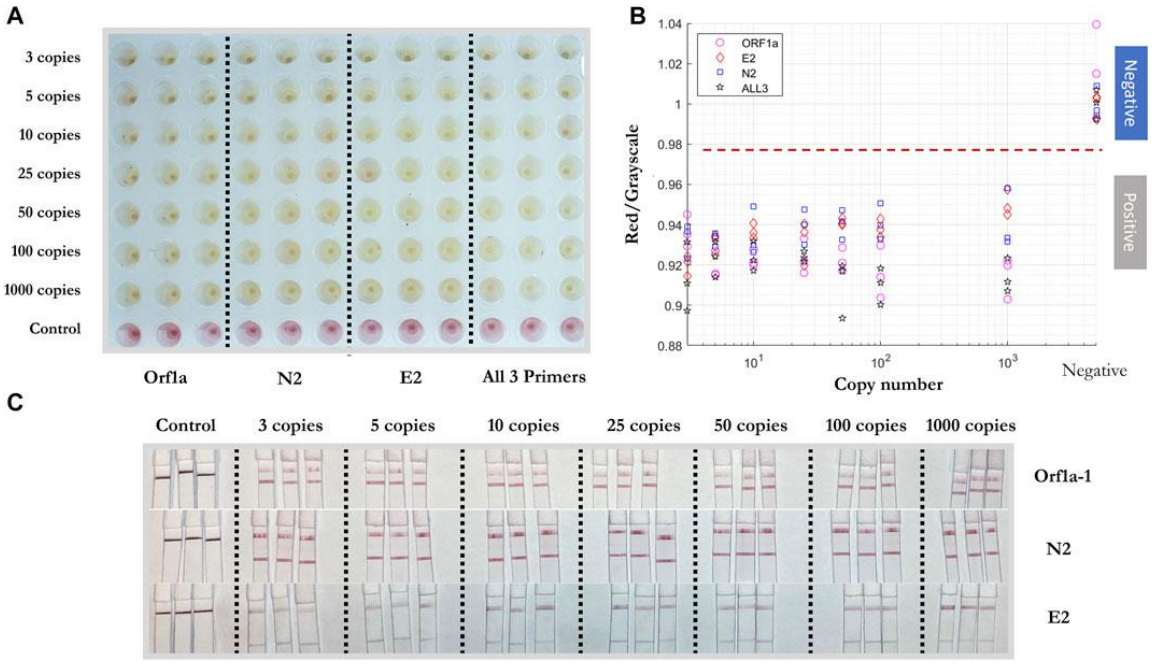

Figure 2.5: Sensitivity test of colorimetric RT-LAMP reaction and LFIA of artificial SARS-CoV-2 RNA template. (A) Positive/negative RT-LAMP products with ORF1a-1, N-2, E-2, and all three primer sets after the reaction, taken by overview camera. (B) Red/grayscale value vs. RNA copy numbers of both positive and negative samples. (C) LFIA read-outs for RT-LAMP products amplified for ORF1ab, N, and E gene blocks.

To test the reproducibility of the RT-LAMP-LFIA prototype system at the lower limit of detection, all three primers were added into the RT-LAMP master mix with 3 copies of SARS-CoV-2 RNA template for twenty replicates, with triplicates of negative controls. The experiment was carried out at 65℃ for 30 min. A red to yellow color change was observed by the prototype camera from above. The red/grayscale values measured by ImageJ distributed below 0.98 for positive samples, while the values for negative control samples were around 1 (Figure 2.6).

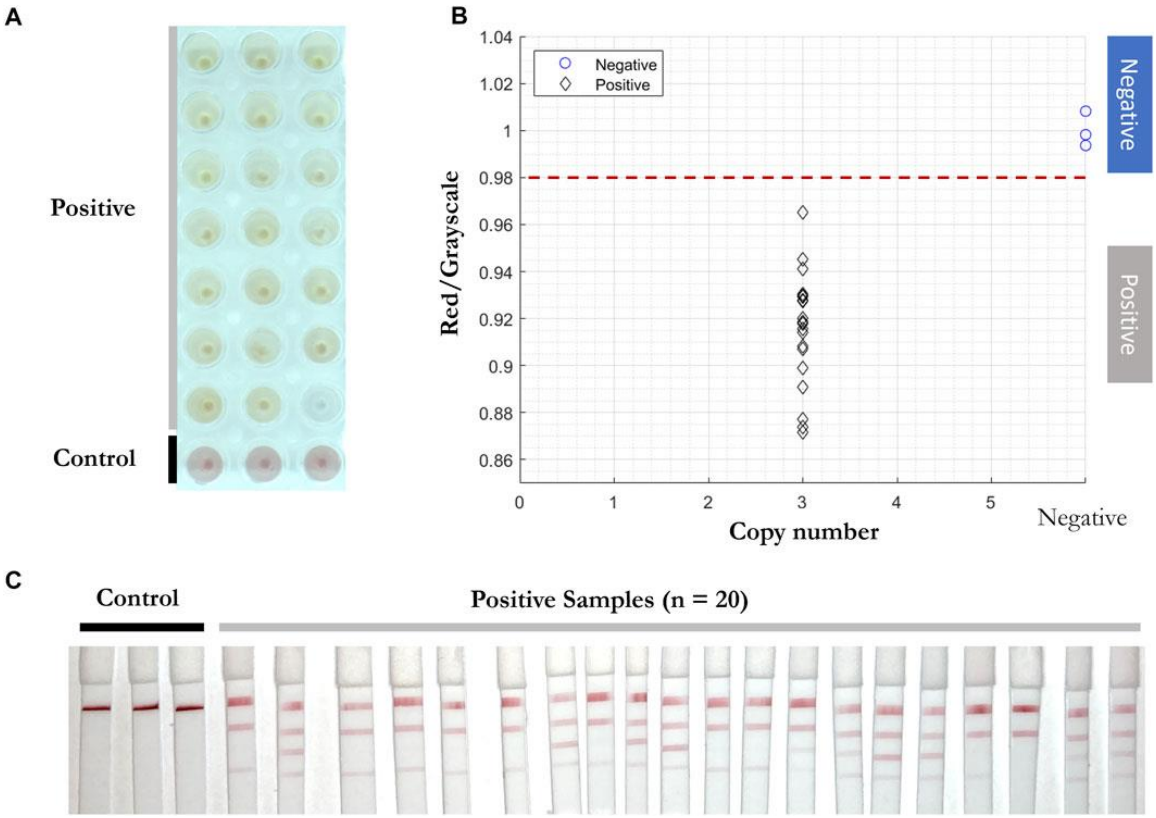

Figure 2.6: Reproducibility test of RT-LAMP-LFIA prototype system at the lower limit of detection. (A) RT-LAMP products from 3 initial template copies (n = 20) and negative control samples (n = 3) after the reaction, taken by overview camera. (B) Red/grayscale vs. copy numbers of both positive and negative samples. (C) LFIA read-outs for RT-LAMP products amplified for all three genes.

As expected, 5 to 10 minutes after adding the RT-LAMP products and running buffer onto each conjugate pad of the LFIA, different positive readings were shown. In the presence of a single RNA target and three sets of primers, competition for a limited amount of template strands means that some reactions can overtake others. As a self-limiting reaction, the process stops when a certain amount of products form or the reaction reaches certain (acid) pH values. Therefore, the amount of N-2, E-2, and ORF1a-1 primer sets' amplified products can vary and show different positive read-outs on the LFIA (Figure 2.6C).

2.4.4 Validation of RT-LAMP and LFIA for Inactivated Whole Viral Particles

RT-qPCR [52][53]and RT-LAMP assays [54] [55] are compatible with direct testing of nasopharyngeal and oropharyngeal swab specimens without an RNA purification or extraction step. To test the efficiency of RT-LAMP and LFA, inactivated viral particles (ATCC, VR-1986HK) diluted into 3, 5, 10, 25, 50, 100, and 1000 copies were added in the RT-LAMP master mix with the three gene primer sets (Figure 2.7). After 30 mins at 65 ℃, a red to yellow color change was captured in wells with the inactivated viral particles by the prototype system camera. The red/grayscale value as measured by ImageJ for positive samples was distributed at around 0.94, while all the negative samples had red/grayscale values above 0.98. Next, 3 µL of each amplification product was mixed with 40 µL of running buffer before being deposited on the conjugate pad of a LFIA strip. Positive read-outs were mainly observed for ORF1a-1 gene amplified products (Figure 2.7C) as a result of primers competing during the self-limiting RT-LAMP reaction.

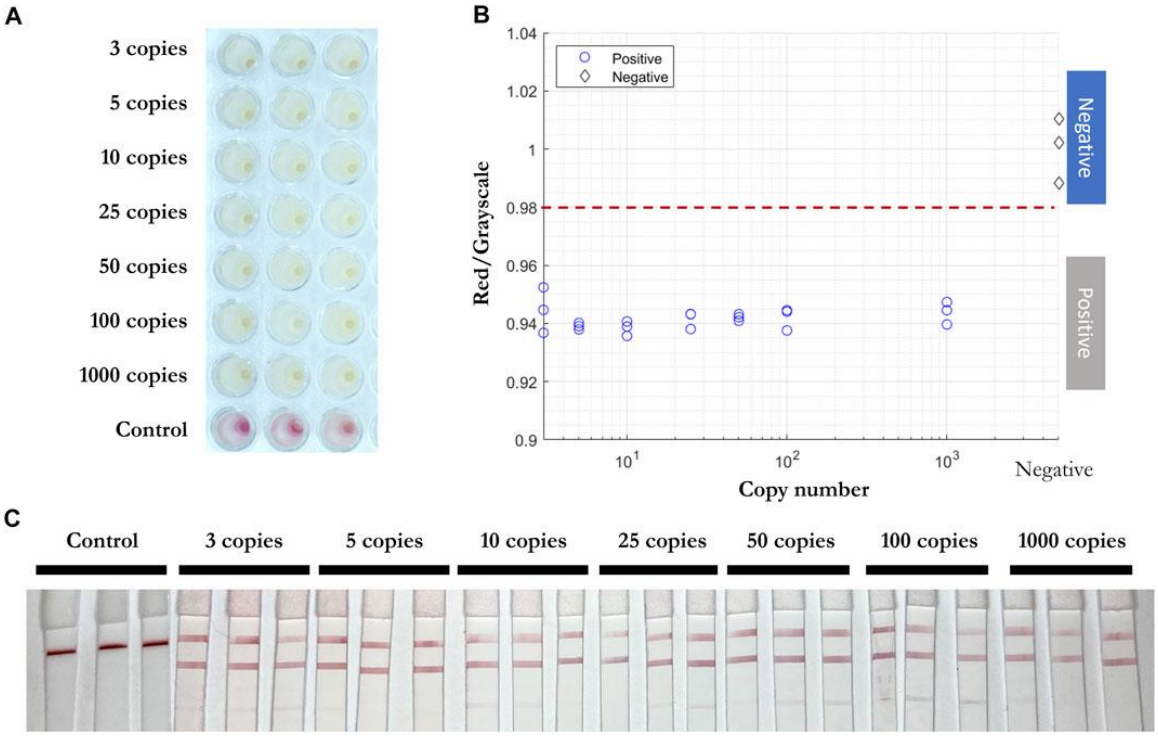

Figure 2.7: Direct RT-LAMP-LFIA testing of inactivated viral particles without prior RNA purification or extraction. (A) RT-LAMP products for inactivated viral particles (3, 5, 10, 25, 50, 100, and 1,000 copies) and negative control samples with three sets of primers, taken by overview camera. (B) Red/grayscale vs. copy numbers of both positive and negative samples. (C) LFIA read-outs for RT-LAMP products amplified for all three genes.

Next, inactivated viral particles were spiked into unique negative patient swab samples preserved in iSwab Microbiome-EL (Extraction-Less) buffer to mimic patient-to-patient variation of conditions in amounts of 3, 5, 10, 25, 50, 100, and 1000 copies per reaction. All samples were red prior to the RT-LAMP reaction, and positive samples were yellow after 30 minutes at 65 °C. The red/grayscale values of positive samples were consistently below 0.96, while the negative samples were distributed around 1 (Figure 2.8). Due to primers competing during the self-limiting RT-LAMP reaction, positive read-outs on the LFIA were mainly observed for ORF1a-1 gene amplified products (Figure 2.8C).

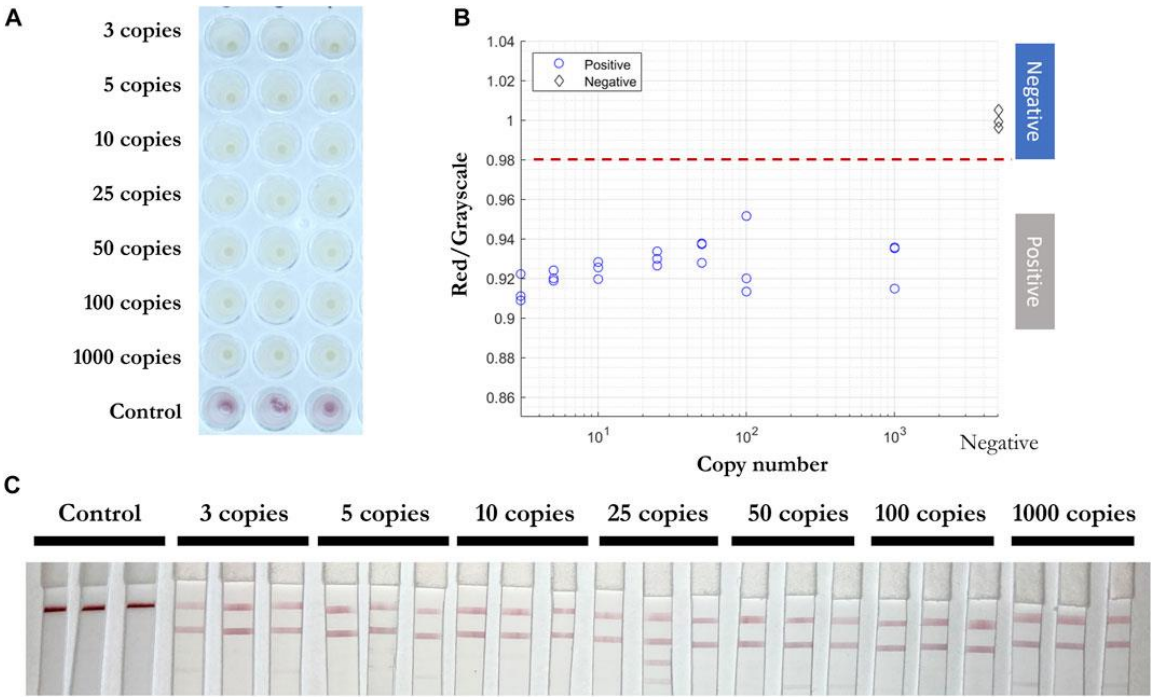

Figure 2.8: Direct RT-LAMP-LFIA testing of spiked inactivated viral particles in nasopharyngeal swab specimens without a prior RNA purification or extraction. (A) RT-LAMP products for inactivated viral particles spiked in nasopharyngeal swab specimens (3, 5, 10, 25, 50, 100, and 1,000 copies) and negative control samples with three sets of primers, taken by overview camera. (B) Red/grayscale vs. copy numbers of both positive and negative samples. (C) LFIA read-outs for RT-LAMP products amplified for all three genes.

2.4.5 Validation of RT-LAMP and LFIA for Clinical Samples

2 µL of solution from 30 positive and 30 negative clinical samples (Table 2.5) were added into RT-LAMP master mix with all three primer sets present. The positive samples turned yellow within 30 mins at 65 ℃ and had red/grayscale values between 0.9 and 0.94. The negative samples remained red with red/grayscale values above 0.98 as quantified by ImageJ (Figure 2.9). For positive samples, read-outs were observed for all samples on at least one test line on the LFIA (Figure 2.9C).

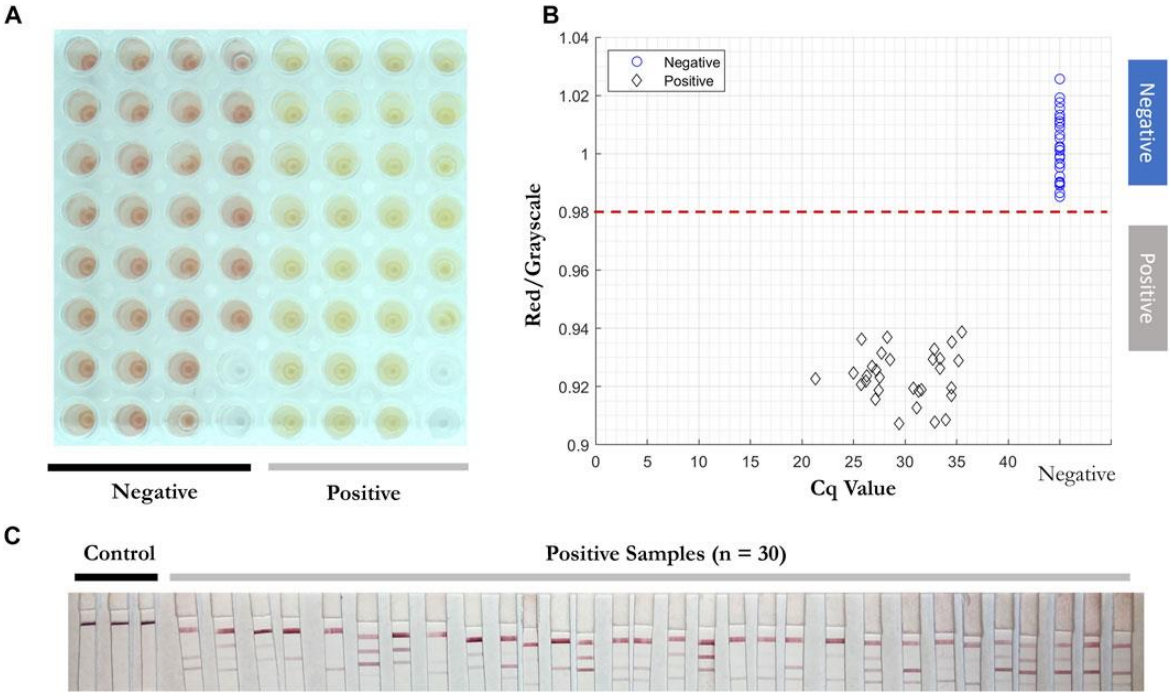

Figure 2.9: Direct RT-LAMP-LFIA testing of 30 positive and 30 negative clinical nasopharyngeal swab specimens without a prior RNA purification or extraction. (A) RT-LAMP products for 30 positive and 30 negative clinical samples amplified with three sets of primers, taken by overview camera. (B) Red/grayscale vs. copy numbers of both positive and negative samples. (C) LFIA read-outs for RT-LAMP products amplified for all three genes.

Table 2.5: Cq Values Obtained from RT-QPCR for Clinical Nasopharyngeal Specimens

Sample No.	Test Result	Cq Value
1-30	Negative	Undetectable
31	Positive	27.514
32	Positive	33.405
33	Positive	25.0205
34	Positive	27.708
35	Positive	28.526
36	Positive	32.840
37	Positive	27.422
38	Positive	32.859
39	Positive	30.810
40	Positive	29.406
41	Positive	27.204
42	Positive	32.703
43	Positive	35.175
44	Positive	25.782
45	Positive	21.299
46	Positive	34.516
47	Positive	26.791
48	Positive	31.589
49	Positive	27.127
50	Positive	25.745
51	Positive	26.304
52	Positive	26.203
53	Positive	31.114
54	Positive	34.482
55	Positive	33.929
56	Positive	28.251
57	Positive	34.532
58	Positive	35.496
59	Positive	33.400
60	Positive	31.301

2.5 DISCUSSION

In this paper, we presented a semi-automated RT-LAMP-LFIA prototype system and evaluated its capability to test nasopharyngeal swab samples from patients without a prior RNA purification or extraction step. The system is almost fully automated and does not require highly trained personnel or specialized laboratory equipment such as thermocyclers. The simple design and automated sample-to-answer workflow indicate that our system is suitable for implementation in high-traffic community settings such as airports or event centers for rapid and easy to use point-of-care diagnostics.

We tested RT-LAMP primer sets for N, E, and ORF1ab genes of the SARS-CoV-2 virus and validated their results on the LFIA. Multiplexing of colorimetric RT-LAMP reactions in a single pot for the SARS-CoV-2 gene targets accelerated the reaction to yield results within 15 minutes. Moreover, the multiplexed read-out of up to 3 genes on a single LFIA can further distinguish multiple viral public health threats on the same platform - for example, SARS-CoV-2, Ebola, and yellow fever.

One limitation of the use of the RT-LAMP-LFIA workflow is the comparatively long development time for creating custom RT-LAMP primers. While established viral diseases often have RT-LAMP primer sequences readily available from publications or commercially, new and emerging diseases must first undergo the primer design process. Thus, the RT-LAMP-LFIA system may have a longer lead time for new diseases in comparison to other established methods such as RT-qPCR.

2.6 SUPPLEMENTARY

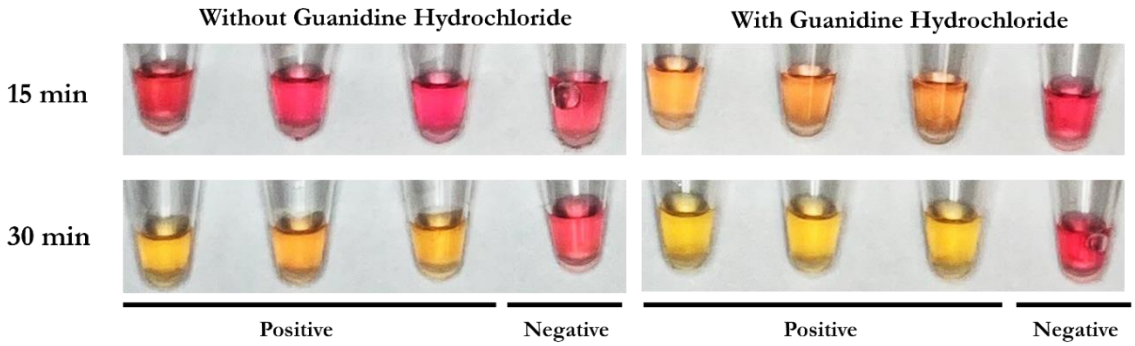

Figure S2.1: Comparison of LAMP reaction times with and without guanidine hydrochloride. LAMP reactions with and without guanidine hydrochloride were heated in dry bath at 65˚C for 15 min and 30 min. Positive samples contained 1000 copies of SARS-Cov-2 RNA. Negative samples contained water.

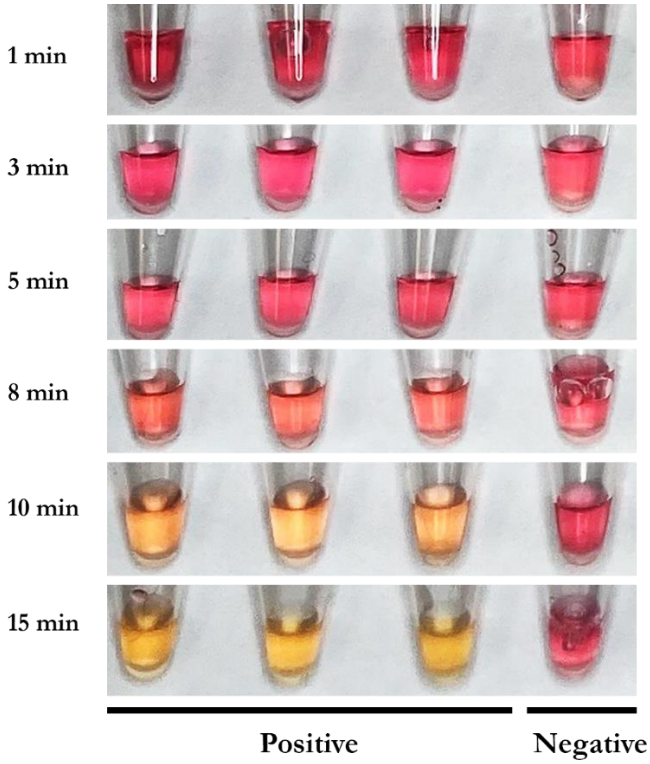

Figure S2.2: LAMP reaction color change progression over time. LAMP samples with guanidine hydrochloride were heated in dry bath at 65˚C for 1, 3, 5, 8, 10 and 15 min, respectively. Positive samples contained 1000 copies of SARS-Cov-2 RNA. Negative samples contained water.

2.7 REFERENCES

[34] Wang, C., Horby, P. W., Hayden, F. G., and Gao, G. F. (2020). A Novel Coronavirus Outbreak of Global Health Concern. The Lancet 395 (10223), 470–473. doi:10.1016/S0140-6736(20)30185-9

[35] World Health Organization (2021). WHO Coronavirus (COVID-19) Dashboard. Available at: https://covid19.who.int/.

[36] Baker, R. E., Mahmud, A. S., Miller, I. F., Rajeev, M., Rasambainarivo, F., Rice, B. L. (2021). Infectious Disease in an Era of Global Change. Nat. Rev. Microbiol 20, 193–205. doi:10.1038/s41579-021-00639-z

[37] Pavia, A. T. (2007). Germs on a Plane: Aircraft, International Travel, and the Global Spread of Disease. J. Infect. Dis. 195 (5), 621–622. doi:10.1086/511439

[38] Luo, Z., Wang, W., Ding, Y., Xie, J., Lu, J., Xue, W.. (2021). Epidemiological Characteristics of Infectious Diseases Among Travelers between China and Foreign Countries before and during the Early Stage of the COVID-19 Pandemic. Front. Public Health 9. doi:10.3389/fpubh.2021.739828

[39] Hu, B., Guo, H., Zhou, P., and Shi, Z.-L. (2020). Characteristics of SARS-CoV-2 and COVID-19. Nat. Rev. Microbiol. 19, 141–154. doi:10.1038/s41579-020- 00459-7

[40] Oeschger, T. M., McCloskey, D. S., Buchmann, R. M., Choubal, A. M., Boza, J. M., Mehta, S. (2021). Early Warning Diagnostics for Emerging Infectious Diseases in Developing into Late-Stage Pandemics. Acc. Chem. Res. 54 (19), 3656–3666. doi:10.1021/acs.accounts.1c00383

[41] Kralik, P., and Ricchi, M. (2017). A Basic Guide to Real Time PCR in Microbial Diagnostics: Definitions, Parameters, and Everything. Front. Microbiol. 8. doi:10.3389/fmicb.2017.00108

[42] Dao Thi, V. L., Herbst, K., Boerner, K., Meurer, M., Kremer, L. P., Kirrmaier, D. (2020). A Colorimetric RT-LAMP Assay and LAMP-Sequencing for Detecting SARS-CoV-2 RNA in Clinical Samples. Sci. Transl. Med. 12, 556. doi:10.1126/scitranslmed.abc7075

[43] Sahoo, P. R., Sethy, K., Mohapatra, S., and Panda, D. (2016). Loop Mediated Isothermal Amplification: An Innovative Gene Amplification Technique for Animal Diseases. Vet. World 9, 465–469. doi:10.14202/vetworld.2016.465-469

[44] Huang, W. E., Lim, B., Hsu, C. C., Xiong, D., Wu, W., Yu, Y. (2020). RTLAMP for Rapid Diagnosis of Coronavirus SARS-CoV-2. Microb. Biotechnol. 13 (4), 950–961. doi:10.1111/1751-7915.13586

[45] Mautner, L., Baillie, C.-K., Herold, H. M., Volkwein, W., Guertler, P., Eberle, U. (2020). Rapid point-of-care Detection of SARS-CoV-2 Using Reverse Transcription Loop-Mediated Isothermal Amplification (RT-LAMP). Virol. J. 17 (160). doi:10.1186/s12985-020-01435-6

[46] Thompson, D., and Lei, Y. (2020). Mini Review: Recent Progress in RT-LAMP Enabled COVID-19 Detection. Sensors Actuators Rep. 2, 100017. doi:10.1016/j. snr.2020.100017

[47] Koczula, K. M., and Gallotta, A. (2016). Lateral Flow Assays. Lateral Flow Assays" 60 60 (1), 111–120. doi:10.1042/EBC20150012

[48] Zhu, X., Wang, X., Han, L., Chen, T., Wang, L., Li, H. (2020). Multiplex Reverse Transcription Loop-Mediated Isothermal Amplification Combined with Nanoparticle-Based Lateral Flow Biosensor for the Diagnosis of COVID-19. Biosens. Bioelectron. 166, 112437. doi:10.1016/j.bios.2020.112437

[49] Chen, X., Wang, S., Tan, Y., Huang, J., Yang, X., and Li, S. (2021). Nanoparticle-Based Lateral Flow Biosensors Integrated with Loop-Mediated Isothermal Amplification for the Rapid and Visual Diagnosis of Hepatitis B Virus in Clinical Application. Front. Bioeng. Biotechnol. 9, 731415. doi:10.3389/fbioe.2021.731415

[50] Zhang, C., Zheng, T., Wang, H., Chen, W., Huang, X., Liang, J. (2021). Rapid One-Pot Detection of SARS-CoV-2 Based on a Lateral Flow Assay in Clinical Samples. Anal. Chem. 93 (7), 3325–3330. doi:10.1021/acs.analchem.0c05059

[51] Zhang, Y., Odiwuor, N., Xiong, J., Sun, L., Nyaruaba, R. O., Wei, H. (2020). Rapid Molecular Detection of SARS-CoV-2 (COVID-19) Virus RNA Using Colorimetric LAMP. Medrxiv. doi:10.1101/2020.02.26.20028373

[52] Smyrlaki, I., Ekman, M., Lentini, A., Rufino de Sousa, N., Papanicolaou, N., Vondracek, M. (2020). Massive and Rapid COVID-19 Testing Is Feasible by Extraction-free SARS-CoV-2 RT-PCR. Nat. Commun. 11. doi:10. 1038/s41467-020-18611-5

[53] Wee, S. K., Sivalingam, S. P., and Yap, E. P. H. (2020). Rapid Direct Nucleic Acid Amplification Test without RNA Extraction for SARS-CoV-2 Using a Portable PCR Thermocycler. Genes 11 (6), 664. doi:10.3390/genes11060664

[54] Lamb, L. E., Bartolone, S. N., Ward, E., and Chancellor, M. B. (2020). Rapid Detection of Novel Coronavirus/Severe Acute Respiratory Syndrome Coronavirus 2 (SARS-CoV-2) by Reverse Transcription-Loop-Mediated Isothermal Amplification. PLoS ONE 15, e0234682. doi:10.1371/journal.pone.0234682

[55] Rabe, B. A., and Cepko, C. (2020). SARS-CoV-2 Detection Using Isothermal Amplification and a Rapid, Inexpensive Protocol for Sample Inactivation and Purification. Proc. Natl. Acad. Sci. U.S.A. 117, 24450–24458. doi:10.1073/pnas.2011221117

Acknowledgements

Chapter 2, in full, is a near-verbatim reprint of the material as it appears in Frontiers in Bioengineering and Biotechnology, 2022. Waller L*, Guo Z*, Tang R, Zhang Z, Wang E, Yasuhara-Bell J, Laurent L and Lo Y-H, Frontiers, 2022. The dissertation author was the co-primary investigator and author of this paper.

CHAPTER 3: NONTHERMAL PLASMA- BASED LIVE CELL LITHOGRAPHY

3.1 ABSTRACT

In this chapter, we demonstrate a novel prototype and concept for cold plasma – based live cell lithography (CPLCL). A plasma jet is formed using a custom dual – lead nozzle, high voltage alternating current transformer, nitrogen feed gas, and frame. The plasma temperature output is around 34˚ C. The concept aims to leverage the batch processing and spatial resolution advantages of lithography to identify, preserve, and isolate cells of interest while preserving their spatial information.

3.2 INTRODUCTION

3.2.1 Background of Spatial Biology Techniques and Motivation

Single- cell analysis techniques like scRNA-seq have proven to be an incredibly useful tool to enable the study of cellular heterogeneities across populations. However, cells do not act in isolation, but rather in concomitance with neighboring cells in the form of signaling molecules, cell-cell junctions, spatially segregated microenvironments, and mechanical stimulation. For many single-cell analysis techniques, individual cells from a tissue are dissociated from each other, obscuring critical insight into their native microenvironments. Consequently, recent scientific efforts have generated numerous spatially resolved techniques which assay cells directly from their location in a tissue cross-section. These techniques can be naturally classified into distinct categories, including microdissection, spatial in situ array capture, in situ hybridization (-ISH), and in situ sequencing (-ISS).

Microdissection is a widely employed strategy for physical dissection of tissue regions of interest via laser cutting. The most common microdissection technique is laser capture

microdissection (LCM) via infrared (IR) capture and ultraviolet (UV) cutting. [56] The basic premise of LCM involves (i) microscopic visualization and ROI selection, (ii) dissection of the ROIs via laser cutting, (iii) transfer of the dissected ROI to a thermolabile polymer, and (iv) removal of the dissected ROI for downstream experimentation. LCM is compatible with many tissue types, staining protocols, and fresh or preserved specimens. The resolution of LCM is around 3 – 5 μm. [57]

Spatial in situ array capture describes a group of methods that utilize spatially barcoded probe arrays that capture polyadenylated mRNA in an untargeted manner and convert it to cDNA. Subsequent sequencing and analysis correlates the spatial barcode with cellular position, with resolution dependent on the resolution of the capture probe array.[58] Coined spatial transcriptomics, array capture techniques in this category have been commercialized by 10X Genomics and various iterations of the technique have been developed, including Slide-seq, [59] Slide-seqV2, [60] Stereo-seq, [61] and PIXEL-seq. [62]

In situ hybridization allows the detection and spatial localization of nucleic acids in a tissue via probes with labeled complementary sequences to the target nucleic acid. [63] Early techniques were useful in identifying expression patterns but were more qualitative than quantitative. The first notable quantitative method, smFISH (single molecule fluorescence in situ hybridization), enabled each individual labeled transcript to be visualized as a spot via microscopy. Current ISH- based variations include seqFISH (sequential fluorescence in situ hybridization), [64] seqFISH+, [65] MERFISH (multiplexed error-robust fluorescence in situ hybridization), [66] enhanced electric FISH, [67] and EASI-FISH (expansion-assisted iterative fluorescence FISH). [68]

In situ sequencing sequences mRNA directly in a tissue section and can yield subcellular resolution. Rather than using gene-specific probes, -ISS based techniques profile one to two bases

of primed and amplified transcripts within the tissue. These are linked to a fluorophore that identifies each transcript. Primers may be targeted or untargeted and are generally amplified using rolling circle amplification (RCA).[69] Examples include FISSEQ (fluorescence in situ sequencing), [70] ExSeq, [71] and STARmap. [72]

However, all of these methods suffer from significant disadvantages. Microdissection-based techniques are limited by their spatial resolution, throughput, and degradation of genetic material due to laser exposure. [73] Many of the -ISH and -SS techniques require significant sample processing, including formalin fixation or gene-specific probe sets. Spatial resolution and mRNA recovery rates can also be low. Perhaps most significantly, all of these methods have an extremely high time requirement to generate sufficient cellular data with statistical significance- many hours to days of microscope imaging time, analysis of terabytes of image data, and painstaking manual sample preparation.

A significant contribution to the field of spatial biology would be a method compatible with batch processing to image, identify, and isolate multiple whole cells of interest from a tissue section without significant manual effort. Here we present a unique method called cold plasma – based live cell lithography (CPLCL). Inspired by the fine resolution of nanofabrication and nanolithography techniques, we utilize a cold plasma jet to “etch” away unwanted tissue material and use multi-micrometer sized magnetic beads to provide a spatial “mask” to protect cell(s) of interest. The magnetic bead “masks” are spatially directed to cells of interest using surface marker antibodies and a streptavidin- biotin conjugation system. Once the etching process is complete, each individual cell-bead pair can be individually picked up by a small magnetic probe and placed into a microarray plate for downstream sequencing or proteomics.

3.2.2 A Brief Review of Lithographic and Etching Processes

Micro or nano lithography techniques concern the engineering (patterning, etching, deposition, or printing) of micro or nano-meter features onto a substrate. With the evolution of the semiconductor industry, the field has taken off and has become a critical and commercially successful technique capable of producing sub-100 nm patterns.[74] Although many lithography techniques exist, the workflow generally consists of 1) deposition of a substrate, 2) patterning using a mask or maskless aligner, 3) an etching process, and 4) removal of the photoresist or other unwanted material.

The etching process in such techniques often involves material removal from a surface via a plasma. A high-speed stream of plasma gas mixture is shot in pulses at a sample. This plasma source, also called the etch species, consists of charged ions or neutral atoms and radicals. Generally, plasma etching occurs in low pressure chambers under 100 Pa. The temperature of the plasma depends on the requirements of the system but often ranges from 50˚ C to > 300˚ C. [75]

At these temperatures and pressures, plasma etching would incinerate most organic matter and kill microorganisms or cells. When fully ionized, the electrons and heavy species inside a plasma are at thermal equilibrium and release energy in the form of heat. However, there is a way to generate a plasma in such a manner that the energy of the electrons is surplus to the heavy elements, resulting in a non-equilibrium environment called nonthermal or cold plasma. This type of plasma can exist at temperatures close to room temperature (under 40˚ C), making it compatible with organic material processes.

3.2.3 Introduction to Cold Plasmas

Plasma, named after a Greek word meaning “moldable substance,” is the most common state of matter and is characterized by a significant portion of charged particles. The most well known plasmas include natural phenomena such as the sun and the stars, galaxies, lightning, solar winds, and the aurora borealis. On earth, temperate pressures and temperatures mean that plasmas are more rare. However, artificial plasmas can be generated that have a variety of uses, and many of them are part of our everyday lives – including plasma televisions and neon and fluorescent lights. Industrial purposes of artificial plasmas include plasma etching, sputtering, surface cleaning, plasma-enhanced chemical vapor deposition, ozone generation, and arc welding. [76]

Plasmas consist of partially ionized gases comprised of molecules, radicals, neutral and excited species, ions, photons, and electrons. In a thermal plasma, also known as “hot” or “equilibrium” plasma, all particles are at roughly equal temperatures and are completely ionized. Conversely, in a nonthermal plasma, also known as “cold” or “non-equilibrium” plasma, excited species are generated in a way such that the electron temperature becomes much hotter than the temperature of ions and neutrals. [77] In such a nonthermal plasma, the electron gas can reach temperatures of more than 20,000 K while the rest of the gas ions and neutral atoms stay under 40˚C.[78] Thus, it can even be touched with bare hands while operating. Because of this, nonthermal plasma is uniquely suited for use on biological materials and in biomedical applications.

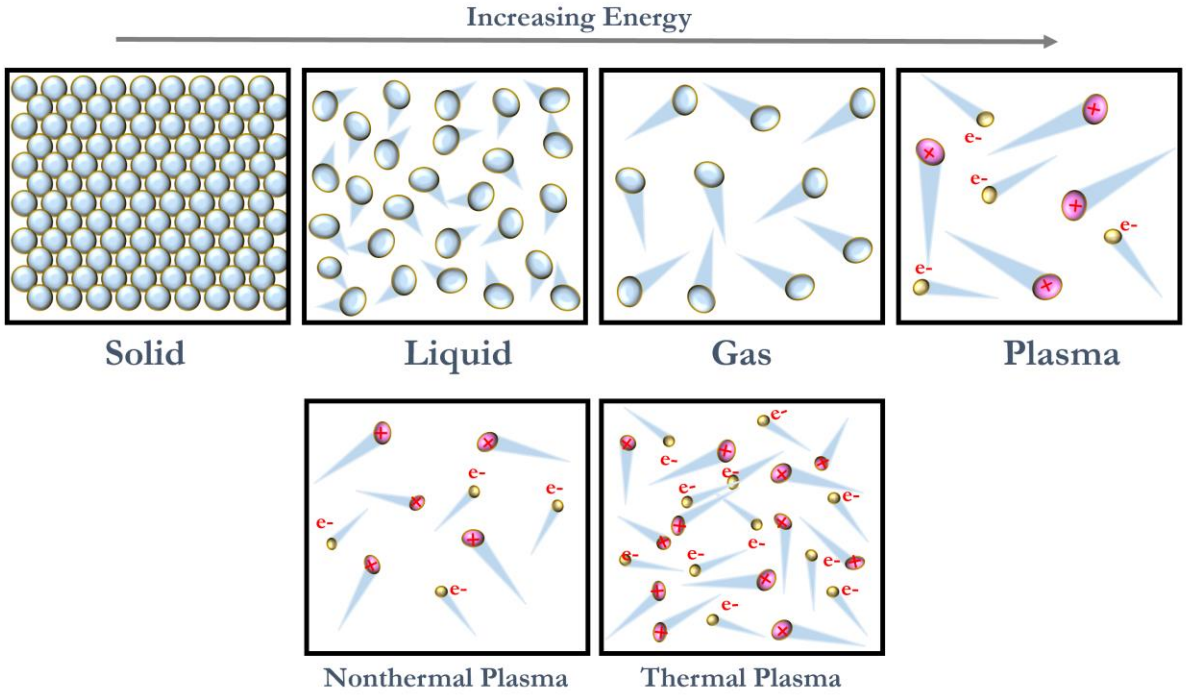

Figure 3.1: States of matter; Nonthermal versus thermal plasma.

One of the principal outcomes of a cold plasma is the generation of large amounts of reactive species. These energized species, collectively known as RONS or primary reactive species, are highly concentrated in the plasma plume. These species include reactive nitrogen species (RNS) such as NO, NO_2, N_2O, N_2O_5, and atomic N; reactive hydrogen species (RHS); and reactive oxygen species (ROS) such as O_2, H_2O2, O, O_3, and OH radicals. [79]

Some of these species immediately undergo a radioactive decay whereas others integrate with neutrals, water molecules, or other reactive species. The primary reactive species can become secondary reactive species such as H_2O_2, NO_3, and O_3. RONS produced in the gaseous phase can dissolve in liquid to form tertiary species. The lifespan of these comparatively long-lasting reactive species endure from milliseconds to several days and include O_3, H_2O_4, NO_3, and NO_2.[80] Cold

plasma also outputs electromagnetic radiation, especially in the wavelengths of vacuum ultraviolet (10 – 200 nm) and ultraviolet (100 – 400 nm).[81]

The types of reactive species in a plasma can been ascertained through methods including optical emission spectroscopy, mass spectroscopy, optical absorbance spectroscopy, microwave or heterodyne interferometry.[82] To determine species in the liquid phase (in the case of media treatment or humid targets), electron paramagnetic resonance spectroscopy, UV-vis absorption spectroscopy, mass spectroscopy, and direct chemical methods can be used.[83] The chemical species present and the transition to secondary or tertiary species depends largely on the feed gas composition and the interaction of plasma species with the characteristics of the plasma target. Although most plasma systems focus on the effects of long-lived reactive species like O_3, H_2O_2, H_3O^+, NO_2^-, and NO_3^-, short lived species are crucially important as they are primarily responsible for biological effects during direct plasma treatments and they are the source of the long lived species. [84]

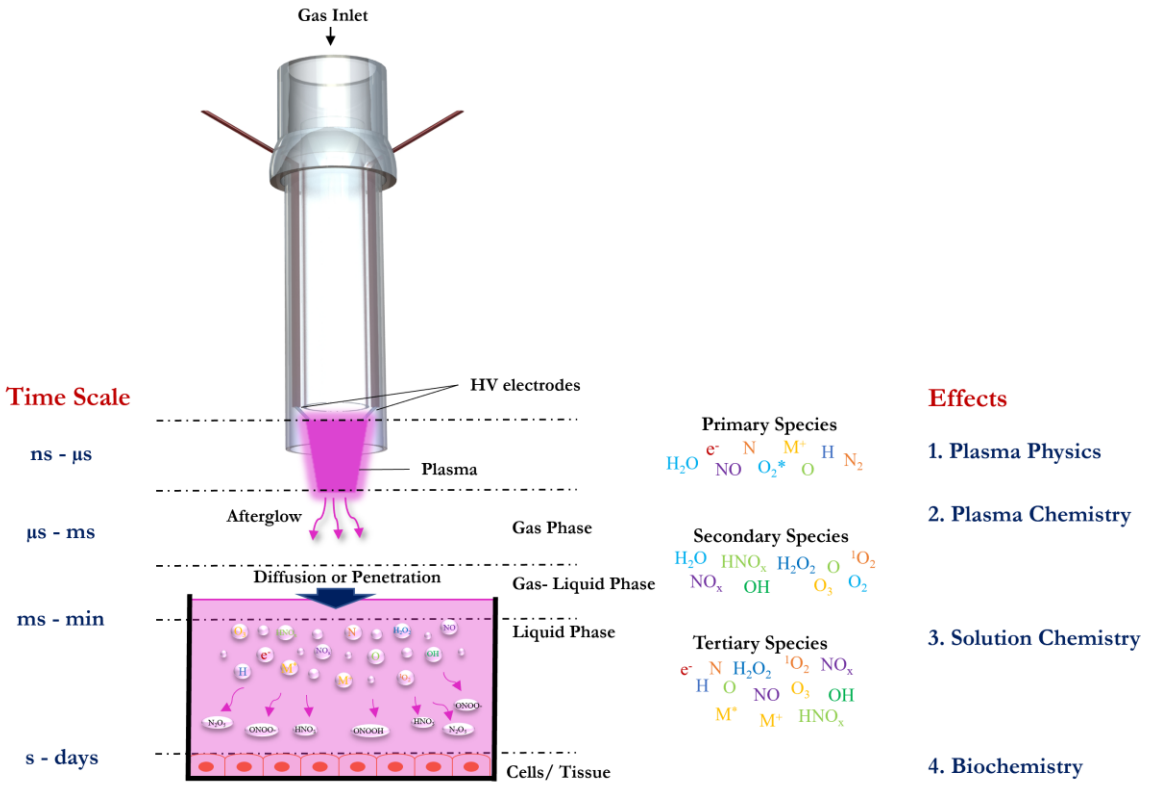

Figure 3.2: Plasma species and reactivity timescales.

3.2.4 How to Generate Plasmas

Various plasma-producing devices exist that all rely on similar mechanisms. Examples of plasma-producing devices include the plasma jet, dielectric barrier discharge (DBD), microwave plasma torch, and nanosecond plasma gun. [85] Plasmas are typically produced by pumping some form of carrier gas (nitrogen, argon, helium) across a high voltage alternating current (AC) differential between two electrodes, typically with frequencies in the kHz range and power consumption between 10 – 100 W. [86] This results in a self-propagating plasma plume outwards toward the target.

The composition of the operating gas, equipment configuration, power, mode of exposure, distance to target, exposure time and gas flow rate will all affect the types and concentration of

reactive species exhibited in the plasma. The feed gas composition is the most important parameter in determining the type of reactive species present in the discharge, whereas the operating parameters of the equipment setup most affect the dosage of reactive species that reach the target.[87] The distribution of the electron energy that determines these species is known as the electron energy distribution function (EEDF).[88] Intuitively, an increase in the EEDF increases the ionization coefficient and excitation rate.

3.2.5 Cellular Effects and Mechanisms

While early studies in the late 1980s and 1990s focused on the use of cold plasmas in sterilization, hygiene, and wound healing, recent discoveries have implicated cold plasma as a useful tool in biomedical applications. For example, cold plasma has been demonstrated to have an exacerbated effect in cancerous cells; relatively low doses of nonthermal plasma treatment were found to selectively cull cancer cells while having minimal effect on healthy cells.[89]

Cold plasma exhibits strongly oxidative properties that can trigger signaling pathways in eukaryotic cells. Correspondingly, these pathways trigger changes in cell physiology, metabolism, growth, aging, and apoptosis. While various reactive species in nonthermal plasma are created, lost, or changed in nanoseconds to seconds, their complex influence on cellular integrity and processes can have enduring effects in timescales of seconds to days.[90] Secondary products are more stable and their effects can compound and even spread to surrounding cells.

The cellular effects of nonthermal plasma are abundant and depend heavily on the type of cell, experimental conditions, delivery dosage, and type of reactive species present in the plasma. For example, whether the treatment target is aqueous or dry dramatically affects the chemistry of RONS. Liquid bombarded by plasma can experience pH reductions by more than 2.[91] Known morphological changes to the cell may include membrane lipid oxidation, extracellular molecules

oxidation, intracellular molecules oxidation, DNA damage, signal transduction, and gene expression changes.[92]

Cold plasma has a few notable cellular effects that potentiate its use as a suitable etching medium for our CPLCL device. As a requirement for our etching process, we want to be able to reliably remove, or "etch" away, the regions outside of our ROI. At the same time, we want to be able to preserve with as little damage as possible the cells in our ROI. Cold plasma has been proven time and again to be capable of inducing apoptosis. It also has been shown to cause damage to extracellular adherence proteins, which is desirable for "lifting off" our unwanted cell areas. In theory, these characteristics satisfy our "etch" requirement. Finally, the reactive particles of cold plasma have a relatively brief half-life and therefore usually only penetrate the surface layer of cells. Therefore, it is possible that a "mask" in the form of a magnetic bead of several microns would be sufficient to protect cell(s) underneath.

3.3 PRINCIPLES AND METHODS

3.3.1 Workflow

The workflow of Cold- Plasma Based Live Cell Lithography is as depicted in Figures 3.3 and 3.4. Starting with a tissue section as depicted in yellow, cellular ROIs with known surface markers are selected (Figure 3.3a). Using the corresponding biotinylated antibody for those surface markers, streptavidin-coated magnetics beads are conjugated to the cell ROIs via the biotinylated antibody (Figure 3.3b). Unbound material is then washed away (Figure 3.3c) and etching via a custom cold plasma jet is performed (Figure 3.3d). Theoretically, at this stage cells outside of the ROIs undergo apoptosis and liftoff from the substrate (Figures 3.3e-f). Cells inside the ROI can then be collected via magnetic probes for single cell analysis (Figure 3.3g). In the case of multiple

cells covered under a single ROI, for example in the case of T cells bound with cancer cells, a similar approach can be utilized (Figure 3.4).

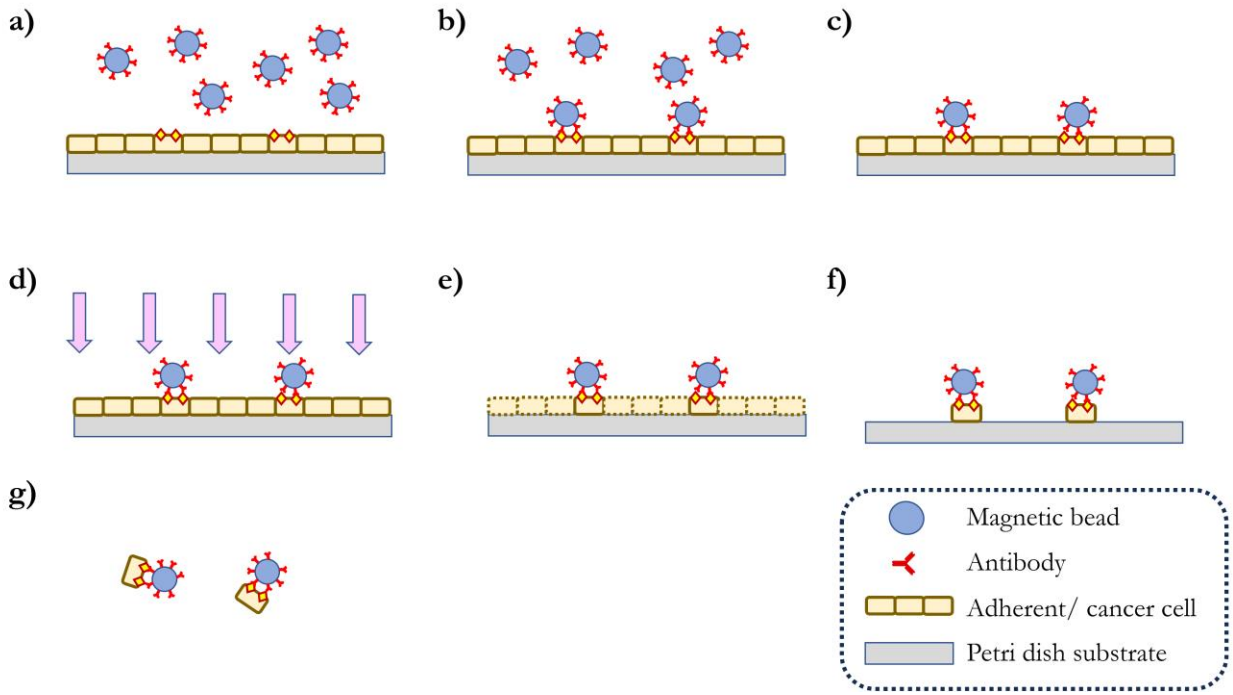

Figure 3.3: Workflow for single cell plasma- based live cell lithography. a) Formation of antibody-magnetic bead conjugates. b) Antibody binding with target cell antigen. c) Washing of free-floating magnetic beads and microscope observation. d) Cold plasma exposure. e) Post- exposure. f) Wash/ remove dead cells. g) Remove and collect cell/ magnetic bead complex.

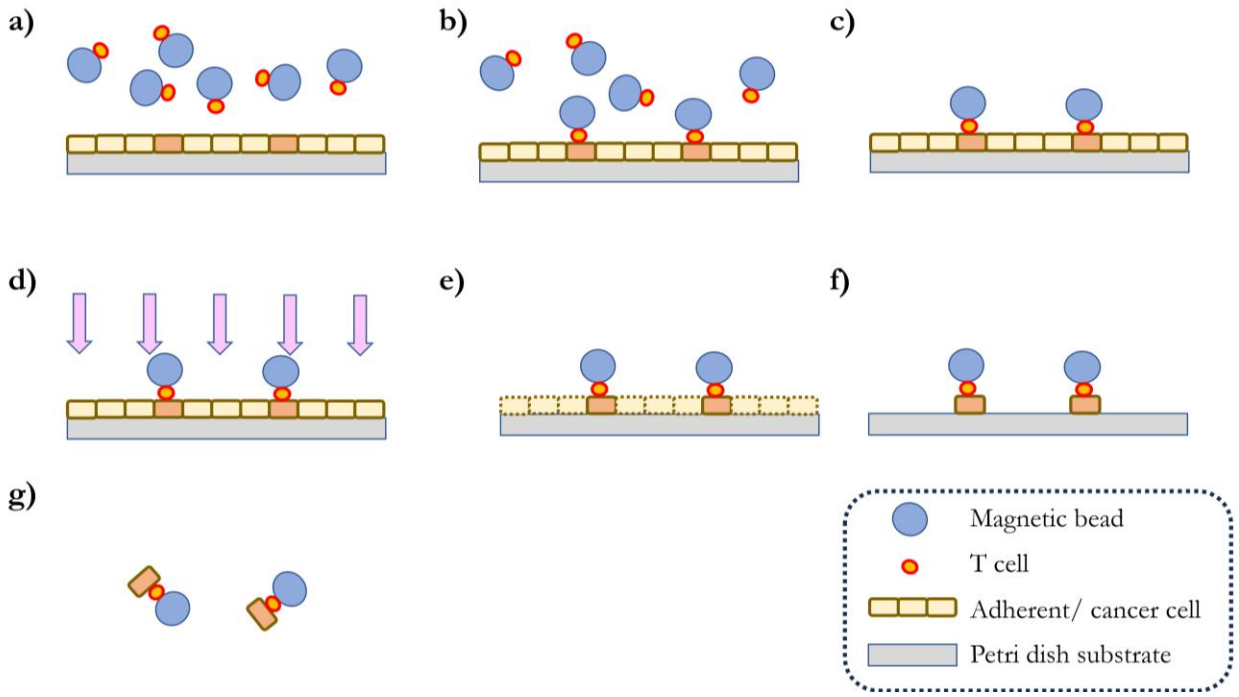

Figure 3.4: Workflow for cell doublet plasma- based live cell lithography. a) Formation of antibody-magnetic bead – T cell conjugates. b) T cell binding with cancer cell. c) Washing of free-floating magnetic beads/ cells and microscope observation. d) Cold plasma exposure. e) Post- exposure. f) Wash/ remove dead cells. g) Remove and collect cell doublet/ magnetic bead complex.

3.3.2 Plasma Device

A custom plasma jet device was built using a power supply (30V 10A DC Power Supply, Lwlongwei Electronics, China), a high voltage transformer (B078SWVGXT, Walfront Electronics, China), a gas supply with an in-line flow meter (Smart-Trak 50 Series, Sierra Instruments, Monterey, CA, USA), and a custom dual-electrode nozzle. The configuration is as shown in Figure 3.5. The feed gas was nitrogen at a flow rate of 5 - 8 L/min. The voltage output of the transformer is 20 kV and the frequency was measured to be approximately 12 kHz. To prevent the transformer from overheating, the cool side of a Peltier cooling chip (TEC1-12706) was placed in contact with the transformer and attached using thermal paste. The voltage input to the Peltier chip was controlled via a thermistor attached to a temperature controller (ILX

Lightwave, LDT-5910B, Bozeman, MT, USA). A large computer fan powered by 12V from a DC power supply was placed on the hot side of the Peltier chip to shunt away heat from the system. The average plasma temperature was 32.3˚C.

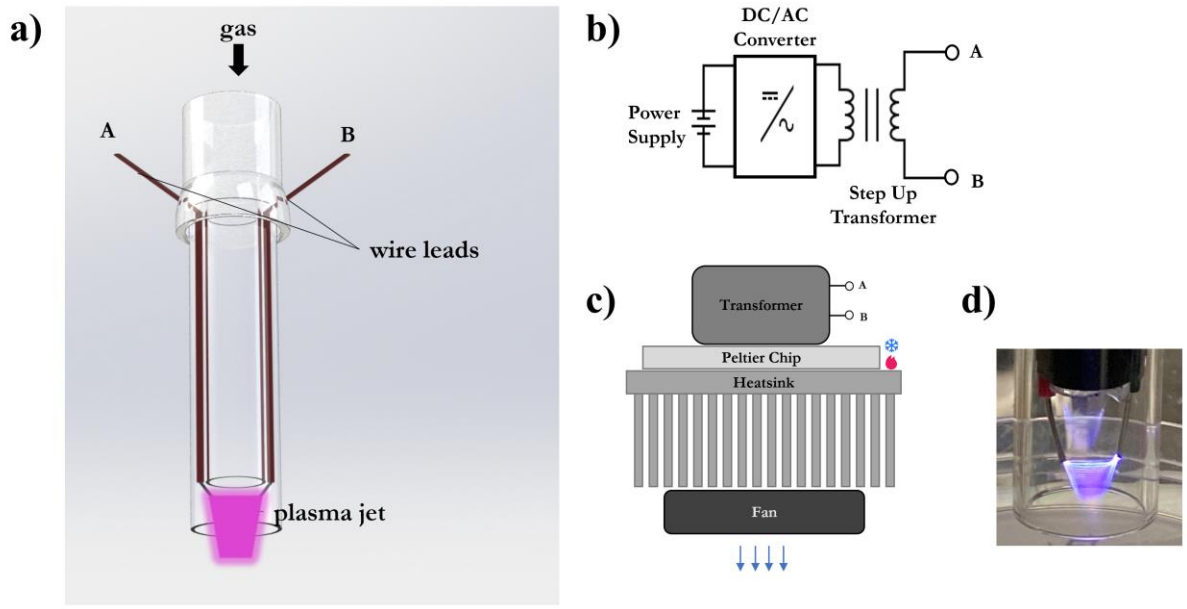

Figure 3.5: The plasma device configuration. a) The dual – electrode nozzle. b) The transformer contains an onboard DC/AC converter. c) Transformer cooling setup. d) Plasma jet in ambient lighting.

3.3.3 Cell Culture

MCF7, HeLa, HEK, and Jurkat cells were purchased from ATCC. Cells were cultured in 90% DMEM supplemented with 10% fetal bovine serum, 100 U/mL of penicillin, and 100 µg/mL streptomycin. Cells were maintained in an incubator at 37˚C and 5% CO_2. Cells were passaged every two to three days. Cells were allowed to adhere for 2.5 days for proper adhesion prior to plasma treatment. Following plasma treatment, a Live/ Dead Cell Stain Kit was performed (R37601, ThermoFisher Scientific, MA, USA).

3.3.4 Bead Selection

Absolute Mag™ Streptavidin Magnetic Particles in sizes of 8 - 9.9 µm, 18 - 22.9 µm, and 38.0 - 44.0 µm (CD Bioparticles, New York, New York, USA) were selected to form a mask covering the cell(s) of interest. Leveraging the strong binding properties of biotin and streptavidin, cell(s) of interest can be selectively bound to the beads by choosing the appropriate biotinylated antibody. When the process is completed, magnetic beads will be bound directly above the cells of interest in a two- dimensional adherent layer of cells.

3.3.5 Bead-Cell Conjugation Protocol

The conjugation was performed via the following steps:

1. Pipette 20 µL of 5% w/v streptavidin coated magnetic beads into a microcentrifuge tube.
2. Place on a magnet for 1 min to gather beads together. Then, carefully remove the supernatant.
3. Keeping the tube on the magnet, add 20 µL PBS, wait 1 min, and again remove the supernatant. Repeat 4 times.
4. Add antibody:
    a. 0.5uL of 0.5 mg/ml antibody per 10 µL bead volume
    b. Put on shaker and gently shake for 30 minutes.
5. Repeat wash step 4 – 5 times on the magnet with PBS with 0.1% bovine serum albumin.
6. Resuspend with 400uL PBS/0.1%BSA per 3 cm dish.
7. Aspirate out media from cell culture dish and place cell culture dish onto a flat magnet.

8. Add 400 µL of bead solution per 3 cm dish and wait 2 minutes.
9. Place in incubator for 30 minutes. After 30 minutes, the cell-bead conjugation will be complete.

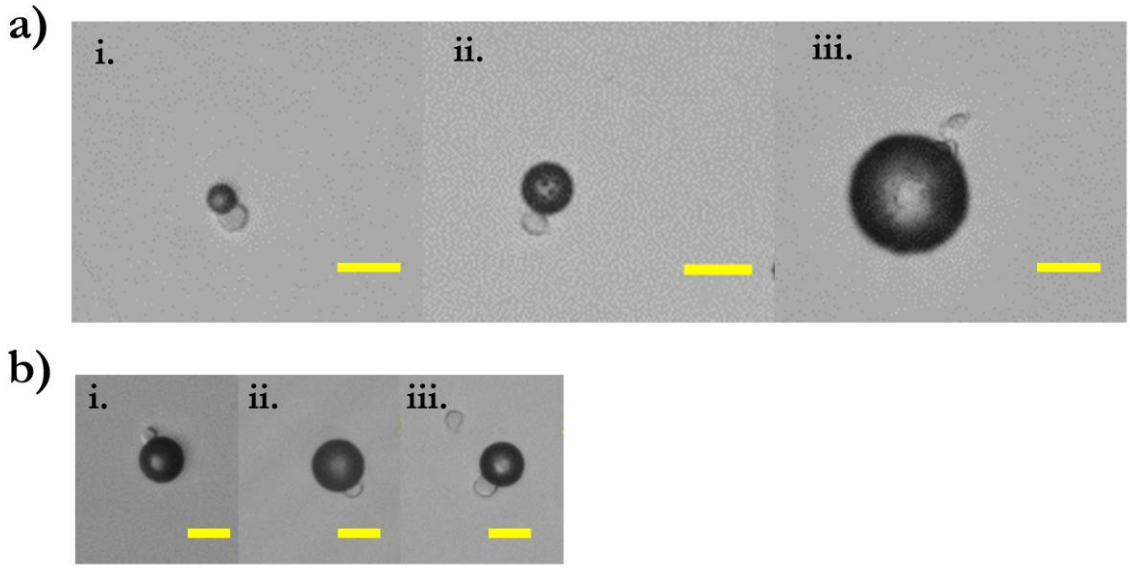

Figure 3.6: Example cell – bead conjugation. Streptavidin-coated magnetic beads were incubated with biotinylated antibodies against a chosen cell target. Next, the bead-antibody complex was incubated with cells according to the protocol listed in Principles and Methods section 3.3.5. The cell- antibody pairs depicted here are HepG2 cells with antibodies targeting CD45. a.i) 8 – 9.9 µm bead; a.ii) 18 – 22.9 µm bead; a.iii) 38.0 – 44.0 µm bead; b.i-iii) 18 – 22.9 µm bead.

3.4 RESULTS

3.4.1 Demonstration of Cellular Apoptosis and Liftoff

MCF7 cells were cultured in 3 cm diameter petri dishes for 2.5 days. Immediately prior to plasma treatment, the cellular growth media was removed from the dish via aspiration. The gas flow rate was 8 L/min and the plasma temperature was measured to be 32.5˚C. The distance between the sample stage and the electrode tips of the plasma device was 8 mm as calibrated via

DinoCam. The cells were plasma treated for 10 min with microscope images taken every 2 minutes. At the conclusion of the 10 minutes of plasma treatment, cells were rehydrated by flooding the dish with 1X PBS and imaged after an additional 10 minutes. No significant effects were noticed in the first 10 minutes of plasma treatment (Figure 3.7a). However, following rehydration, significant cell liftoff or apoptosis was observed inside the plasma treated region, while outside the plasma treated region cells remained intact and healthy (Figure 3.7b). At the edge of the plasma treated region, the demarcation between the two regions is especially apparent. These preliminary results demonstrate that plasma treatment by our custom device can induce cellular apoptosis or liftoff, the first requirement of CPLCL's etching removal process.

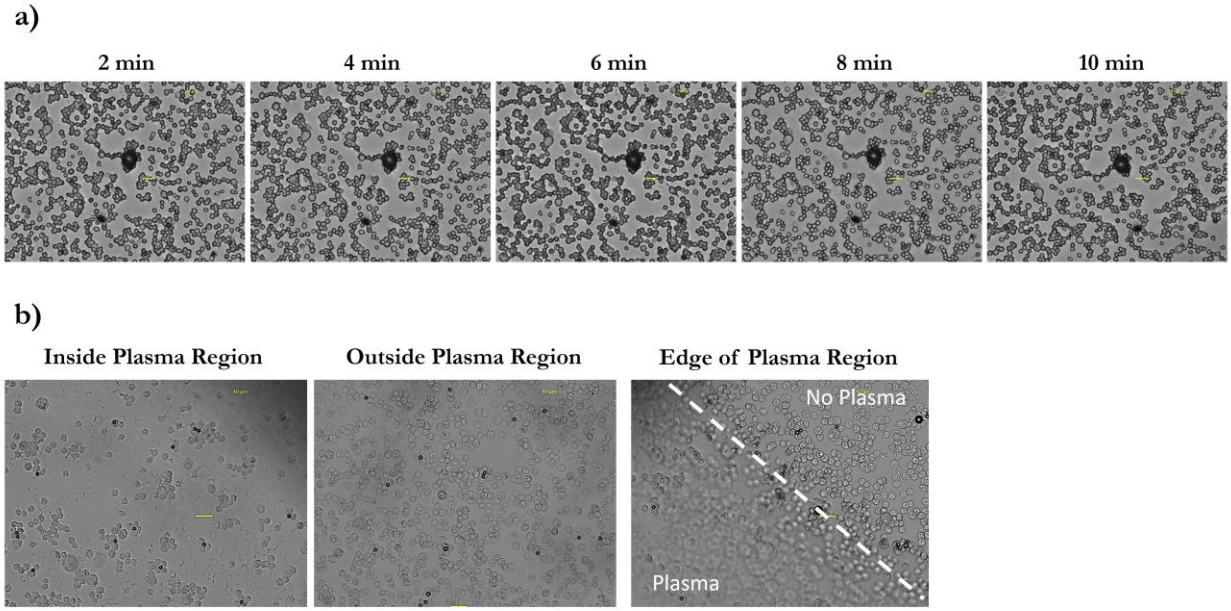

Figure 3.7: Plasma treatment versus time. a) Plasma- treated MCF7 cells vs time. b) Following 10 minutes of plasma treatment, the cells were rehydrated with PBS. Inside the plasma region, we observe significant cell death and cell liftoff. Outside the plasma-treated region, we observe healthy cells. At the edge of the plasma-treated region, the demarcation is especially apparent.

3.4.2 Assessment of Cellular Death under Various Experimental Conditions

3.4.2.i Plasma Treatment versus Time of HeLa and MCF7 Cells

HeLa cells and MCF7 cells were cultured in 3 cm diameter petri dishes for 2.5 days. Immediately prior to plasma treatment, the cellular growth media was removed from the dish via aspiration. The gas flow rate was 8 L/min and the plasma temperature was measured to be 34.2˚C. The distance between the sample stage and the electrode tips of the plasma device was 8 mm as calibrated via DinoCam. Cells were plasma treated, rehydrated with PBS following the plasma treatment, then stained with a live/dead fluorescent cell stain. A green colored stain indicates a live and healthy cell, whereas a red stain indicates cell death. Three regions within the plasma treatment zone were imaged before plasma treatment, after plasma treatment, after 15 minute rehydration, and after live/dead fluorescent staining.

For both HeLa and MCF7 cell types, all plasma treatment times investigated (3 min, 6 min, 9 min, 12 min, and 15 min) demonstrate cell death of the entire population within the plasma treatment region (Figures 3.8 and 3.9). Notably, we do not see as much cell liftoff as observed in the experiment in section 3.4.1.

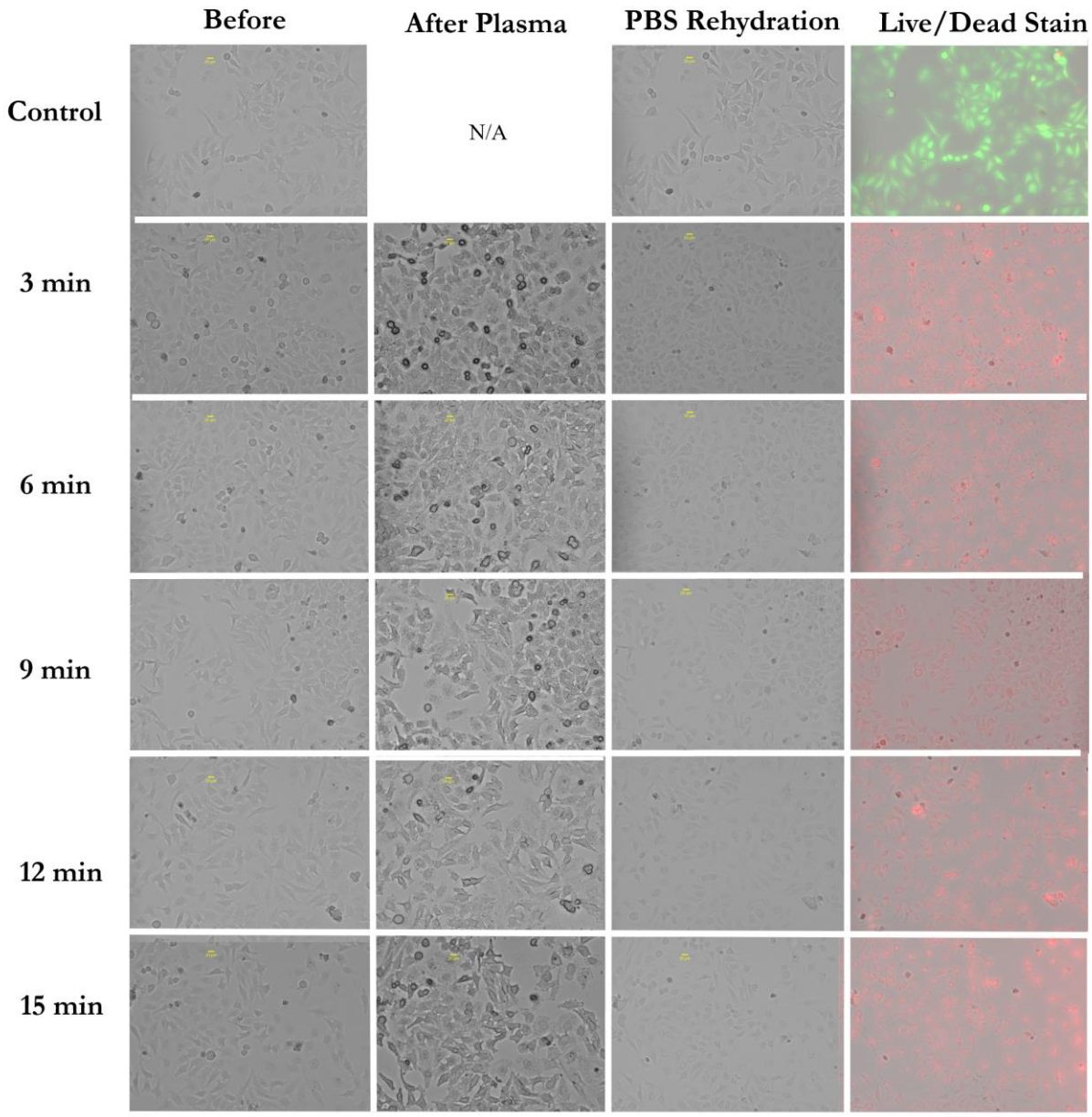

Figure 3.8: HeLa cells; Δ Plasma Treatment Time; Flow Rate: 8L/min; Plasma Temp: 34.2˚C; d = 8 mm. Significant cell death, but insignificant cell liftoff, is observed at all measured time points.

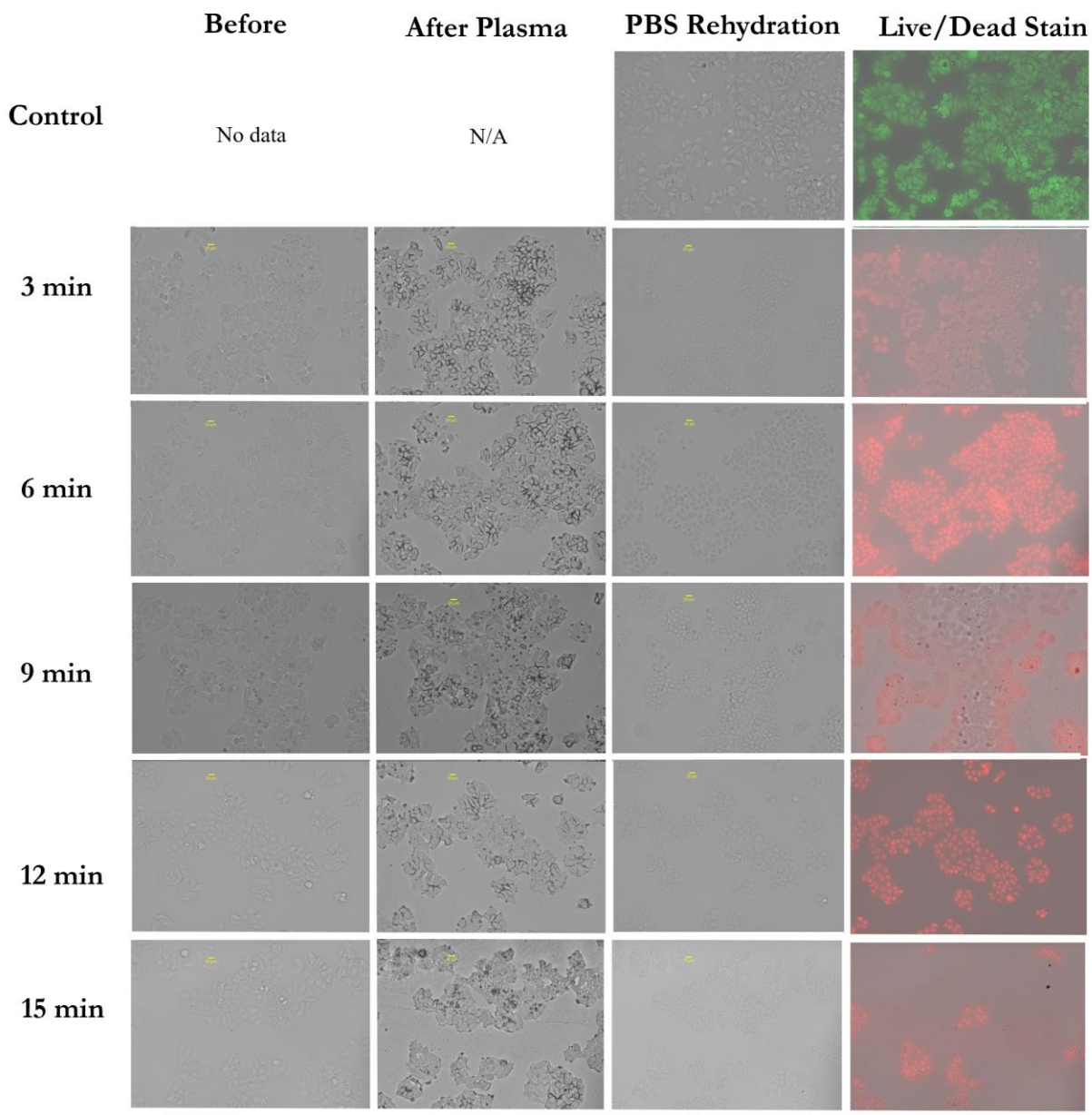

Figure 3.9: MCF7 cells; Δ Plasma Treatment Time; Flow Rate: 8L/min; Plasma Temp: 34.2˚C; d = 8 mm. Significant cell death, but insignificant cell liftoff, is observed at all measured time points.

3.4.2.ii Assessment of Effects of Nitrogen Gas Only versus Plasma Treatment

To assess whether the cell death observed in the experiments in section 3.4.2.i was a direct consequence of the plasma treatment or a side effect of drying due to the relatively high gas flow rate, shorter treatment times of 10 s, 30 s, and 1 min were performed with the nitrogen gas only at a flow rate of 8 L/ min (no voltage input to the electrodes of the plasma nozzle) and with the plasma device on (voltage supplied to the electrodes of the plasma nozzle).

MCF7 cells were cultured in 3 cm diameter petri dishes for 2.5 days. Immediately prior to plasma or nitrogen gas treatment, the cellular growth media was removed from the dish via aspiration. The gas flow rate was 8 L/min and the plasma temperature (if applicable) was measured to be 34.2˚C. The distance between the sample stage and the electrode tips of the plasma device was 8 mm as calibrated via DinoCam. Cells were plasma treated, rehydrated with PBS following the plasma treatment, then stained with a live/dead fluorescent cell stain. A green colored stain indicates a live and healthy cell, whereas a red stain indicates cell death. Three regions within the plasma treatment zone were imaged before plasma treatment, after plasma treatment, after 15 minute rehydration, and after live/dead fluorescent staining.

After only 10 seconds of treatment by nitrogen gas or plasma, we observe a mixed red and green fluorescent image during our live/dead cell staining, indicating that the propidium iodide present in the live/dead stain is binding to intracellular DNA, and the cell is dead or dying. We also observe that for the 30 sec and 1 minute time points, the plasma treated cells appear to have more red fluorescence in their staining images than the nitrogen gas treated cells. This indicates that the nitrogen gas flow has a moderate impact on cell death while plasma treatment has a more profound effect.

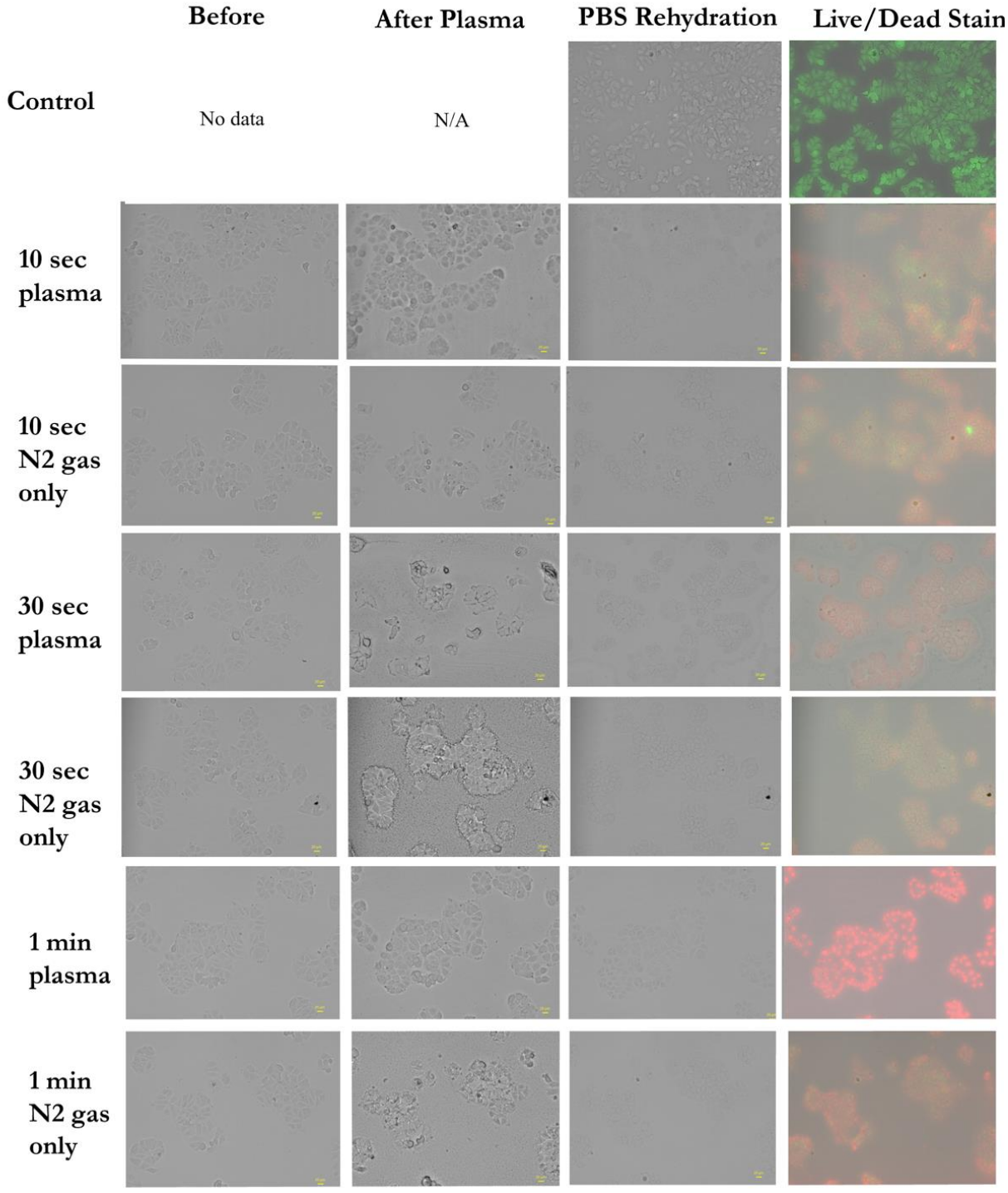

Figure 3.10: MCF7 cells; Δ Treatment Time; Flow Rate: 8L/min; Plasma Temp: 34.2˚C; d = 8 mm.

3.4.2.iii Assessment of Effects of Distance to Sample Stage

To assess the effects of distance to the sample stage, the distance between the sample stage and the electrode tips of the plasma device varied from 12mm to 8 mm in increments of 1 mm as calibrated via DinoCam.

MCF7 cells were cultured in 3 cm diameter petri dishes for 2.5 days. Immediately prior to plasma or nitrogen gas treatment, the cellular growth media was removed from the dish via aspiration. The gas flow rate was 8 L/min and the plasma temperature was measured to be 34.2˚C. Cells were plasma treated for 30 seconds, rehydrated with PBS following the plasma treatment, then stained with a live/dead fluorescent cell stain. A green colored stain indicates a live and healthy cell, whereas a red stain indicates cell death. Three regions within the plasma treatment zone were imaged before plasma treatment, after plasma treatment, after 15 minute rehydration, and after live/dead fluorescent staining. Similar results in terms of the amount of red fluorescence present in the staining images were observed for distances of 12 mm, 11 mm, 10 mm, and 9 mm, while more red fluorescence present in the staining for the distance of 8 mm indicated a potential for increased cell damage at that distance.

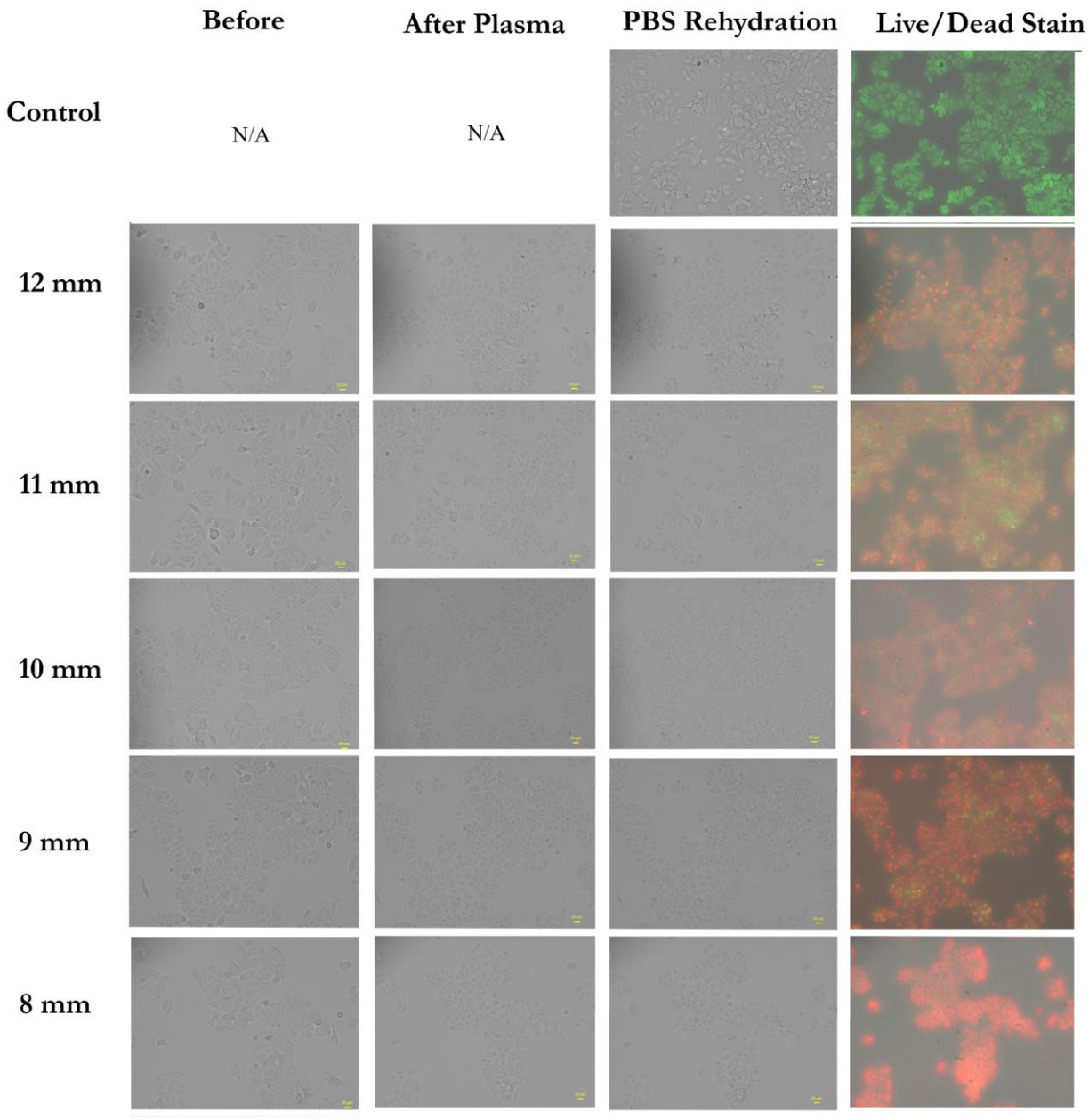

Figure 3.11: MCF7 cells; Δ Distance to Sample; Flow Rate: 8L/min; Plasma Temp: 34.2˚C.

3.4.2.iv Assessment of Effects of Increased Media Volumes (1 mL, 1.5 mL, 2 mL)

MCF7 cells were cultured in 3 cm diameter petri dishes for 2.5 days. Immediately prior to plasma or nitrogen gas treatment, the cellular growth media was removed from the dish via aspiration. To assess the effects of increased media volume present during plasma treatment, fresh cell media in volumes of 1 mL, 1.5 mL, and 2 mL were added to the cell dishes immediately prior to plasma or nitrogen gas treatment. Cells were treated, rehydrated with PBS following the plasma treatment, then stained with a live/dead fluorescent cell stain. Three regions within the plasma treatment zone were imaged before plasma treatment, after plasma treatment, after 15 minute rehydration, and after live/dead fluorescent staining. The gas flow rate, plasma temperature, treatment time, distance to sample stage, and live/dead cell stain results are as recorded in Table 3.1.

With the increased media volume in the cell dishes, a new phenomenon was noticed as depicted in Figure 3.12. Briefly, the gas flow would displace the media directly under the plasma nozzle causing a “dry spot.” The time of the initial emergence of this “dry spot” was dependent on the experimental parameters and ranged from almost immediately to >15 minutes. The size of the dry spot increases with time. Notably, the presence of the dry spot had a 100% correlation with cell death as determined by live/dead staining results, and regions outside of the dry spot had a 100% correlation with live cells. Additionally, we note that with large volumes of media covering the target layer of cells, it is unlikely that the primary effects of the plasma can penetrate to reach the target cells.

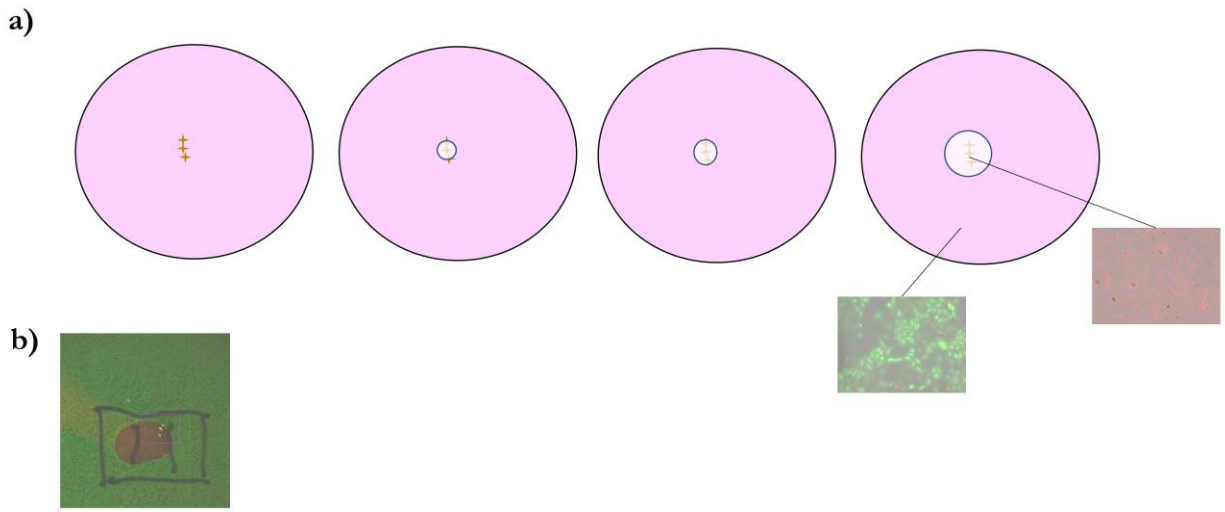

Figure 3.12: Explanatory diagram of dry spot phenomenon. a) Depending on the experimental conditions, a dry spot forms directly under the plasma nozzle head due to the gas flow and increases in size as time goes on. b) Overview photo of live/dead cell staining after dry spot observed. The dry spot region had a 100% correlation with cell death. Regions outside of the dry spot had a 100% correlation with live cells.

Table 3.1: MCF7 cells; Variable Experimental Conditions and Results

Cell Type	Amount of Media (mL)	Gas Flow Rate (L/min)	d (mm)	Treatment Time	Plasma On (Y/N)	Plasma Temp (˚C)	Live/ Dead Stain Results	Dry Spot?
MCF7	1	8	10	10s	N	32.7	dead inside dry spot; live outside	Y, t=3 sec
				20s			dead inside dry spot; live outside	Y, t=3 sec
				30s			dead inside dry spot; live outside	Y, t=3 sec
	1.5	8	10	30s	Y	32.7	live	N
				1 min			live	N
				3 min			live	N
				6 min			dead inside dry spot; live outside	Y, t=5.5 min
				9 min			dead inside dry spot; live outside	Y, t=5.5 min
				15 min			dead	Y, t=5.5 min
	1.5	5	10	3 min	Y	32.7	live	N
				6 min			live	N
				12 min			live	N
				15 min			dead	Y, t= 12.25 min
	2	5	10	3 min	Y	32.7	live	N
				6 min			live	N
				12 min			live	N
				15 min			live	N

3.5 DISCUSSION

Cold Plasma- Based Live Cell Lithography can be broken down into two distinct benchmarks: a) successful removal, or “etching” of cells outside of the region of interest; and b) successful preservation and recovery of cells within the region of interest. We have successfully built a robust and reliable prototype that produces cold plasma and the corresponding methodology to bind our bead “mask” to adherent cells. Our results indicate that we can reliably induce cell death, but we found that cell removal via plasma treatment was unreliable. Given that the cell removal, or “etching” process is so crucial to the success of CPLCL, we need to investigate other methodologies or conditions to enable reliable removal of regions outside of our region of interest.

There are several ways to approach this issue. One possibility is that altering the dosage conditions of the cold plasma etch source could give us finer control of the process. The input voltage of the plasma, the pulse frequency, the material of the electrodes, the feed gas mixture and the conformation of the plasma nozzle can all alter the delivery dosage and type of reactive species to the sample target. Another option is to fundamentally alter our workflow to achieve cell lithography in an alternate way – for example, encapsulating the region of interest in a biocompatible polymer, enabling stronger etch parameters without harming the cells inside the region of interest.

3.6 REFERENCES

[56] Virginia Espina; Julia Wulfkuhle; Valerie Calvert; Amy VanMeter; Weidong Zhou; George Coukos; David Geho; Emanuel Petricoin III; Lance Liotta. Laser-Capture Microdissection. Nature Protocols 2006, 1, 586–603. https://doi.org/10.1038/nprot.2006.85.

[57] Virginia Espina; Julia Wulfkuhle; Valerie Calvert; Amy VanMeter; Weidong Zhou; George Coukos; David Geho; Emanuel Petricoin III; Lance Liotta. Laser-Capture Microdissection. Nature Protocols 2006, 1, 586–603. https://doi.org/10.1038/nprot.2006.85.

[58] Cameron William; Hyun Jae Lee; Takahiro Asatsuma; Roser Vento-Tormo; Ashraful Haque. An Introduction to Spatial Transcriptomics for Biomedical Research. Genome Medicine 2022, 14 (68). https://doi.org/10.1186/s13073-022-01075-1.

[59] Samuel Rodriques; Robert Stickels; Aleksandrina Goeva; Carly Martin; Evan Murray; Charles Vanderburg; Joshua Welch; Linlin Chen; Fei Chen; Evan Macosko. Slide-Seq: A Scalable Technology for Measuring Genome-Wide Expression at High Spatial Resolution. Science 2019, 363 (6434), 1463–1467. https://doi.org/10.1126/science.aaw1219.

[60] Robert Stickels; Evan Murray; Pawan Kumar; Jilong Li; Jamie Marshall; Daniela Di Bella; Paola Arlotta; Evan Macosko; Fei Chen. Highly Sensitive Spatial Transcriptomics at Near-Cellular Resolution with Slide-SeqV2. Nat Biotechnol 2021, 39 (3), 313–319. https://doi.org/10.1038/s41587-020-0739-1.

[61] Ao Chen; Sha Liao; Mengnan Cheng; Longqi Liu; Xun Xu; Jian Wang. Spatiotemporal Transcriptomic Atlas of Mouse Organogenesis Using DNA Nanoball-Patterned Arrays. Cell 2022, 185, 1777–1792. https://doi.org/10.1016/j.cell.2022.04.003.

[62] Xiaonan Fu; Li Sun; Runze Dong; Jane Chen; Richard Palmiter; Liangcai Gu. Polony Gels Enable Amplifiable DNA Stamping and Spatial Transcriptomics of Chronic Pain. Cell 2022, 185 (24), 4621–4633. https://doi.org/10.1016/j.cell.2022.10.021.

[63] Cameron William; Hyun Jae Lee; Takahiro Asatsuma; Roser Vento-Tormo; Ashraful Haque. An Introduction to Spatial Transcriptomics for Biomedical Research. Genome Medicine 2022, 14 (68). https://doi.org/10.1186/s13073-022-01075-1.

[64] Eric Lubeck; Ahmet Coskun; Timur Zhiyentayev; Mubhji Ahmad; Long Cai. Single Cell in Situ RNA Profiling by Sequential Hybridization. Nat Methods 2014, 11 (4), 360–361. https://doi.org/10.1038/nmeth.2892.

[65] Chee-Huat Linus Eng; Michael Lawson; Qian Zhu; Ruben Dries; Noushin Koulena; Yodai Takei; Jina Yun; Christopher Cronin; Christoph Karp; Guo-Cheng Yuan; Long Cai. Transcriptome-Scale Super-Resolved Imaging in Tissues by RNA SeqFISH. Nature 2019, 568 (7751), 235–239. https://doi.org/10.1038/s41586-019-1049-y.

[66] Kok Hao Chen; Alistair Boettiger; Jeffrey Moffitt; Siyuan Wang; Xiaowei Zhuang. Spatially Resolved, Highly Multiplexed RNA Profiling in Single Cells. Science 2015, 348 (6233). https://doi.org/10.1126/science.aaa6090.

[67] Lars Borm; Alejandro Mossi Albiach; Camiel Mannens; Jokubas Janusauskas; Ceren Ozgun; Ed Lein; Simone Codeluppi; Sten Linnarsson. Scalable in Situ Single-Cell Profiling by Electrophoretic Capture of MRNA Using EEL FISH. Nat Biotechnol 2023, 41 (222–231). https://doi.org/10.1038/s41587-022-01455-3.

[68] Yuhan Wang; Mark Eddison; Greg Fleishman; Martin Weigert; Scott Sternson; Paul Tillberg. EASI-FISH for Thick Tissue Defines Lateral Hypothalamus Spatio-Molecular Organization. Cell 2021, 184 (26), 6361–6377. https://doi.org/10.1016/j.cell.2021.11.024.

[69] Cameron William; Hyun Jae Lee; Takahiro Asatsuma; Roser Vento-Tormo; Ashraful Haque. An Introduction to Spatial Transcriptomics for Biomedical Research. Genome Medicine 2022, 14 (68). https://doi.org/10.1186/s13073-022-01075-1.

[70] Je Hyuk Lee; Evan Daugharthy; Jonathan Scheiman; Reza Kalhor; Kun Zhang; George Church. Fluorescent in Situ Sequencing (FISSEQ) of RNA for Gene Expression Profiling in Intact Cells and Tissues. Nature Protocols 2015, 10, 442–458. https://doi.org/10.1038/nprot.2014.191.

[71] Shahar Alon; Daniel Goodwin; Anubhav Sinha; Asmamaw Wassie; Adam Marblestone; Edward Boyden. Expansion Sequencing: Spatially Precise In Situ Transcriptomics in Intact Biological Systems. Science 2021, No. 371, 6528. https://doi.org/10.1126/science.aax2656.

[72] Xiao Wang; William Allen; Matthew Wright; Emily Sylwestrak; Felice-Alessio Bava; Karl Deisseroth. Three-Dimensional Intact-Tissue Sequencing of Single-Cell Transcriptional States. Science 2018, 361, 6400. https://doi.org/10.1126/science.aat5691.

[73] Cameron William; Hyun Jae Lee; Takahiro Asatsuma; Roser Vento-Tormo; Ashraful Haque. An Introduction to Spatial Transcriptomics for Biomedical Research. Genome Medicine 2022, 14 (68). https://doi.org/10.1186/s13073-022-01075-1.

[74] Mengmeng Guo; Zhiyuan Qu; Fanyi Min; Zheng Li; Yali Qiao; Yanlin Song. Advanced Unconventional Techniques for Sub-100 Nm Nanopatterning. InfoMat 2022, 4 (8). https://doi.org/10.1002/inf2.12323.

[75] Artem Osipov; Gleb Lankevich; Anastasis Speshilova; Armenak Osipov; Sergey Alexandrov. High-Temperature Etching of SiC in SF6/O2 Inductively Coupled Plasma. Scientific Reports 2020, 20, 19977. https://doi.org/10.1038/s41598-020-77083-1.

[76] L'udmila Holubova; Stanislav Kyzek; Ivana Durovcova; Jana Fabova; Eva Horvathova; Andrea Sevcovicova; Eliska Galova. Non-Thermal Plasma—A New Green Priming Agent for Plants? Int. J. Mol. Sci. 2020, 21 (24), 9466. https://doi.org/10.3390/ijms21249466.

[77] L'udmila Holubova; Stanislav Kyzek; Ivana Durovcova; Jana Fabova; Eva Horvathova; Andrea Sevcovicova; Eliska Galova. Non-Thermal Plasma—A New Green Priming Agent for Plants? Int. J. Mol. Sci. 2020, 21 (24), 9466. https://doi.org/10.3390/ijms21249466.

[78] Adam Harvey; Ibrahim Mohammed; Usman Dahiru; Kui Zhang. Opportunities for Process Intensification Using Non-Thermal Plasmas. Curr. Op. in Chem. Eng. 41, 100930. https://doi.org/10.1016/j.coche.2023.100930.

[79] Kyriakos Sklias; Joao Santos Sousa; Pierre-Marie Girard. Role of Short- and Long-Lived Reactive Species on the Selectivity and Anti-Cancer Action of Plasma Treatment In Vitro. Cancers 2021, 13 (4), 615. https://doi.org/10.3390/cancers13040615.

[80] Kyriakos Sklias; Joao Santos Sousa; Pierre-Marie Girard. Role of Short- and Long-Lived Reactive Species on the Selectivity and Anti-Cancer Action of Plasma Treatment In Vitro. Cancers 2021, 13 (4), 615. https://doi.org/10.3390/cancers13040615.

[81] Judith Golda; Beatrix Biskup; Vincent Layes; Tristan Winzer; Jan Benedikt. Vacuum Ultraviolet Spectroscopy of Cold Atmospheric Pressure Plasma Jets. Plasma Processes and Polymers 2020, 17 (6), 1900216. https://doi.org/10.1002/ppap.201900216.

[82] M Dharini; S Jaspin; R Mahendran. Cold Plasma Reactive Species: Generation, Properties, and Interaction with Food Biomolecules. Food Chemistry 2023, 405 (PA), 134746.

[83] M Dharini; S Jaspin; R Mahendran. Cold Plasma Reactive Species: Generation, Properties, and Interaction with Food Biomolecules. Food Chemistry 2023, 405 (PA), 134746.

[84] Francesco Tampieri; Maria-Pau Ginebra; Cristina Canal. Quantification of Plasma-Produced Hydroxyl Radicals in Solution and Their Dependence on the PH. Anal. Chem. 93, 3666–3670.

[85] Fatemah Faramarzi; Parisa Zafari; Mina Alimohammadi; Mohammedreza Moonesi; Alireza Rafiei; Sander Bekeschus. Cold Physical Plasma in Cancer Therapy: Mechanisms, Signaling, and Immunity. Oxid Med Cell Longev 2021, 9916796. https://doi.org/10.1155/2021/9916796.

[86] Clotilde Hoffmann; Carlos Berganza; John Zhang. Cold Atmospheric Plasma: Methods of Production and Application in Dentistry and Oncology. Med Gas Res 2013, 3 (21). https://doi.org/10.1186/2045-9912-3-21.

[87] M Dharini; S Jaspin; R Mahendran. Cold Plasma Reactive Species: Generation, Properties, and Interaction with Food Biomolecules. Food Chemistry 2023, 405 (PA), 134746.

[88] M Dharini; S Jaspin; R Mahendran. Cold Plasma Reactive Species: Generation, Properties, and Interaction with Food Biomolecules. Food Chemistry 2023, 405 (PA), 134746.

[89] Fatemah Faramarzi; Parisa Zafari; Mina Alimohammadi; Mohammedreza Moonesi; Alireza Rafiei; Sander Bekeschus. Cold Physical Plasma in Cancer Therapy: Mechanisms, Signaling, and Immunity. Oxid Med Cell Longev 2021, 9916796. https://doi.org/10.1155/2021/9916796.

[90] Fatemah Faramarzi; Parisa Zafari; Mina Alimohammadi; Mohammedreza Moonesi; Alireza Rafiei; Sander Bekeschus. Cold Physical Plasma in Cancer Therapy: Mechanisms, Signaling, and Immunity. Oxid Med Cell Longev 2021, 9916796. https://doi.org/10.1155/2021/9916796.

[91] Oliver Handorf; Viktoria Isabella Pauker; Thomas Weihe; Katharina Riedel; Jorg Ehlbeck. Plasma-Treated Water Affects Listeria Monocytogenes Vitality and Biofilm Structure. Front. Microbiol. 2021, 12, 652481. https://doi.org/10.3389/fmicb.2021.652481.

[92] Fatemah Faramarzi; Parisa Zafari; Mina Alimohammadi; Mohammedreza Moonesi; Alireza Rafiei; Sander Bekeschus. Cold Physical Plasma in Cancer Therapy: Mechanisms, Signaling, and Immunity. Oxid Med Cell Longev 2021, 9916796. https://doi.org/10.1155/2021/9916796.

Acknowledgements

Chapter 3, in full, contains unpublished material co-authored with Zhilin Guo and Brendan Schuster. The dissertation author was the primary investigator and author of this chapter.